Confocal Raman micro-spectroscopy of collagen-containing tissues: the impact of optical clearing

Ph.D. Thesis

Author

Ali Jaafar Sadeq

Supervisor

Dr. Miklós Veres

(HUN-REN Wigner RCP)

Doctoral School of Physics
Department of Optics and Quantum Electronics
Faculty of Science and Informatics
University of Szeged

Institute of Solid State Physics and Optics
HUN-REN Wigner Research Centre for Physics

Szeged, Hungary 2024

I am dedicating this thesis to my beloved late father,
who was looking forward to my success.

Table of contents

List of abbreviations

Area under the curve	AUC
Absorption coefficient	μ_a
Confocal Raman micro-spectroscopy	CRM
Diffusion coefficient	D
Dura mater	DM
Dimethyl sulfoxide	DMSO
Distilled water	DW
Fingerprint region	FP region
Glycerol	Gly
Glycerol-related Raman peak intensity	I_{gly}
Highest concentration of glycerol at saturation conditions	C_0
High wavenumber region	HWN region
Interstitial fluid	ISF
Inverse Monte Carlo	IMC
Optical clearing	OC
Optical clearing agent	OCA
Optical clearing efficiency	OC_{eff}
Phosphate buffered saline	PBS
Raman spectroscopy	RS
Refractive index	RI
Raman peak intensity before optical clearing treatment	I_0
Raman peak intensity after optical clearing treatment	I_{OC}
Relative refractive index	RRI
Relative glycerol concentration	TRGC
Scattering anisotropy factor	g
Scattering coefficient	μ_s
Stratum corneum	SC
Surface enhanced Raman scattering	SERS

Chapter 1: Introduction

The field of biomedical optics and biophotonics has emerged as one of the fastest-growing disciplines in basic life sciences and biomedical applications, including diagnosis, imaging, therapy, monitoring, and surgery. It permits functional and structural examination of tissues, organs and cells with imaging resolution and contrast unachievable by any other technique [1].

Light-based techniques, such as spectroscopy and optical imaging are widely accepted for the detection of physiological and pathological changes in cells and tissues by probing their optical properties *in vitro* and *in vivo* studies or even *in situ* [2]. Raman spectroscopy (RS) as one of the optical spectroscopic methods offers information about the molecular structure and conformation of biological objects, and gains great attention for diagnostics and monitoring in cosmetic and medical research [3–12]. It could be utilized as a non-invasive, label-free, non-destructive, and even non-contact tool in various areas such as physics, chemistry, biology, medicine and materials science. Additionally, RS has emerged as a promising alternative or complementary method to the gold standard method of tissue biopsy [13,14], which allows to assess the changes related to tissue conditions with minimum sample preparation and handling requirements [15].

RS provides valuable insights into the collagen structure and conformation related to different progressive diseases arising from collagen alterations, offering objective, quantifiable molecular information for diagnosis and monitoring [16]. For instance, RS can effectively discriminate between *dura mater* (DM) and meningioma based on Raman peaks correlated with the abundance of collagen in DM and on the increased lipid content in tumour [17–19]. Moreover, RS can monitor changes in collagen conformation within the skin-dermis related to disease or aging processes [20–22]. Additionally, RS has been utilized to evaluate collagen alterations in various human body sites such as heart valves [23], eye [24,25], lungs [26], epithelium [27], stomach [28], colon [29], and breast [30].

Biomedical optics and biophotonics including RS are suffering from strong light scattering or limited light penetration depth, posing a significant challenge for implementing optical techniques in clinical practice for diagnosis and monitoring of biological tissues and organs [31–33]. In the late 1990s, the optical clearing (OC) technique based on immersion of the tissue into an optical clearing agent (OCA) was introduced and developed in order to

increase the detection depth of optical techniques, as well as to improve the spatial resolution and contrast of the resulting images [33,34], by suppressing the light scattering within the biological objects. OC is recognized to be a promising technique to combine with the optical methods in the visible to NIR spectral range for clinical practice [35,36].

Currently, a diverse range of biomedical imaging techniques, such as RS [37], confocal Raman micro-spectroscopy (CRM) [38,39], 3D confocal microscopy [40], polarized microscopy [41], and optical coherence tomography [42,43], have the potential for common utilization in combination with various OCAs such as glucose [44], dimethyl sulfoxide (DMSO) [45–48], glycerol [49], *uDISCO* [50], *ScaleS* [51], and *Scale* [52] to increase sensitivity and reduce light scattering in order to enhance in-depth optical imaging resolution and contrast within biological objects.

However, the potential impact of OCAs on various biological tissues and their components, particularly collagen, raises concerns regarding their safety, and this aspect remains a subject of ongoing research. Furthermore, the effect of OCAs on the water content, the major component of biological tissues (up to 80% of their volume), has not been sufficiently investigated yet. Nonetheless, the main challenges are associated with the need to improve imaging resolution and contrast even more to the subcellular level for organs or larger tissue blocks [35].

The main motivation behind this thesis was to contribute to the knowledge and solutions related to the above mentioned unresolved issues and questions. In addition, the development of optical techniques in combination with optical clearing agents could pave the way for real-time molecular imaging within living cells.

The thesis aims to study the impact of optical clearing agent (OCA) on collagen in different biological tissues, such as *ex vivo* porcine *dura mater* and skin-dermis using in-depth confocal Raman micro-spectroscopy. Glycerol (Gly) was chosen as OCA being one of the most commonly used agents due to its efficiency, high refractive index, availability, biocompatibility, pharmacokinetics, biosafety, and low cost. The impact of this OCA in different concentrations on collagen-related Raman peaks, dehydration, dissociation, as well as its concentration and diffusion coefficient in-depth was thoroughly investigated using confocal Raman micro-spectroscopy.

To achieve the above mentioned goals, the following tasks were defined:

1- Investigate the changes in collagen-related Raman peaks after the application of the optical clearing agent (glycerol) to both *dura mater* and skin-dermis.
2- Examine the in-depth changes in collagen hydration and dissociation in the *dura mater* after treatment with an optical clearing agent.
3- Calculate the diffusion coefficient and concentration of the optical clearing agent in the *dura mater*.
4- Analyze the in-depth variation of water content relative to water hydrogen bond strength in the *dura mater* after the application of the optical clearing agent.
5- Investigate the effect of optical clearing on *ex vivo* porcine skin through in-depth monitoring of collagen-related Raman peaks using different excitation wavelengths of 633 and 785 nm.

The thesis has the following structure. Chapter 1 commences with an introduction that provides the motivation, relevance, and main objectives of the study. Chapter 2 contains the scientific background required for the understanding of results. Chapter 3 provides details on the materials and methods employed in the study. The results obtained during my PhD work are presented in Chapter 4. Chapter 5 concludes the thesis by summarizing of the major findings and provides prospects for the futures.

Chapter 2: Structure and chemical properties of the collagen

This thesis covers two topics: confocal Raman micro-spectroscopy investigations of *ex vivo* porcine DM and the skin dermis under the action of glycerol as an OCA. Therefore, this chapter summarizes basic information on these tissues, their optical properties and the impact of OC treatment.

2.1 Structure and chemical properties of collagen

Collagen is the main structural protein in mammals, and its structure and organization have been intensively investigated for more than half a century. It is located in the extracellular matrix of all multicellular animals, including sponges, invertebrates, and vertebrates. It is the major constituent of tendon, skin, DM, cartilage, bone, ligament, and other specific tissues providing tensile strength, tissue integrity, durability, and flexibility [53]. Collagen is comprised of a set of three polypeptide chains that possess a specific triple-helical structure and are organized into a fibrous network [53]. The various types of collagen fall into a selection of functional and structural subgroups [54,55], the most common types of collagen are listed in Table 2.1[56].

Table 2.1: *The five most common types of collagen [56].*

Type	**Location**
Type I	Dermis, tendon, ligaments and bone
Type II	Cartilage, vitreous body, nucleus pulposus
Type III	Skin, vessel wall, reticular fibres of most tissues (lungs, liver, spleen …)
Type IV	Basal lamina, the epithelium-secreted layer of the basement membranes
Type V	Lung, cornea, hair, fetal membranes and bones

The most abundant are the fibril forming, interstitial collagens with collagen type I covering about 90% of the body's collagen [53]. The tropocollagen (collagen molecule) is their major unit, which self-assembles into microfibrils, forming a collagen fibrils network and being about 300 nm in length for collagen type I (see Figure 2.1A) [57]. It's found in the skin dermis and DM in high proportion about 85–90% and >90%, respectively.

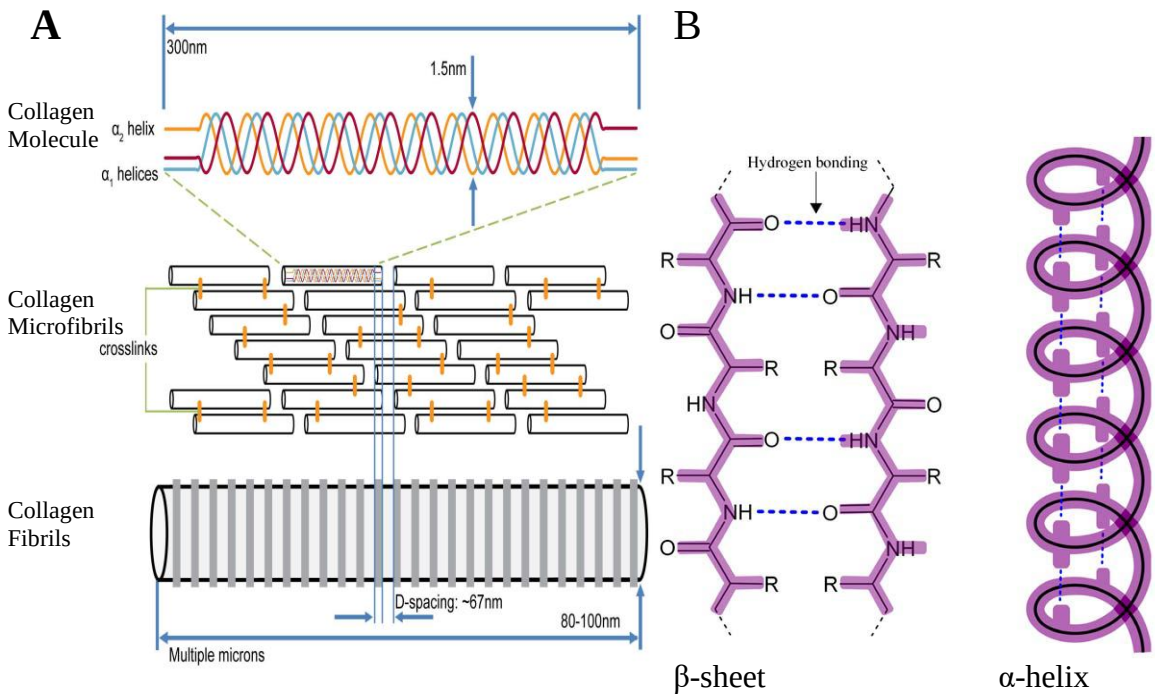

Figure 2.1: *Collagen type I structure: (A) schematic illustration of the three various structures that form a collagen fiber [57], and (B) the two most common protein secondary structures, where the backbone chains (purple outline) interact with hydrogen bonding (blue dashed lines). R denotes to the side chain [58].*

Similar to all proteins, collagen's structure describes its properties and interactions with other molecules and cells in the biological tissue. Collagen is assembled from several amino acids (primary structure) that serve as building blocks ((C_α─C(=O)─N)) to form a polymer chain. The proteins were comprised of a linear structure due to covalent bonds between the amino group of one amino acid and the carboxyl group of another [58]. In the amino acid chain, the interaction of side chain groups (R) with the backbone defines the secondary structure [58]. Figure 2.1B illustrates the two most common types of protein secondary structure, the β-sheets (anti-parallel) and the α-helices.

Collagen conformation of a specific triple-helical structure is stabilized by two different types of hydrogen bonds. These hydrogen bonds could be direct or indirect (more frequently) through the involvement of water molecules (see Figure 2.2) [59]. Consequently, water molecules perform an essential role in preserving collagen's structure. It's worth to notice that two water molecules could be hydrogen bonded with the same carbonyl group [60].

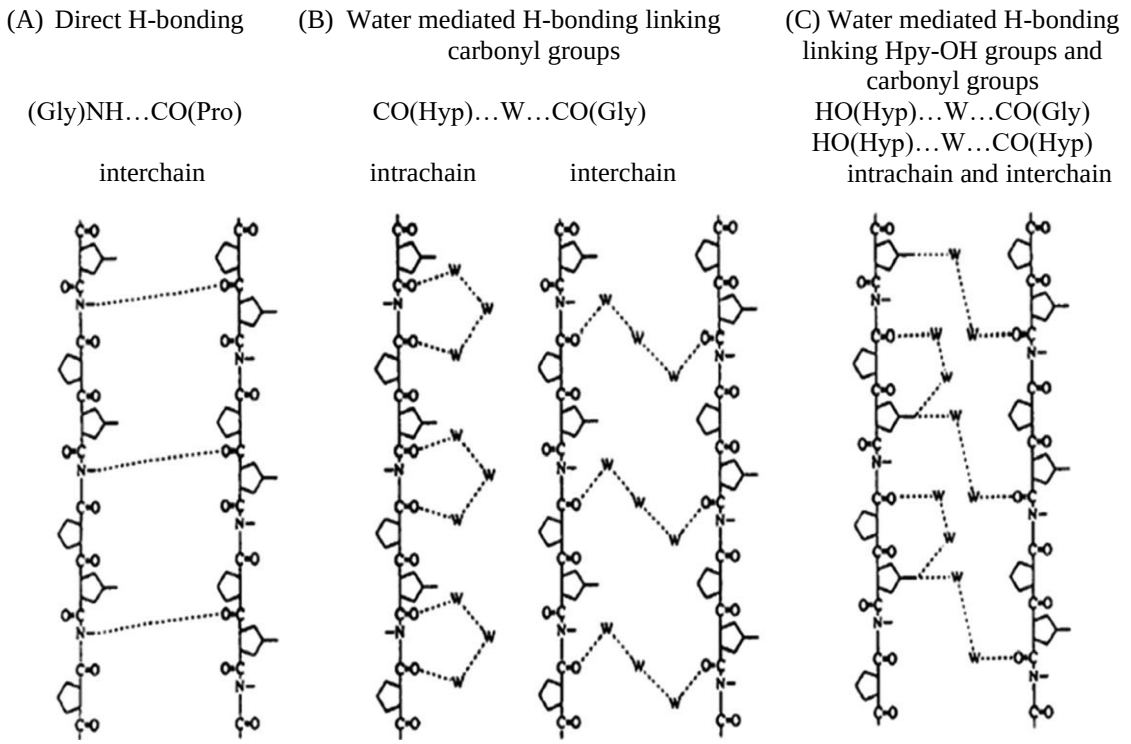

Figure 2.2: *Graphic representation of the collagen structure stabilized by hydrogen bonding: (A) direct hydrogen bonding; (B) water-mediated hydrogen bonding linking carbonyl groups and (C) water-mediated hydrogen bonding linking hydroxyproline OH and carbonyl groups [59].*

2.1.1 Dura mater

Dura mater (DM) is the upper layer of the meninges and is securely connected to the skull bone [61], serving as a protective tissue covering for the mammalian brain. While the mechanical properties of the brain have been intensively studied, the meninges layers have frequently ignored [62]. The meninges plays a significant role in the central nervous system, brain traumatic injury, and forensic medicine [63]. From a structural point of view, DM is a dense and tough connective tissue composed of a network of collagen fibrils [64], constituting more than 90% of its thickness. The average diameter of collagen fibrils is approx. 100 ±5 nm (see Figure 2.3) [65], with a refractive index (RI) of 1.47, while that of the interstitial fluid (ISF) is 1.34 at 589 nm wavelength [66].

DM is composed of two layers: the first layer is the periosteal layer (uppermost layer), which is directly attached to the bone surface and comprises nerves and a vascular network. This layer is characterized by elongated fibroblasts with a large intercellular matrix. The second layer is the meningeal layer (middle layer), which exhibits a higher fibroblast density and a lower concentration of collagen fibrils compared to the periosteal layer [67].

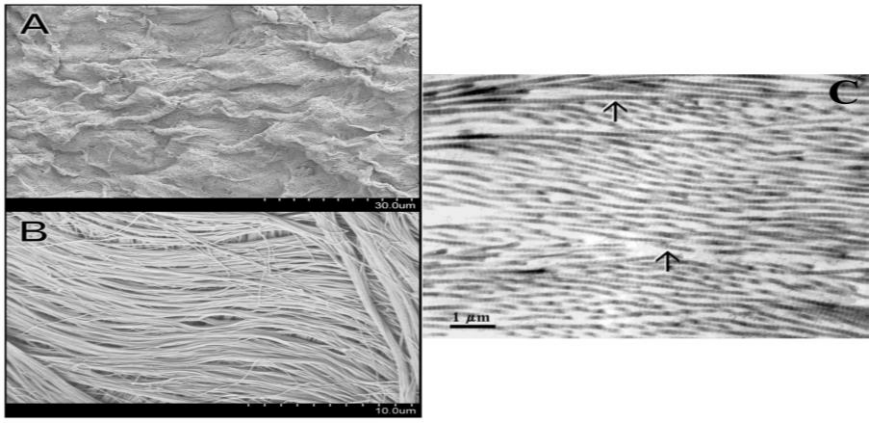

Figure 2.3: *(A) The arachnoid surface layer, (B) the bone surface layer [63], and (C) collagen fibril layers owning an alternating orientation [65].*

However, it is important to mention that these layers of DM are functionally and anatomically linked to each other, forming a single layer without any distinct boundaries [65]. Due to the similar structure of collagen in DM, its optical properties are comparable to the dermis of the skin and the sclera of the eye. The presence of a blood vessels network in DM is the only distinguishing feature from the sclera [68].

The study of the effect of OCA on the optical properties of collagen-DM results in an appropriate non-destructive technique for visualize blood vessels of the brain surface and the brain itself, to enhance the assessment of human head injuries related to meninges, and to increase in-depth imaging [69]. In addition, studying the collagen structure of DM is essential for developing and enhancing of biomedical materials for collagen-based tissues [53], which are widely accepted in applications such as graft tissues and implantable smart devices for therapy [70–72]. As mentioned above DM is comparable to other collagen-rich biological tissues and organs, such as the sclera of the eyes and the dermis of the skin. Therefore, the results obtained for DM could be translated into these biological tissues and organs (to the dermis of the skin in this case).

2.1.2 Skin

Skin is a complex multi-layered organ that covers most of the human body, with an approximate surface area of 1.5–2 m^2. It plays an important role in biochemical and mechanical protection against exogenous agents [73]. Skin consists of three major layers: epidermis, dermis and subcutaneous fat [74–77], as illustrated schematically in Figure 2.4. The skin has an efficient barrier function against the penetration of pathogens, light exposure damage, maintains human body temperature, and regulates water loss [4,78–80].

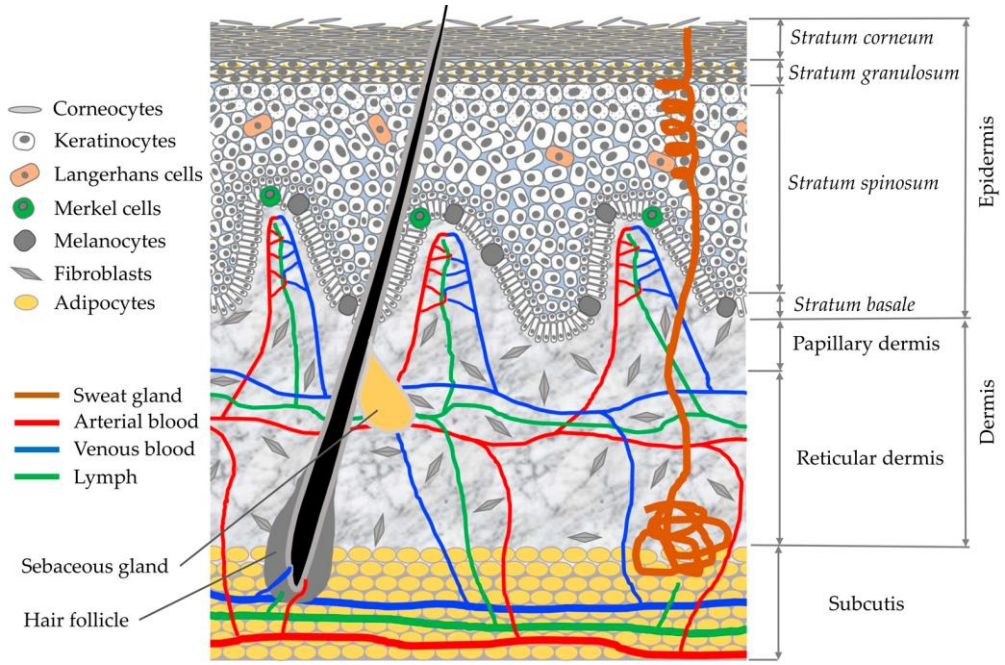

Figure 2.4: *The different layers of the skin tissue* [80].

The epidermis is first and outmost layer of the human skin (including stratum corneum, stratum lucidum, stratum granulosum, stratum spinosum, and stratum basale). It serves as an efficient barrier function against the penetration of pathogens, light exposure damage, maintains human body temperature, and regulates water loss. The epidermis contains keratin filaments and melanin, the primary skin constituents responsible for scattering and absorbing light, respectively. Additionally, these components participate in water binding and regulating water diffusion [81–86].

The dermis, the largest and second layer of the skin, is a dense connective tissue composed of collagen fibers and the interstitial fluid (ISF), which comprises proteoglycans, proteins, protein-polysaccharide complexes, and water [74–76,87]. It contains two distinct layers: the papillary layer and the reticular layer, which can be distinguished by the size of collagen fibers and their blood content [74,76,88]. Collagen is the most abundant constituent in the dermis, comprising about 80% of its total dry weight and 90% of all dermal protein [89]. More specifically, collagen type I is one of the most common proteins in dermal layers [20,22], which supplies great tensile strength and tissue integrity to skin, among other functions.

The subcutaneous adipose tissue, also known as hypodermis, is the lowest layer of the skin, which consists primarily of connective tissue and fat cells (adipocytes) that containing lipids (stored fat) in the form of isolated small droplets. These lipids are mostly composed by triglycerides. The lipid content of a single adipocyte accounts for about 95% of its volume

[88,90,91]. This layer is actively involved in maintaining homeostasis, protecting the organs from physical external damage and the body from heat loss.

Nearly all biological tissues possess high scattering properties, which strictly limit the imaging depth of optical spectroscopic methods. OC method has been suggested to reduce light scattering and increase light penetration depth and became a hot topic of research. Collagen is the primary constituent responsible for light scattering in biological tissues [65,92,93]. Collagen type I is one of the most fundamental components of DM and skin dermis and its Raman analyses can be better understood after OC treatment. Observing the changes in collagen type I configuration and its interactions with OCAs, water, and other substances holds significant potential for clinical applications.

2.2 Raman spectroscopy

2.2.1 Principle of Raman spectroscopy

Raman spectroscopy is one of the optical spectroscopic method that offers insights into the molecular structure and conformation of biological objects non-destructively, attracting considerable attention in cosmetic and medical research for diagnostic and monitoring purposes [3–12]. The Raman scattering effect was discovered in 1928 by C.V. Raman, who was the first one detected and explained the inelastic light scattering and received the Nobel Prize for it in 1930 [94].

The scattering of light on molecules can be either an elastic or an inelastic processes. In elastic scattering, the incident and scattered photons have identical energy (as observed in the most light-tissue interactions, known as Rayleigh scattering). Inelastic scattering, on the other hand, involves energy exchange between the incident photon and the scattering molecule, resulting in a shift in the energy of the scattered photon. This effect is employed in biophotonic methods including Raman scattering microscopy and coherent anti-Stokes Raman scattering [1,95].

Raman scattering is an inelastic scattering event that excites the vibrational modes of molecules, resulting in two distinct outcomes: Stokes and anti-Stokes scattering (see Figure 2.5A). In Stokes scattering, the molecule is excited from the ground state to a higher vibrational energy level, and the energy of the scattered photon is lower than that of the incident one; as a result, the scattered light has a longer wavelength. On the other hand, anti-Stokes scattering happens when an incident photon interacts with a molecule that relaxes to a lower vibrational energy level and transfers some energy to the photon; as a result, the

scattered light has a shorter wavelength. At room temperature, most of molecules reside in their ground states. Consequently, the probability of the anti-Stokes scattering events are very low, and as a result, the Stokes scattering constitutes most to the RS.

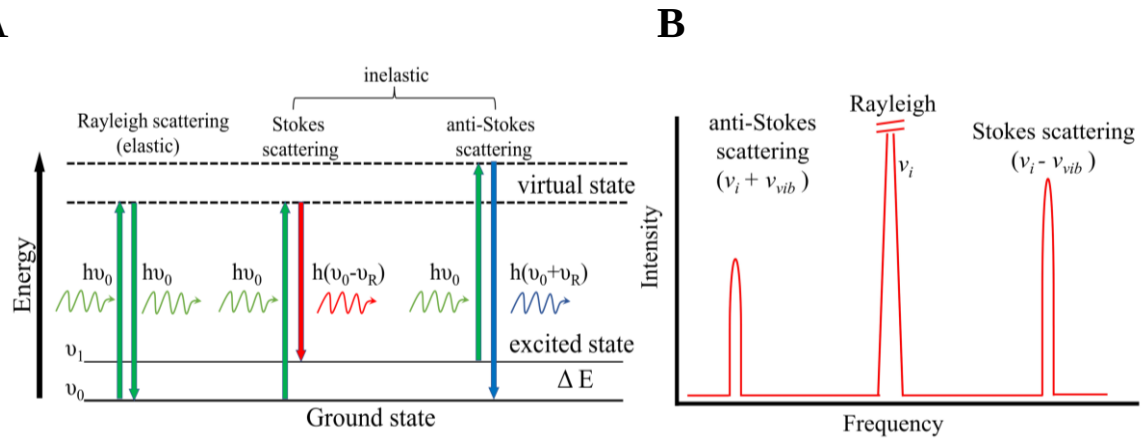

Figure 2.5: *(A) Schematic of the Rayleigh and Raman scattering processes (Stokes and anti-Stokes), and (B) the relations of the photon frequencies of the different processes.*

RS utilizes monochromatic laser light to excite the molecules within biological tissues or objects, allowing for precise measurements of wavelength shifts between incident and scattered light (see Figure 2.5B). In a Raman spectrum, the x-axis reflects the relative change in photon energy for the various Raman peaks and is given in Raman shift or wavenumber units (cm^{-1}). Raman shift quantifies the difference of the wavenumbers of the incident and scattered photons, calculated according to the formula:

$$\Delta\nu\ (cm^{-1}) = (\nu_0 - \nu_R) \quad (1)$$

where ν_0 and ν_R are the wavenumbers of the incident and Raman scattered photons, respectively.

RS has become an essential tool for examining biological tissues, applicable not only *ex vivo* but also *in vivo*, due to obvious advantages such as being label free, non-invasive, non-destructive, sensitivity, and specificity [7,95–97]. However, RS faces limitations in terms of the small penetration depth due to strong tissue scattering, along with the complexity or impossibility of distinguishing the obtained spectra signal from different depths [32,98]. This obstacle was overcome by the integration of RS and confocal microscopy, forming what is known as confocal Raman micro-spectroscopy (CRM). This advancement made it possible to acquire Raman spectra in-depth [99]. It is worth to mention that the amount of the scattering molecules is directly proportional to the number of bonds in the tissue molecules [1,96,100].

2.2.2 Raman spectroscopy in the biological tissue

RS of biological tissues and objects offers molecular signatures that reveal the chemical conformation of different tissue constituents, including proteins, lipids, nucleic acids, and carbohydrates [10,19,101–104]. Within RS, the Amide I and III regions are frequently utilized to detect alterations in the secondary structures of collagen, along with the regions associated with lipids, proline and hydroxyproline regions [16]. Figure 2.6 summarizes these three key regions involved in the conformational changes of collagen structure, with corresponding assignments presented in Table 2.2 [105–108].

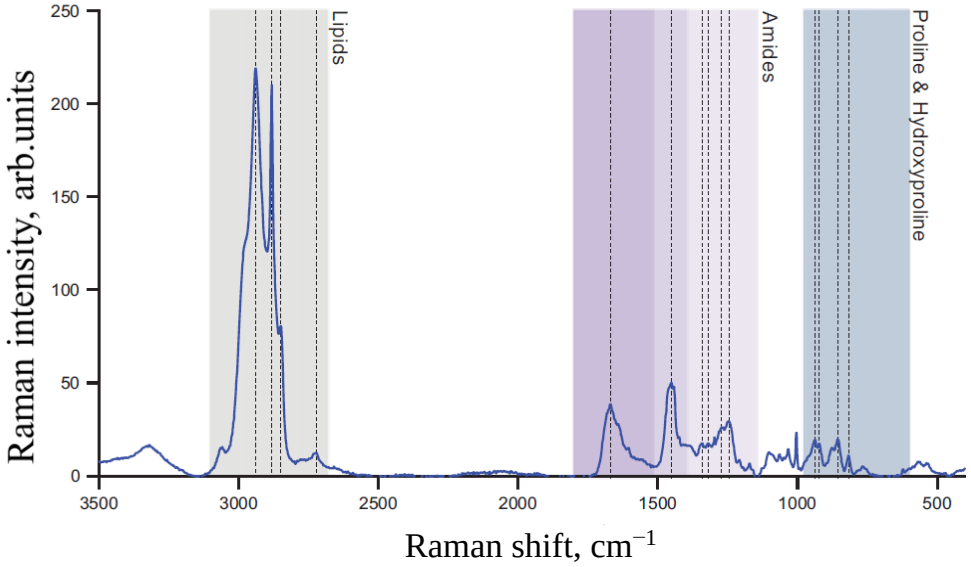

Figure 2.6: *Typical Raman spectrum (an average of 60 spectra) of collagen structures. The peaks in the highlighted three major spectral regions frequently reflect conformational changes [16].*

Table 2.2*: Main Raman peaks of collagen structures* [105–108].

Region	Raman shift, cm^{-1}	Assignment
Amides I, II, III	1666	C═O stretching of amide bond (peptide bond)
	1450	NH_2 deformation of amide bond (peptide bond)
	1340	CH_2 scissoring
	1319	CH_3, CH_2 twisting
	1271	N-H deformation of amide bond (peptide bond)
	1245	C-N stretching of amide bond (peptide bond)
Proline & Hydroxyproline	936	C-C stretching of protein backbone
	921	C-C stretching of Pro/Hypro ring
	855	C-C stretching of Pro/Hypro ring
	816	C-C stretching of protein backbone
Lipids	2939	C-H stretching vibration
	2881	CH_2 asymmetric stretching
	2849	CH_2 symmetric stretching
	2721	C-H stretching vibration

Numerous approaches can analyze the collagen molecule, but only a limited number can analyse modifications in its molecular structure. Moreover, these approaches often involve destructive sample and require labeling [16]. On the other hand, RS offers a label-free, non-destructive and non-invasive method for examining biological objects [3–12].

RS has emerged as a valuable tool for unraveling collagen structures and conformation related to different progressive diseases caused by collagen molecule alterations [16]. For instance, RS can discriminate between DM and meningioma based on Raman peaks correlated to rich collagen content in DM and on increased lipid content in tumour [17–19]. It also has the potential to monitor changes in collagen conformation in skin-dermis related to disease or the chronological aging process [20–22].

Other studies have employed pure collagen to identify distinct Raman spectra for each collagen type, including collagen type I, IV [20], and VII [109]. Additionally, RS has examined collagen type I to revealed specific Raman peaks that are sensitive to the surrounding water environment and the molecule's conformation [22,89]. Collagen modifications related to diseases have been reported, including those associated with chronological aging, UV light exposure, cancer progression, and alterations in mechanical, physical, and biochemical characteristics [20,21,89,110,111]. Moreover, RS has been used to examine changes in collagen molecules in various human body sites such as heart valves [23], eye [24,25], lungs [26], epithelium [27], stomach [28], colon [29], and breast [30].

RS exhibits unique vibrational peaks for each substance, and its intensity is directly proportional to the concentration of the substance [112]. This remarkable property makes RS a promising quantification system. RS has proven to be a sensitive technique for quantitative or semi-quantitative monitoring the penetration profiles of xenobiotic into biological objects [113–120]. Caspers *et al.* [121] have suggested a new technique for fully quantifying the concentration of a substance applied into the skin utilizing *in vivo* CRM. This novel approach based on a linear correlation between molecule concentration and the generated Raman intensity, employing various calibration approaches and mathematical formulas to estimate the mass ratio of the permeant (mg) per protein (g) based on the corresponding Raman intensity ratio.

Recently, Choe *et al.* [122–124] displayed the remarkable capability of a tailored multivariate curve resolution alternating least squares (MCR-ALS) method for calculating skin constituents and concentrations of topically administered substance *in vivo*. For further penetration kinetics fitting and quantitative analysis, various mathematical algorithms, such as non-negative matrix factorization [125], non-negative constrained least squares approach

[126], and classical least squares analysis [115] have shown the ability to translate Raman data into concentration information.

The in-depth Raman signals attenuation due to refraction, dissipation, and strong scattering in biological tissues significantly distorts the data. However, this attenuation effect can be mitigated by correlating a substance's Raman peak to a protein-related Raman peak as an internal reference, thereby equalizing the signal attenuation [114,118,127–129]. This approach enables monitoring substance penetration relative to a specific component of biological tissue.

For instance, Franzen *et al*. [129] utilized unspecific methyl deformation vibration in the frequency interval from 1388 to 1497 cm^{-1} as an internal reference for quantitative caffeine analysis with its controlled concentration in-depth in human skin. Alonso *et al.* [130] correlated the caffeine-related Raman peak to Raman peaks of amino acids and amide I in skin (1004 and 1650 cm^{-1}, respectively). The keratin-related Raman peaks at 1450 and 1650 cm^{-1} can also be utilized as a normalized peak reference [131]. However, the assumption of homogeneous skin-derived Raman peak intensities as an internal reference remains uncertain, especially considering the skin's extremely complex composition as a biological object. Additionally, different studies have employed varying skin Raman peaks as reference. Consequently, a comprehensive study and assessment of this analytical method are missing [129,132].

Similarly, the thesis aims to determine the optimal protocol for OCA quantification using CRM. To address this gap, I investigated the suitability of the Raman peak correlation approach, considering the influence of different protein-related Raman peaks as reference and their potential role in quantifying OCA in tissue depth using the passive diffusion model described in Section 3.5.

Water is an important component for living organisms, actively participates in cellular metabolism and contributes to skin hydration [133]. It is the major component of biological tissues and objects (nearly 80% of their volume). CRM is considered an effective tool for precisely evaluating water mass percentage in skin [134,135]. Huizinga *et al.* [136] proposed an approach using CRM to calculate in-depth water profiles in the eye, employing the ratio of Raman peaks of water (3350-3550 cm^{-1}) to protein (2910-2965 cm^{-1}) in HWN region. Caspers *et al.* [99] further customized this approach for *in vivo* skin. Nakagawa *et al.* [137] demonstrated the effectiveness of CRM in calculating water profiles up to 200 μm depth in the dermis *in vivo*.

Vyumvuhore *et al.* [138] utilized Raman OH band deconvolution Gaussian function–based in the range of 3100-3700 cm^{-1} to assess different types of total water molecules (primary-bound water, partially-bound water, and free water) in extracted SC of the skin. Currently, for the first time, Choe *et al.* [139] showed identification of the distribution of different mobility states of water in the *in vivo* SC of human skin. Their findings showed that strongly hydrogen-bonded (double donor-double acceptor) and weakly hydrogen-bonded (single donor-single acceptor) water account for more than 90% of total skin water content, while tightly hydrogen-bonded (single donor-single acceptor) and free water types represent the remaining <10%. However, it was found that collagen type I provide certain Raman peaks that are sensitive to the water environment and alterations in collagen-bound water [22,89]. In this thesis, the impact of OC on the profile of different types of water molecules (see Table 2.3) in *ex vivo* porcine DM up to a depth of 200 μm was investigated using the deconvolution method suggested in the literature [138–140] (Section 4.2).

Table 2.3: *The four water molecules states.*

Raman shift, cm^{-1}	**Assignment**
3005	Tightly-bound (DAA–OH)
3277	Strongly-bound (DDAA–OH)
3458	Weakly-bound (DA–OH)
3604	Free water (sum of unbound (free OH) and very weakly bound (DDA–OH) water)

Light scattering in collagen-rich tissues is primarily caused by ubiquitous collagen fibers [65,92,93], significantly limiting the effectiveness of light-based techniques like spectroscopy and optical imaging. As explained earlier, collagen is one of the most prevalent component in the DM and skin-dermis, and its Raman spectroscopic examine can be better understood after OC due to reduced light scattering in depth. Certain OCAs are capable of destabilize the collagen structure due to interactions between collagen and an OCA through hydrogen bonds. This leads to an anticipated reduction in light scattering from collagen-rich tissues due to a decrease in scatter size [141]. Understanding the mechanisms that drive collagen structure alterations during OC is of paramount importance to the medical community. In this study, I utilize CRM to explore the interactions between collagen-rich tissues (DM and skin-dermis) and OCAs, elucidating the roles of water content, RI matching, and collagen dissociation effects. In addition, the diffusivity of OCAs in collagen-rich tissue was investigated in the framework of a passive diffusion model.

2.3 Optical properties of tissues and light propagation

The interaction of light with biological tissue is a complex process due to the intricate structure of its constituent materials, which are multicomponent, multilayered, and optically inhomogeneous. The fundamental light-tissue interactions include reflection at the tissue interface, refraction, absorption, and scattering within the tissue, and transmission through the tissue. When light enters a medium, it undergoes attenuation, arising from two main mechanisms: scattering and absorption. The extent to which a photon is scattered or absorbed within a medium is determined by the optical properties of that medium (in our case, biological tissue), specifically, the absorption coefficient (μ_a) and the scattering coefficient (μ_s).

The optical absorption coefficient (μ_a) represents the fraction of the radiant flux Φ (λ) absorbed in a medium over a unit distance (L) of the beam path [32,36]. It is measured in units of inverse length (cm^{-1}) and follows the expression:

$$\mu_a(\lambda) = -\frac{1}{\Phi}\frac{d\Phi(\lambda)}{dL} \quad (2)$$

Biological tissues are inherently heterogeneous materials composed of different constituents. Consequently, the overall optical properties of biological tissue arise from a composite of the particular properties of the tissue's constituents. Some of the most prevalent biological tissue constituents include proteins, lipids, blood, and water [35]. These biological tissue constituents exhibit absorption bands at distinct wavelengths. The μ_a for the spectral range from 200 to 1200 nm for water, lipids, hemoglobin, and other chromophores is illustrated in Figure 2.7 [142].

The absorption of light in biological tissue is dependent on its molecular constitution. Generally, hemoglobin and melanin are two key absorbing substances in biological tissues. Hemoglobin is a pigment (globular metalloprotein) responsible for oxygen transport from the lungs to the body [1]. The skin dermis is richly vascularized and thus contains a high concentration of hemoglobin [77].

Melanin, the main chromophore that imparts colour to human skin, eyes, and hair, mainly resides in the epidermis. As depicted in Figure 2.7, the absorption coefficient of melanin exhibits a monotonic decrease from the UV toward the infrared spectrum [1]. Besides hemoglobin and melanin, other chromophores, such as bilirubin, carotenoids [143,144], fats [143], cell nuclei, and protein filaments [145] also contribute to light absorption in biological tissues [146].

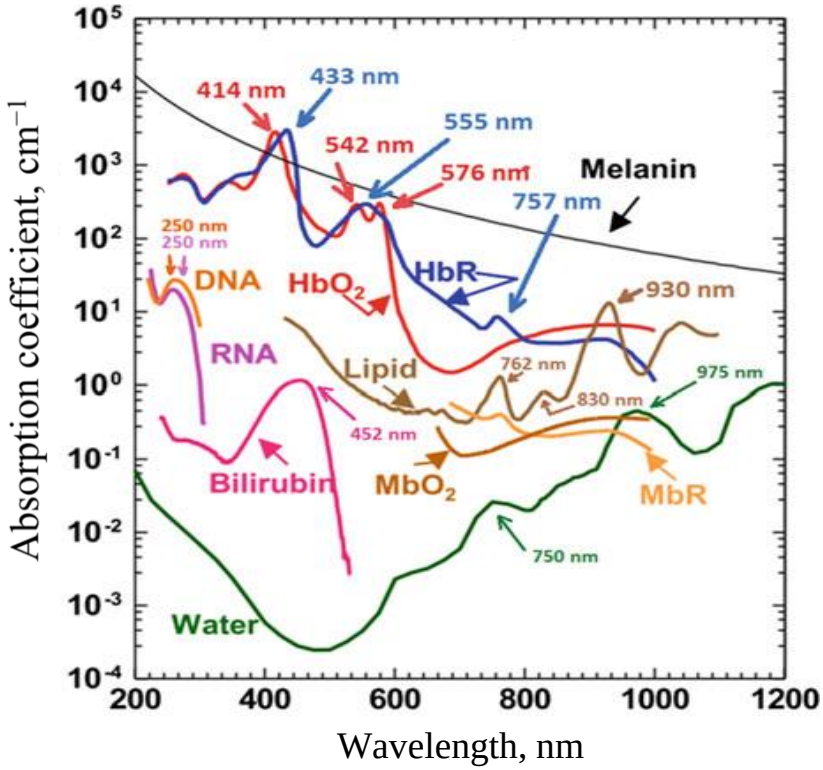

Figure 2.7: *Absorption coefficient (μ_a) of some constituents of biological tissues* [142].

Despite their high concentrations in all biological tissues, water and lipids (non-chromophores) don't exhibit substantial absorption in the visible region of the spectrum. The overtones of their vibrational modes mainly occur in the near-infrared region, leading to significant absorption there. Optical measurement of their overtone bands gives information about the local abundance of molecules, offering valuable insights for the diagnosis and therapy of tissue states [35,146].

The scattering coefficient (μ_s) represents the attenuation (T) of a collimated beam when traveling through a medium (non-absorbing medium) [32,35,36], It is measured in units of inverse length (cm^{-1}) and follows the expression:

$$T(\lambda) = \exp(-\mu_s(\lambda)L). \quad (3)$$

Light scattering in biological tissue is strongly influenced by the wavelength, sizes of structures, and RI of biological tissue constituents that contribute to scattering (cell membranes, collagen fibers, connective tissue, nervous tissue, muscle tissue, organelles, etc.) as shown in Figure 2.8 [1,35,146]. The primary constituents responsible for scattering in skin are protein filaments. In the skin epidermis, this is mainly keratin, while in the dermis layer [92] and in the DM [65,93], it is collagen. Melanosomes, cell nuclei, and cell walls also contribute minimally to photon scattering [147–149].

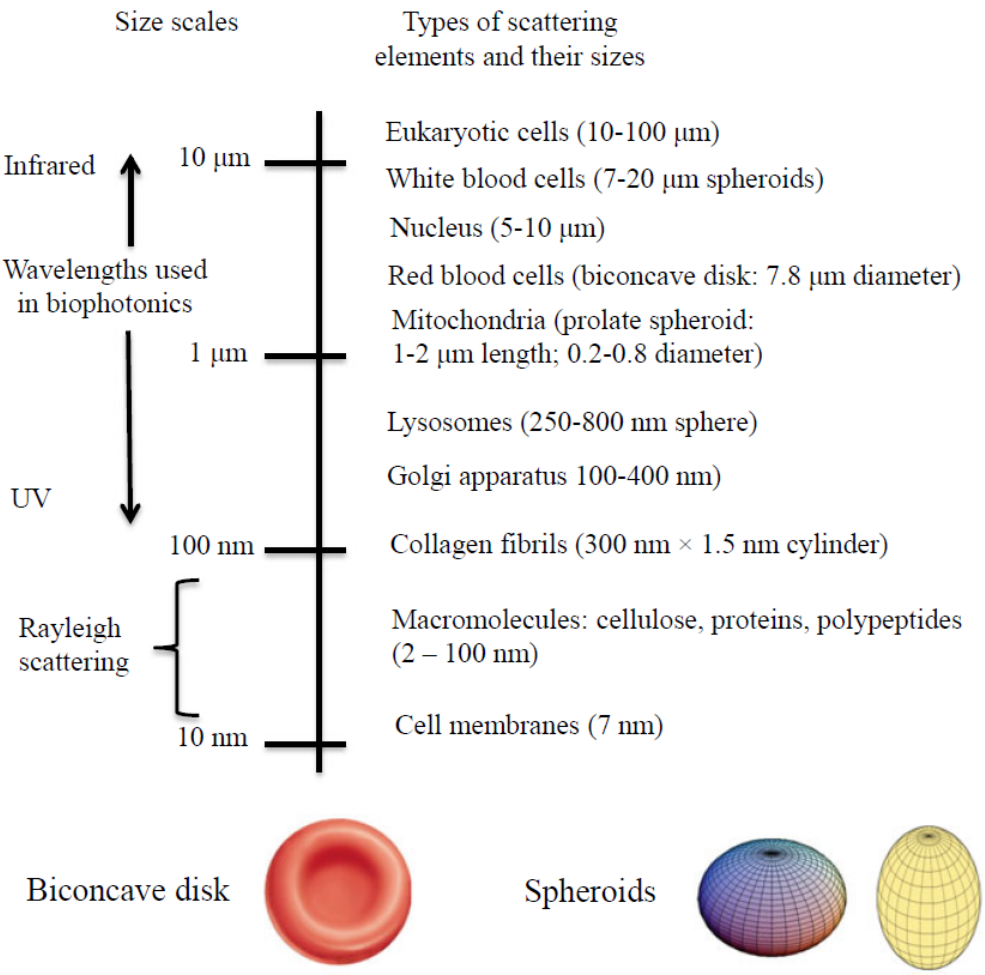

Figure 2.8: *Size and type of objects being main scatterers for different wavelengths in biological tissues [1].*

Scattering processes are commonly utilized in biophotonics applications for clinical diagnosis and therapy. For instance, disease-induced alterations in tissue can influence the scattering properties, thereby offering diagnostic markers for distinguishing healthy and diseased tissue. Together, the absorption and scattering of photons lead to the broadening of the light beams and intensity decline during in-depth penetration through the tissue.

Finally, the refractive index mismatch between tissue constitution is the last optical property of paramount importance [1,35,146]. The RI determines the speed of light propagation in a medium and how the direction of light changes as it passes through the boundary between media [150]. Having c = 2.998 × 10^8 m/s and v as the light speed in vacuum and biological tissue, respectively, the RI of the tissue (n_{tissue}) is determined as [36]:

$$n_{tissue} = \frac{c}{v} \tag{4}$$

Multiple light scattering happens when photons interface a material having a RI that differs from that of the surrounding medium. The RI for the visible and infrared (Vis-IR) wavelengths range has been experimentally measured for a wide spectrum of different biological tissues, as well as their main constituents (for example, connective tissue collagen [151], organelles in mammalian cells [152], oxygenated and non-oxygenated hemoglobin [153,154], etc.). The average RIs of biological tissues range from 1.34 to 1.62, which significantly exceeds the RI of water at 1.33. Table 2.4 provides a list the RIs for various tissue components.

Table 2.4: *RIs of different tissue components. The starlike indicates a significant value range in literature source* [1,146].

Tissue component	**Refractive index**
Water	1.33
Extracellular fluid	1.34 –1.35
Intracellular fluid	1.35 –1.36
Proteins	1.40*
Lipid	1.45*
DNA	1.44 –1.49*
Bilipid membrane	1.46
Melanin	1.65
Cytoplasm	1.35 –1.37
Epidermis	1.34–1.43
Human liver	1.36–1.38
Mitochondria	1.38–1.41
Tooth enamel	1.62–1.73
Whole blood	1.35–1.39

For biological tissues, the μ_s is primarily determined by the RI mismatch between the cellular tissue constituents (organelles, membranes, nuclei, etc.) or scleroprotein fibrous structures, muscle or cartilaginous tissues and ISF [155]. It is worth to mention that for biological tissues the μ_s values are typically much greater than the μ_a values. All of the aforementioned parameters contribute to the tissue's optical properties and influence the in-depth probing capabilities of optical imaging and diagnostic methods, which are strongly wavelength-dependent. This basically means that the wavelength of light employed for a given treatment or diagnosis must be carefully selected.

2.4 Tissue optical clearing mechanisms

The rapid advancements in the OC method offers a new perspective for 3D imaging of biological tissue [156–159]. Recent advances in optical imaging and OC that enable modification of tissue optical properties have led to enhanced photodynamic therapy response in the treatment of cutaneous melanoma in mice down to depth at 750 μm. After OCA

treatment, tumors exhibit greater optical homogeneity due to RI matching, resulting in improved photodynamic therapy response through enhanced light penetration and distribution [160]. Raman spectra analysis of the main biochemical changes in OCA-treated tumor (proteins, lipids and nucleic acids) demonstrates that topically applied of OCA prior to tumor irradiation leads in more homogenous, deeper and better photodynamic therapy treatment in depth layers. Moreover, a single-cell OC technique for plasmonic nanoprobes imaging using hyperspectral dark-field microscopy has been developed. This technique based on a combination of RI matching and delipidation with highly biocompatible and cost-effective agents. Delipidation is achieved by administration a mild delipidation solvent and is monitored using stimulated Raman scattering, enabling elimination of lipid-enriched granular structures that impede OCA penetration [161].

As explained earlier, the major factor restricting the potential use of light-based techniques, such as spectroscopy and optical imaging in biological tissue, is the significant light scattering, which drastically reduces the spatial resolution, contrast, and scanning depth. The primary contributor to high light scattering in biological tissue is the mismatch of RI between the scatterers (such as protein fibers, nuclei, cell membranes, organelles, and lipid droplets) and the ISF (mostly composed of water). Furthermore, the cellular cytoplasm also mostly comprises of water, suggesting heterogeneity in optical properties at the intracellular level [32,35,36].

The relative refractive index (RRI) of biological tissue, determined by the ratio of the RI of tissue scatterers ($n_{scatter}$) to the RI of the ISF (n_{ISF}), which allows to approximate the degree of tissue scattering. For instance, the RI of collagen, the primary constituent of connective tissue, and relies on its degree of hydration, is calculated as 1.47 [162]. Melanin, which is abundant in skin, has an RI of 1.65, while the RI of ISF ranges from 1.35 to 1.37 at a wavelength of 589.6 nm. Notably, the RRI for skin exceeds unity for these two scatterers (collagen and melanin). Consequently, the scattering probability for photons traversing skin is exceptionally high due to the large number of such native scatterer/ISF interfaces with RI mismatches. The high tissue scattering is likely to decrease if RRI value is equal/close to 1. While it is challenging to reduce the RI of tissue scatterers to match that of the ISF, Tuchin suggested a method for immersion OC of biological tissues [36], which involves modifying the n_{ISF}.

The OC technique depends on the utilize of biocompatible, commonly hyperosmotic chemical agents named optical clearing agents (OCAs). The tissue OC method offers a novel approach to enable in-depth tissue imaging, diagnosis, and therapy by making biological

tissues or objects more transparent and reducing light attenuation by applying different OCAs [35,163]. Tissue OC mechanisms, based on the main chemical or physical principles, comprise reduction of light scattering and absorption through the matching of RI and pigment removal in biological tissues, respectively. These mechanisms result from chemicals-biomolecules interactions (including dehydration, hyperhydration, collagen dissociation, delipidation, and decalcification for matching of RI and decolorization for removal of pigments) (see Figure 2.9). It is well established that biological tissue is composed of different constituents, containing proteins, lipids, water, mineral compositions, and numerous molecules. The concentration of these components varies among different tissue types. Therefore, the diverse OC mechanisms are likely the outcome of complex interactions between tissues and OCAs [164–166].

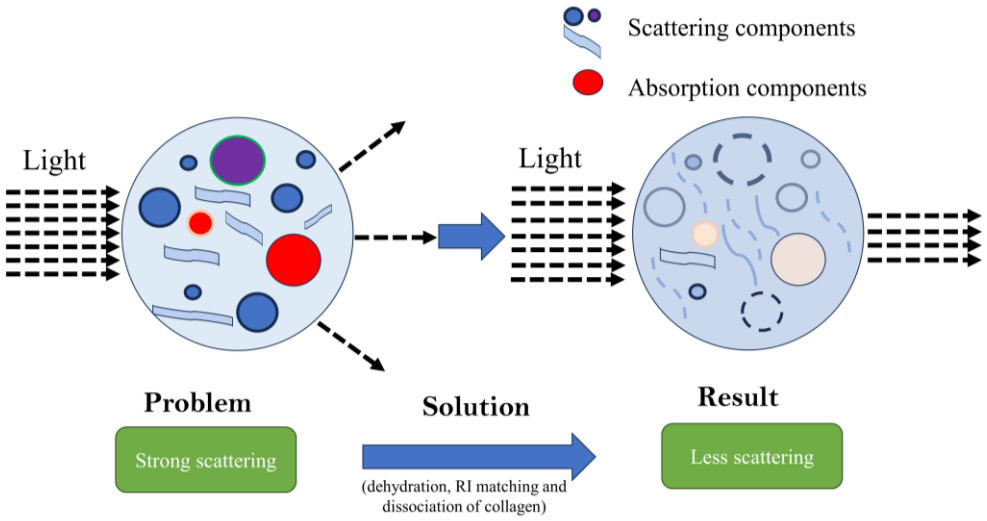

Figure 2.9: *Tissue optical clearing principles.*

In recent years, the scientific community has recognized three main hypothesized mechanisms of OC in biological tissues and objects [31,33]. The first mechanism involves tissue dehydration caused by the hyperosmotic properties of OCAs [32,66,141,167–170]. The second mechanism aims to match the RI difference between the various constituents of biological tissues and ISF as a result of the penetration of the OCA into the biological tissue [32,33,51,52,87,167,169,171–173]. The third mechanism related to the process of (reversible) dissociation of collagen during its interaction with the OCA.[171,174–177].

Numerous studies have demonstrated that tissue dehydration is one of the essential mechanisms for tissue OC [31,172,178,179]. When biological tissue samples are immersed *ex vivo* or topically applied *in vivo* with such chemical agents, they exert an osmotic pressure on

the tissue, leading to a change in the natural concentration gradient of water inside the tissue. Unbound water molecules in the intercellular space flows outside of the tissue due to this osmotic pressure. This efflux of water molecules out into the external environment, the samples become more organized. Consequently, The sample thickness reduces and the scatterers will be compacted [32,35,36,66,180,181]. In other words, the concentration of scatterer per unit volume increases, potentially leading to an increase in tissue scattering. On the other hand, the overall transmission and tissue transparency can enhance due to the reduced tissue thickness and more organized packing of scatterers (tissue shrinking) [66,181]. It's important to notice that strong osmotic pressure can cause irreversible destruction of the tissue structure (OCA toxicity) [182].

The RI mismatch between scattering particles and the background medium (ISF and/or cytoplasm) leads to significantly light scattering in biological tissue [66]. Introduction chemical agents with high RI into biological tissue and/or the outflow of water molecules from the tissue due to the agent's hyperosmolarity could increase the RI of the background medium [35,180,181,183]. This could happen in parallel with tissue dehydration, as water molecules could flux out from the tissue and the hyperosmotic agent molecules also diffuse into the tissue [31,32,172,33,34,51,52,87,167,169,171]. This RI matching can reduce scattering and make the tissue more transparent.

In accordance with this concept, OCAs with higher RIs are expected to provide better OC efficiency in biological tissues. For fibrous tissues like the DM and dermis of skin, The RI matching process is prioritized over dehydration, since strong tissue dehydration is feasible only when applying hyperosmotic agents, although the molecule size of OCA is much less than the average value of the interfibrillar space [33,34,167,184]. It is worth to notice that biological tissues are densely packed with various substance, containing scattering particles with higher RI (1.39–1.52) and a background medium with lower RI (1.33–1.37). It's important to mention that due to the complicated structures of biological tissues, the interactions between different OCAs and tissues are extremely complex, preventing a comprehensive understanding of OC processes [185].

This process contributes to the destabilization of protein structure (reversible) through the interaction of hydrogen bonds between collagen and OCA. Collagen is one of the major scattering structures in biological tissue, arranged into complex fiber structures (see Section 2.1). The OCA-induced dissociation of the collagen structure is due to the interfering of the OCA with the hydrogen bonds that hold the collagen structure together. Accordingly, the application of OCAs with multiple hydroxyl groups, possessing strong electronegativity, may

destabilize the higher-order collagen structure and induce its dissociation. Reducing the size of main scattering particles (collagen dissociation) leads to a substantial reduction in light scattering in tissue [168,186]. Nonetheless, this effect could be simply reversed due to the non-covalent nature of hydrogen bonds in collagen triple helices [172,187]. For instance, the dissociation of collagen fibers in *in vitro* immersion with OCAs was studied using the second harmonic generation imaging (see Figure 2.10) [174]. The collagen fibrous structure is clearly visible before glycerol (OCA) treatment (Figure 2.10A). After the addition of glycerol, the dermis of rodents becomes more optically transparent, and the fibrous structure unravels into a matted morphology (Figure 2.10B). Upon the removal of excess glycerol and subsequent treatment with PBS, the collagen fibrous structure recovers (Figure 2.10C). However, the impact of glycerol on *in vivo* rat skin during the OC process did not result in collagen dissociation or fractionation. Instead, only a decrease in the diameter of protein fibers and skin thickness is observed, attributed to water loss [141].

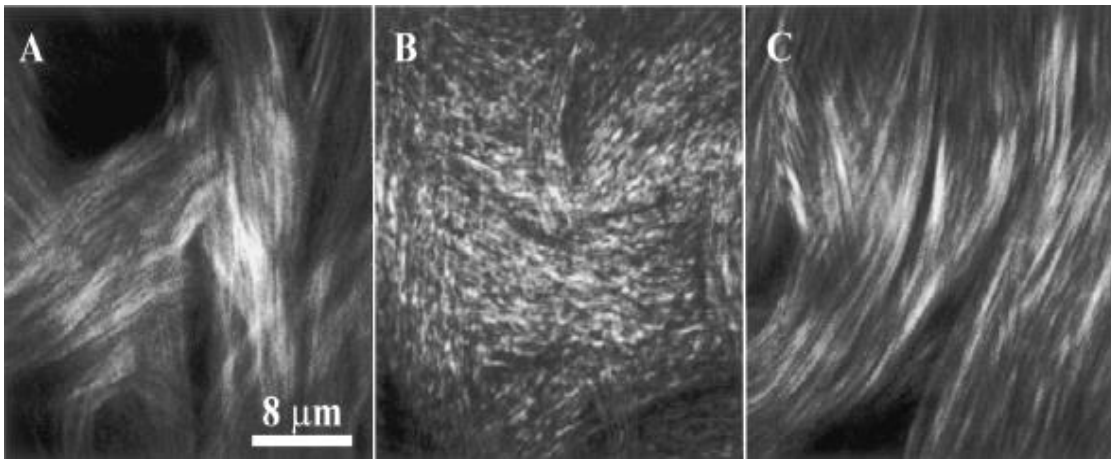

Figure 2.10: *Second harmonics generation image showing the reversible effect of glycerol on the dermis of rodent (A) before and (B) after glycerol treatment, and (C) after treatment with PBS (rehydration)* [174].

2.4.1 Optical Clearing Agents (OCAs)

The OC efficiency in biological tissues depends upon various factors, including the RI, concentration, osmolarity, and physicochemical properties of the OCA. Additionally, the parameters related to the biological tissue, such as its initial turbidity and permeability for the molecules of a selected OCA, play a crucial role in determining the effectiveness of the OC process. In addition, when conducting *in vivo* studies, the efficiency of OC may be influenced by various physiological properties of the tissue. Factors such as the metabolic response of living tissue to the OCA, temperature, and functional aspects (such as the degree of blood

supply and the presence of the lymphatic system) can impact the outcomes [32,33,66,170,172,188–191]. Moreover, the RI of living tissue is subject to variations based on its physiological and pathological state.

In recent years, extensive research has been conducted on various substances and their combinations for use as OCAs in biological tissues. Currently, OCAs for immersion applications for *ex vivo* and *in vivo* studies can be categorized into the following five groups:

1- **Polyatomic alcohols**: glycerol, polyethylene glycol, polypropylene glycol, combined mixtures on the base of sorbitol, polypropylene glycols, polyethylene glycols, xylitol and mannitol, etc. [65,141,183,188,190,192–201];
2- **Sugars**: glucose, fructose, ribose, sucrose, dextrose, and saccharose, etc [65,184,193,202–208];
3- **X-ray and magnetic resonance contrast agents**: Verographin™, Trazograph™, Hypoque™, Omnipaque™ , Gadovist, Magnevist and Dotarem [38,135,209–211];
4- **Organic acids**: oleic and linoleic acids [212,213];
5- **Other organic solvents**: DMSO, and thiazon [45,47,149,171,212–219].

All these OCAs are generally considered to be non-toxic. However, it's important to note that prolonged exposure to OCAs can lead to some negative effects. These may include local hemostasis (impairment of blood flow), tissue shrinkage, and, in extreme cases, necrosis (cell death) in living tissue [169,220]. Therefore, careful consideration of exposure times and concentrations is essential to minimize these potential side effects when applying OCAs to living tissues. Currently, the most popular and frequently used OCAs for biological tissues are Gly, glucose, and PEG due to their efficiency, availability, biocompatibility, pharmacokinetics, biosafety, and low cost [35,167,169,214,221–223]. However, the effectiveness of OCAs does not directly rely on their RI only, but also on the molecular structure features that influence the interaction of the OCA with biological tissue components [192,199].

The first group of OCAs comprises common polyhydric alcohols with similar molecular structures characterized by the existence of more than one hydroxyl-group. Their hydrophilic and hyperosmotic properties induce dehydration and shrinking of biological tissue, leading to a reduction in light scattering [31–33,35,172]. Additionally, the OC efficacy of these OCAs directly depends on the number of hydroxyl groups (more hydroxyl groups result in better OC efficacy) [192]. This is described by their potential to disrupt and screen

the hydrogen bonds in collagen triple helices, initiating the dissociation of the collagen structure.

Another approach to enhance the OC efficiency of the skin involves increasing its permeability for OCAs by facilitating their penetration through the SC into the deeper layers. DMSO is a penetration enhancer that not only diminishes the barrier function of the SC but can also act as an OCA itself [45]. As a chemical enhancer, DMSO can potentially alter the intercellular conformation of keratin from an α-helical to a β-sheet and disrupt the structural stability of the lipid bilayer, thereby facilitating the penetration of OCAs into the deeper layers of the skin [36,45,224,225]. Generally, the SC substantially minimizes the mobility of OCAs penetration into the skin layers, and the use of permeation enhancers can substantially improve the efficiency of the OC process.

Thus, a crucial and challenging task remains identifying the optimal OCA, along with determining its optimal concentration and exposure time, to enable safe and effective *in vivo* imaging of living tissues. Further investigation is essential to identify OCAs with the most favorable and safest parameters under optimal experimental conditions. This complex endeavor is integral to advancing the OC of biological tissues and objects.

2.4.2 Raman spectroscopy combined with tissue optical clearing

A significant advancement in both RS and OC method has enabled the solution of a complex challenge: through-skull imaging of the cortex vasculature of a mouse brain under a transparent skull window at a depth of over 850 μm. This technique also allows for the analysis of compositional changes in the skull before and after OC application using RS [226]. Additionally, this approach simultaneously facilitates the mapping of metabolic dynamics of lipid and protein synthesis in glioblastoma [227].

Moreover, numerous studies have demonstrated the impact of different OCA concentrations and exposure times on the in-depth changes of tissue-related Raman peaks. For instance, it was observed that topical application of Gly solution to porcine skin can increase the in-depth Raman peak intensity by 2-4 times at a depth of 400 μm [228]. Further, the OC effects using different concentrations of 40%, 60%, and 80% Gly solutions were explored. The findings revealed that an increase in Gly concentrations led to improved OC efficiency and Gly treatment contributed to the recovery of skin tissue Raman spectra, which not overlapped with the Gly-related Raman spectra over time. In work [229] examined the effect of Gly solutions with different concentrations and exposure times on the effectiveness of the

OC process in in-depth RS of intact *ex vivo* porcine skin Raman spectra. It was found the best OC efficiency was achieved by applying a combination of 60% Gly and 40% water after a 45 min treatment (3.4-fold enhancement at 80 μm depth). However, studies [38,228,230] have demonstrated that the use of an OCA enhances the signal-to-noise ratio, improves the Raman signal quality, and reduces the systematic error that can arise from inaccurate determination of the surface and sub-surface spectra of the probing sample.

Others have conducted comparative studies between different OCA types such as polyatomic alcohols and x-ray computer tomography agents. The effects of 70% Gly and 100% Omnipaque™ 300 solutions as OCAs were investigated on *ex vivo* porcine skin [38]. The intensity of Raman peaks was significantly increased at depths below 160 μm with Omnipaque™ 300 treatment. In contrast, with 70% Gly treatment, the increase in Raman peak intensity was observed at a depth of 40 μm after 60 min of treatment. Furthermore, the study examined the influence of these OCAs on collagen hydration within the dermis. Both OCAs were shown to induce skin dehydration, but the effect was significantly more pronounced with Gly. In addition, a study investigated the OC effect of three different OCAs (Gly, polyethylene glycol, and Omnipaque™) on *in vivo* human skin using portable fiber optic RS [231]. Skin-related Raman peaks were significantly increased for all three OCAs, indicating the OC effect. However, the effectiveness of OC varied with different concentrations of the agents, and the kinetic curves were specific to the concentration of each OCAs. It was also observed that the OC effect diminished during the initial 10–20 min, likely due to the dehydration.

The Raman signal is significantly influenced by elastic scattering [232,233]. Therefore, it is worth to notice that high concentrations and long exposure time of OCA could significantly reduce scattering, leading to a loss Raman signal due to reduction of light interaction length. Thus, it is necessary to seek a compromise during the OC process between the Raman signal attenuation in the absence of scattering for highly turbid media and the Raman signal enhancement for strongly transparent ones [232,234]. Therefore, it is crucial to find the most suitable and biocompatible OCA, as well the optimal exposure time and concentration that optimizes the OC process and Raman signal intensity for effective *in vivo* tissue analysis at maximum depths using Raman methods. In this regard, the use of penetration enhancers in combination with traditional OCAs like DMSO [225], hyaluronic acid [235], or oleic acid [213] can significantly accelerate the OC process.

Due to the strong scattering in biological tissues and objects and the weak intensity of Raman scattering, the resolution and contrast of Raman spectra from deeper layers are

reduced. Approaches based on Surface Enhanced Raman Scattering (SERS) have attracted great attention, allowing for a substantial enhancement in Raman measurement sensitivity and extending its applications into deeper layers [204,236–239]. In work [240], for the first time, the OC method was proposed to support SERS *in vivo* imaging. The highest efficiency was achieved with a multicomponent OCA of fructose, PEG-400, and thiazone, which provided a 3.5-fold higher improvement in OC effect compared to fructose after 15 min of treatment. At the same time, utilizing SERS *in vivo* imaging in combination with the OC method revealed the feasibility of enhancing and expanding the clinical applications of handheld Raman detector for deeper tissue layers studies.

In work [241], it was shown that applying the OC method increased the SERS signal-to-background ratio by 5-fold and allow a reduction in the total bioimaging time by at least 10-fold without significant signal loss from *in vivo* subcutaneous tumor phantom. The SERS bioimaging combined with the OC method made it possible to clearly determine the shape, size and boundaries of the *in vivo* subcutaneous phantom, which was previously impossible to observe without the OC method. Due to the high efficiency of the OC method, it could be accelerate the clinical prospects of using SERS for preoperative bioimaging of subcutaneous tumours.

Chapter 3: Materials and methods

This chapter is divided into five sections. The first section presents the OCAs used for the experiments. The second section describes sample preparations of different biological tissues (porcine *ex vivo dura mater* and skin). The third section shows the confocal Raman micro-spectroscope used in this study. The four section explains the data analysis methods. The final section elaborates on the mathematical model based on passive diffusion.

3.1 Optical clearing agent

In this thesis, glycerol was used as an OCA due to its efficiency, high RI, widespread availability, biocompatibility, pharmacokinetics properties, biosafety, and affordability — making it one of the most commonly used OCAs [170,198]. Gly is a water-soluble triatomic alcohol comprising three carbon atoms covalently bound to the hydroxyl-group (see Figure 3.1A). It is worth to mention that a 50% Gly solution is considered safe for *in vivo* human applications [242]. Moreover, Gly has demonstrated the potential to reduce intracranial pressure and brain tissue edema in stroke patients [243–245].

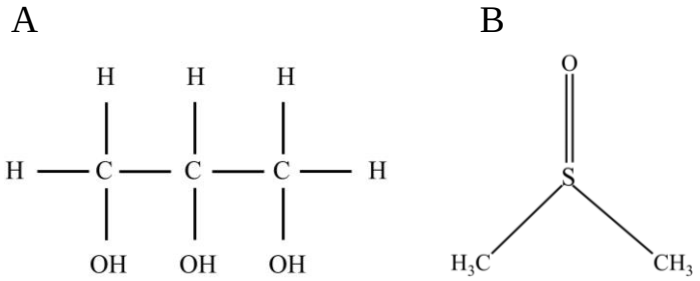

Figure 3.1: *Chemical structure of (A) glycerol and, (B) DMSO.*

For the *ex vivo* porcine DM study, we used 99.0% purity Gly (Sigma-Aldrich Ltd.) to investigate the impact of high concentration of Gly on collagen (see Section 4.1). Furthermore, Gly solutions ranging from 0 to 50% (v/v) were prepared in distilled water (DW), using ≥99.7% purity Gly (VWR chemicals, Belgium). These solutions served as the foundation for creating a calibration curve to determine the relative Gly concentration (TRGC) in the treated DM. Subsequently, the 50% Gly solution was utilized to estimate the diffusion coefficient, concentration, and its impact on various hydrogen bonds in the DM tissue (Section 4.2).

For the *ex vivo* porcine skin study, Gly of 99% purity (Sigma Aldrich, Ltd.) was used. It was found that ≈70-80% (*v/v*) Gly diluted in DW gives the most efficient OC process [38,246]. Therefore, a mixture of 75% glycerol + 25% DW, and another of 75% glycerol + 20% DW + 5% DMSO were employed as OCAs. DMSO (Fisher chemical, Belgium) was utilized as the penetration enhancer, which decreases the SC barrier function and is also used as an OCA by itself (see Figure 3.1B). [45]. The RIs of different OCA mixtures used in this study are listed in Table 3.1.

Table 3.1: *Refractive index of OCA solutions used for this study.*

OCA mixtures	RI
99% Gly	1.47
75% Gly + 25% DW	1.43
75% Gly +20% DW + 5% DMSO	1.44
50% Gly + 50% DW	1.41

3.2 Sample preparation

In this work, fresh *ex vivo* porcine tissues were used to study the impact of OC. Porcine DM serves as a suitable model for conducting *in vivo* investigations of human DM, taking into consideration features such as housing, gross anatomical structure, feasibility, and ethical concerns [67,247,248]. Additionally, porcine ear skin exhibits histologically, morphologically, and immunohistochemically similarities to human skin [249–252]. All samples were delivered to the laboratory on the day of sacrifice from a local accredited slaughterhouse (Albertirsa, Hungary). Figure 3.2 summarizes the sample preparation, immersion in OCAs and experimental setup, which explain in details next sections.

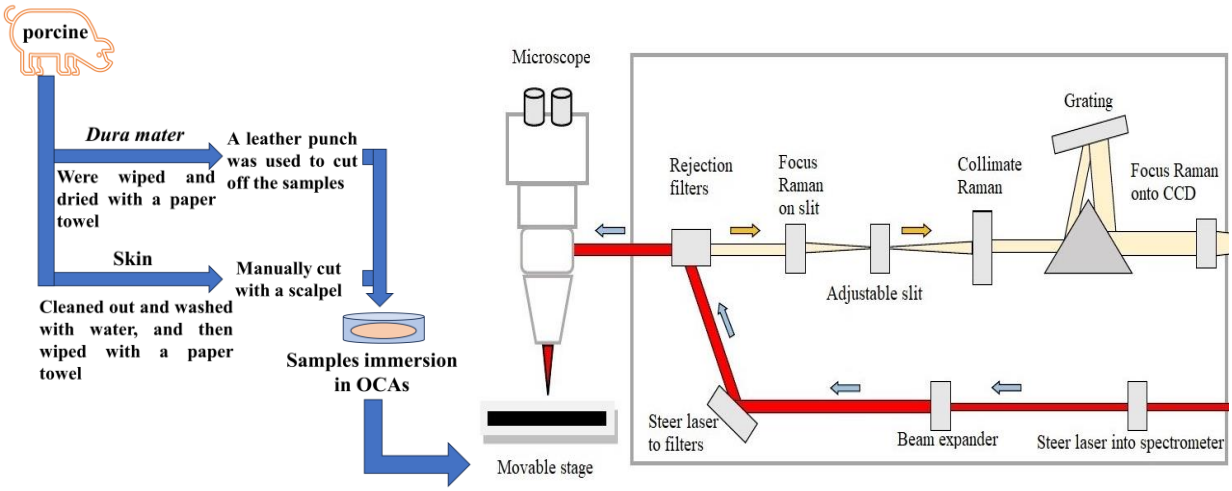

Figure 3.2: *Schematic representation the experimental setup of the inVia Raman microscope and the sample preparation.*

3.2.1 Dura mater preparation

All freshly harvested *ex vivo* porcine DM samples were obtained on the day of slaughter from a local accredited abattoir (Albertirsa, Hungary) and maintained cold on ice in PBS (Sigma Aldrich) during transportation to the laboratory. To study the effect of Gly in high concentrations on collagen-DM (see Section 4.1), twelve *ex vivo* porcine DM samples were gently wiped and dried with a paper towel prior the measurement. The sample size was 22 mm^2 and the thickness was approx. 0.5 mm. A leather punch was used to cut off the samples. Subsequently, the samples were immersed in a bath of 5 mL of 99.0% Gly (see Figure 3.3) for different treatment times: 5, 10, 15, and 30 min in Petri dishes. A DM sample without treatment was considered as a reference. The thickness of each sample was measured before and after OC treatment using a digital micrometer. CRM measurements were conducted by locating the DM samples on a silicon wafer for easier handling, and Raman spectra were obtained through the outer endosteal layer of the DM.

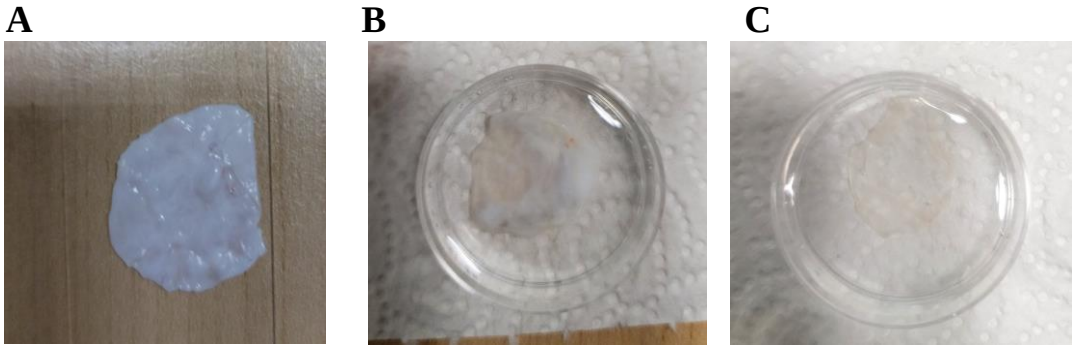

Figure 3.3: *Dura mater sample (A) before treatment and after immersion in 99% Gly for (B) 5 min and (C) 30 min.*

Furthermore, we studied the impact of a moderate concentration of Gly (see Section 4.2). For these experiments the DM sample was cleaned using a paper towel. Then, a leather punch was utilized to excise sample sections of 13 mm^2 in size and 0.4±0.08 mm in thickness, which was measured with a digital micrometer prior to treatment. Finally, the samples were secured beneath the metal ring to ensure stabilization and prevent the %50 Gly solution from flowing downward from the lateral border of the sample, guaranteeing uniform treatment (see Figure 3.4). Four and six DM samples were utilized to acquire Raman spectra in the FP and HWN regions for each depth, respectively (total sample count = 40 for all depths). All measurements were acquired on the upper endosteal DM layer.

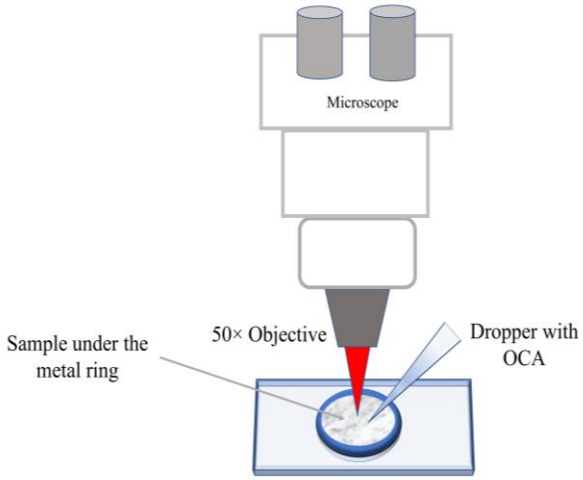

Figure 3.4*: Graphic represent of the experimental setup of Dura mater measurement using CRM.*

3.2.2 Skin preparation

To study the effect of OC (see Section 4.3), measurements were made on *ex vivo* four fresh porcine ear skin samples (see Figure 3.5).

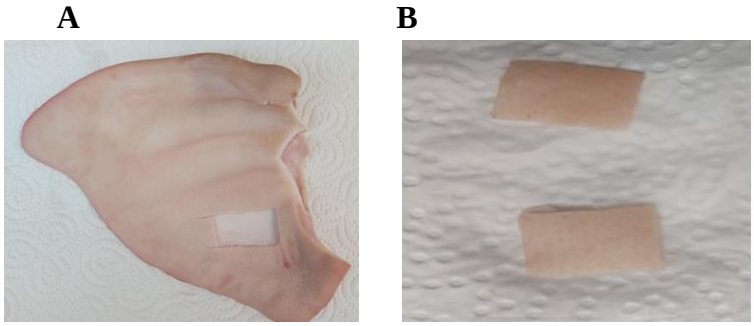

Figure 3.5: *(A) Ex vivo porcine ear, and (B) skin samples from porcine ear.*

Before the measurement, the skin was thoroughly cleaned with water and then wiped dry with a paper towel. Furthermore, to increase the penetration of OCAs into the deeper layers of the *ex vivo* porcine skin, the hair was shaved off, and the skin was subjected to 20 tape stripping to remove the outermost layer on the surface. Subsequently, the skin samples were defatted by placing them in a bath of pure ethanol for 5 seconds. These procedures routinely employed on skin before examination, contribute to reduced backscattering from the SC. Thus, a greater amount of light could be penetrate into deeper skin layers, enabling the monitoring of Raman scattering from these regions. Consequently, Raman spectra from deeper skin regions could be collected.

The skin sample size was 1×1 cm^2 and the thickness was approx. 1.2 mm. It was manually cut with a scalpel and kept in a refrigerator for no more than two days at 5 °C.

Before the measurements, the samples were allowed to acclimatize to the laboratory for 30 min at a temperature of 20 ± 1°C. Finally, the skin samples were immersed in bath containing the different OCAs for 30 and 60 min in Petri dishes. The skin sample without OCAs treatment served as a reference. It is worth to mention that even with 60 min of treatment, the exposure time was not sufficient for the OCAs to fully penetrate into all skin layers from both the dermal and epidermal sides [211,253]. All Raman measurements were recorded by locating the samples on a silicon wafer for better handling and performed through the epidermis.

3.3 Experimental setup

Raman spectra were acquired for the fingerprint (FP, 400-1800 cm^{-1}) and high wavenumber (HWN, 2700-3800 cm^{-1}) regions using backscattered geometry by Renishaw inVia^{TM} confocal Raman microscope in static mode. All samples (DM and skin) were mounted on the motorized *xyz*-axis stage of the Raman microscope permitting automatic vertical displacement with micrometer resolution to acquire z-scan profiles in-depth (see Figure 3.6).

***Figure 3.6**: Renishaw inVia Raman micro-spectrometer used for the Raman measurements.*

The laser power delivered to the surface of the sample was maintained at 10 mW and 50 mW for 633 and 785 nm, respectively, which is considered non-destructive for biological objects [254]. The system was calibrated using 520 cm^{-1} Raman band of a silicon wafer before acquiring the Raman spectra. All the obtained data were recorded under the same conditions at a room temperature of 20 ± 1°C.

Table 3.2 summarizes the main parameters for the Renishaw inVia^{TM} systems. The Raman spectra were displayed by the relevant versions of the Renishaw WIRE software installed on the computer.

Table 3.2: *The Raman microscope devices main parameters used for the measurements.*

Laser source	633 nm	785 nm
Spatial resolution	0.77 μm	0.95 μm
Laser power	10 mW	50 mW
Objective	50×	
Exposure time	5 s for fingerprint region 1 s for high wavenumber region	5 s for fingerprint region
Accumulation	1	
Grating	1200 l/mm	
Motorized *xyz*-axis stage step size	0.1 μm in the XY direction 0.2 μm in the Z direction	
Detector	1024 x 256 pixel CCD	

It is important to recognize that both laser sources have their own strengths and limitations. Firstly, different wavelengths exhibit varying degrees to penetration into biological tissues. In fact, when a laser with a shorter wavelength penetrates the biological objects, it experiences more significant light attenuation, resulting in a reduction in Raman intensities compared to a laser with a longer wavelength [255]. In this regard, the 785 nm laser source offers higher scanning depth. Secondly, the natural pigmentation of biological tissues can lead to fluorescence, increasing the background noise in the Raman spectrum [256]. Consequently, Raman peaks excited at 633 nm may be more susceptible to overlapping with a stronger fluorescence signal in the FP region. Moreover, the intensity of Raman peaks is inversely proportional to the fourth power of the wavelength. Therefore, a laser with a shorter wavelength could be potentially enhance the sensitivity of the Raman measurements.

Additionally, the response of CCD detectors is significantly reduced in the near-infrared wavelength region due to their quantum efficiency characteristics (sensitivity). This can lead to weaker detected Raman signals, particularly in the high wavenumber (HWN) region, which is crucial for calculating water concentration and lipid characterization in biological objects [135,257]. Therefore, a 633 nm laser can be used for both the FP and HWN regions simultaneously. Moreover, from a practical perspective, using a 633 nm excitation wavelength is advantageous for medical diagnostics and treatment. Visible lasers are easier to visualize during surgery, enabling surgeons to identify and remove tumors based on their vibrational features.

3.4 Data analysis

The Raman spectra obtained from each depth of the samples (DM and skin) were averaged and the data presented as mean ± SEM. The averaged spectra were then processed using the Spectragryph software [258]. This processing included baseline subtraction using an adaptive algorithm and an advance smoothing using a Savitzky–Golay filter with a third-order polynomial and a 9-point interval. Principal component analysis was performed to decrease the number of low variability components of the obtained Raman spectra. The Renishaw WIRE software with a built-in algorithm performed the principal component analysis with the first four principal components [114,259]. Due to the advancement of CRM and the benefits of rational decomposition of Raman spectra, a combination of Gaussian and/or Lorentzian peaks has become a common practice for analyzing Raman spectra. In order to acquire biochemically and reproducible results, the full widths at half maximum and the maximum shift of the sub-band were authorized for vary within 20 cm^{-1} and 5 cm^{-1}, respectively. The quality of the fit was assessed using the R-Squared values.

3.5 The mathematical model based on passive diffusion

As explained earlier, the optical properties of biological tissues are altered due to modifications in their micro-structures and scattering components after permeation by OCA having higher RIs than the ISF of the tissue. Various biological tissues have varying diffusion coefficient based on the features and behavior of the OCAs. Consequently, numerous studies have focused on controlling the optical properties of the biological tissue by evaluating the diffusion coefficients of OCAs [65,87,170,180,200,209]. For this reason, a mathematical model based on passive diffusion was utilized to estimate the OCAs diffusion coefficients for fibrous tissue like dermis, sclera, DM, and muscles [260].

Given the fibrous structure of these tissues, it is reasonable to presume that the dynamics of fluid diffusion within these tissues can well be adequately explained by free diffusion. To perform in-depth analysis of fluxes and concentration profiles under *in vivo* and *in vitro* conditions, Fick's second law of diffusion could be a good starting point:

$$\frac{\partial C(z,t)}{\partial t} = D\frac{\partial^2 C(z,t)}{\partial z^2}, \tag{5}$$

Where $C(z,t)$ is the concentration of OCAs at depth z (cm) and in time t (sec); D is the diffusion coefficient (on the hypothesis that it is a constant in the whole tissue volume), in cm^2/sec.

This formula holds true when the process rate is unlimited across the tissue sample or when a substance in solution has a high rate of permeation through tissue sample. Another assumption is that the OCA penetration into a sample does not modify its concentration outside the tissue (in the external volume). The corresponding boundary condition is:

$$C(0,t) = C_0 = const, \quad (t > 0), \tag{6}$$

Where C_0 is the concentration of OCA in the external volume. The initial condition relates to the OCAs absence inside sample before its application:

$$C(z,0) = 0, \quad (z > 0), \tag{7}$$

for all points inside of the tissue sample before treatment.

From the Laplace transform, the problem of diffusion can be considered in a semi-infinite medium. Considering z is the reference variable, by treating with Laplace transform of $C(z,t)$ to p:

$$\overline{C}(z,p) = \int_0^\infty e^{-pt}\, C(z,t)dt, \tag{8}$$

The term in the square bracket vanishes at $t = 0$ under the initial condition Eq.7 and at $t = \infty$ through the exponential factor. Thus Eq.8 reduces to:

$$p\overline{C} = D\,\frac{d^2C(z,p)}{dz^2}. \tag{9}$$

In the Laplace transform, the variable p is a complex parameter, by treating the boundary condition Eq.6 in the same way we obtain:

$$\overline{C}\big|_{z=0} = \int_0^\infty C_0\, e^{-pt}dt = \frac{C_0}{p}. \tag{10}$$

Then the solution of Eq.5 when satisfying the condition of Eq.10 is

$$\overline{C} = \frac{C_0}{p}\, e^{-z\sqrt{\frac{p}{D}}} \tag{11}$$

By applying the inverse Laplace transform, the solution of Eq.11 for tissue depth z at the moment t with boundary condition Eq.6 and initial condition Eq.7 can be obtained as

$$C(z,t) = C_0 erfc(x) = C_0(1 - \frac{2}{\sqrt{\pi}}\Big(x - \frac{x^3}{1!3} + \frac{x^5}{1!5} - \frac{x^7}{1!7} \ldots\Big), \tag{12}$$

$$x = \frac{z}{2\sqrt{Dt}}. \tag{13}$$

Where erfc is the complementary error function and C_0 is the maximum OCA concentration that is reached in sample at saturation conditions.

$$C(z,t) = C_0\left(1 - \frac{2}{\sqrt{\pi}}\exp(-x^2)\sum_{k=0}^{\infty}\frac{2^k x^{2k+1}}{(2k+1)!!}\right), \quad (14)$$

Finally, the solution of Eq. 5 for a semi-infinite medium (tissue samples) is [48]:

$$C\ (z,t) = \ C_0\ \mathrm{erfc}\left(\frac{z}{2\sqrt{Dt}}\right), \quad (15)$$

Figure 3.7 A-B shows the concentration change of OCA in tissue derived from Equation (12) plotted as a function of time for various medium layers and depth for different time intervals, respectively.

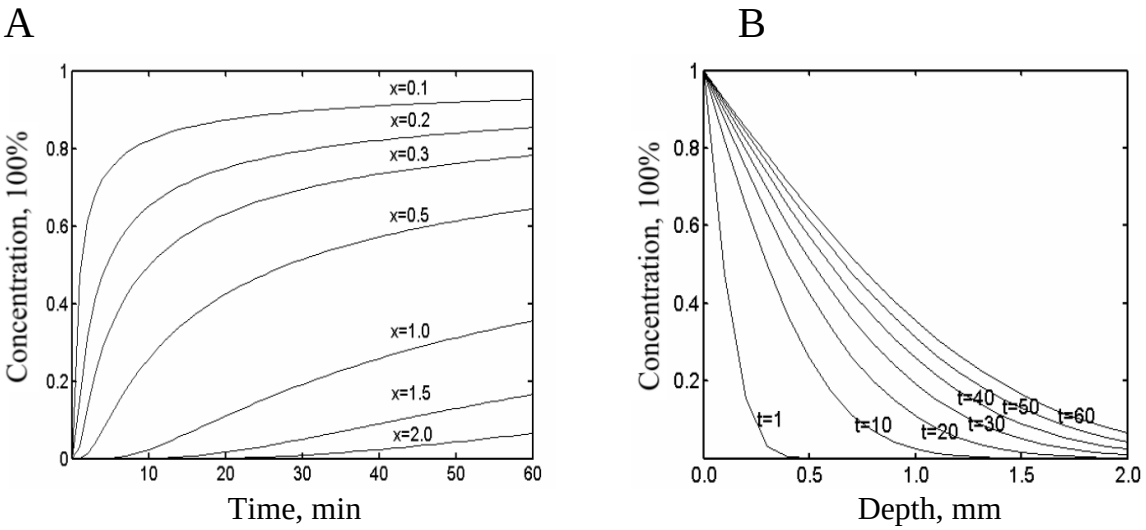

Figure 3.7: *The change of the Gly concentration as (A) function of time from 0 to 60 min, (B) function of depth from 0 to 2 mm in depth [260].*

This theoretical derivation provides a general approach to calculate the diffusion coefficient and concentration of OCA from Raman spectra of the Gly inside the tissue using the passive diffusion model (see Section 4.2). This demonstrates the ability of CRM to quantitatively monitor the OC process.

Chapter 4: Results and discussion

This chapter presents the results obtained during my PhD work, which are divided into three sections. The first section explores the impact of a high concentration of Gly on Raman peak intensity, dehydration, and dissociation of collagen in *dura mater*. The second section examines the effect of 50% Gly (moderate concentration) on the collagen Raman spectrum in *dura mater*, focusing on distinguishing of Gly diffusivity within the framework of passive diffusion and the mobility of water. The third section studies the effect of different OCAs on the Raman spectra of *ex vivo* porcine skin dermis using 633 and 785 nm laser excitations.

4.1 Impact of optical clearing on collagen in *dura mater*

In this section, the impact of a high concentration of 99.0% Gly as an OCA on the DM-collagen Raman spectra is investigated *ex vivo* porcine DM at various depths from 0 to 250 µm using CRM with a 633 nm laser excitation. The Raman measurements were performed in the FP region from 400 to 1800 cm^{-1}. The DM samples were mounted on a motorized *xyz*-stage of the microscope to obtain in-depth z-scan profiles (see Figure 4.1). Before each measurement, any remaining Gly on the DM surface was removed using a paper towel.

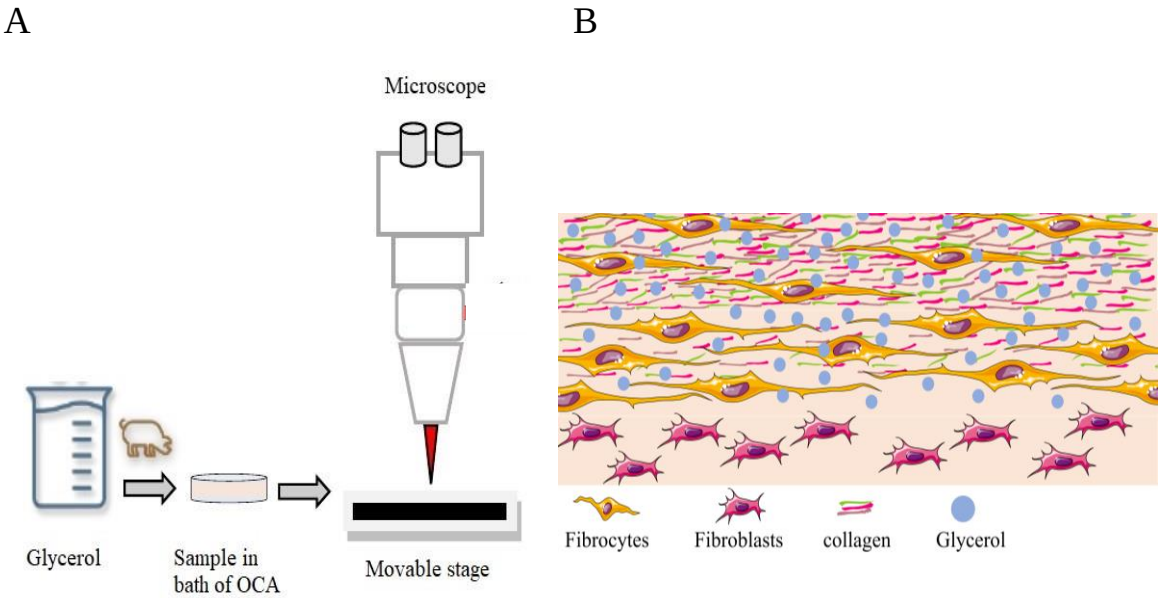

Figure 4.1: *(A) Diagram of the sample preparation, and (B) the schematic representation of the DM model immersed in Gly and Gly molecules distribution. The shapes of the cells of various types were obtained from Servier Medical Art (http://smart.servier.com).*

Figure 4.2 A-B provide a direct comparison of the Raman spectra between control DM (untreated) and Gly in the FP region. The four main collagen-related Raman peaks are located at 938 cm^{-1} (C–C stretching mode of collagen), 1246 cm^{-1} (amide III), 1268 cm^{-1} (amide III), and 1666 cm^{-1} (amide I) [19,21,38]. Gly-related Raman peaks can be observed at 484, 849, 1056, 1250, and 1466 cm^{-1}. It can also be seen that the Raman spectra of the untreated DM sample and Gly overlap partially. Notably, certain regions exhibit minimal interference between the Raman peaks, such as those located at 484, 849, and 1056 cm^{-1}, which can be employed to evaluate the presence of Gly in the DM after OC treatment.

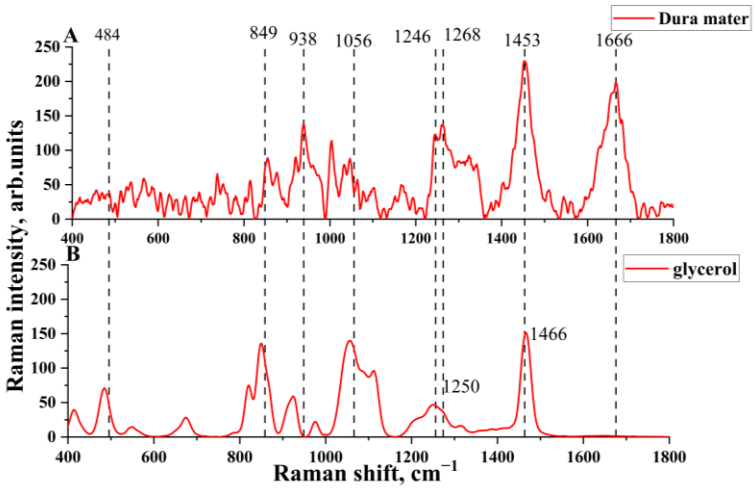

Figure 4.2: *Raman spectra of (A) DM, and (B) 99.0% Gly in the FP region. The dashed lines show the Raman peaks for the DM and Gly.*

Figure 4.3 shows a sequences of Raman spectra recorded from the DM control sample in-depths from 0 to 250 µm (with a step size of 25 µm). These spectra provide a comprehensive overview of the spectral variations with increasing depth.

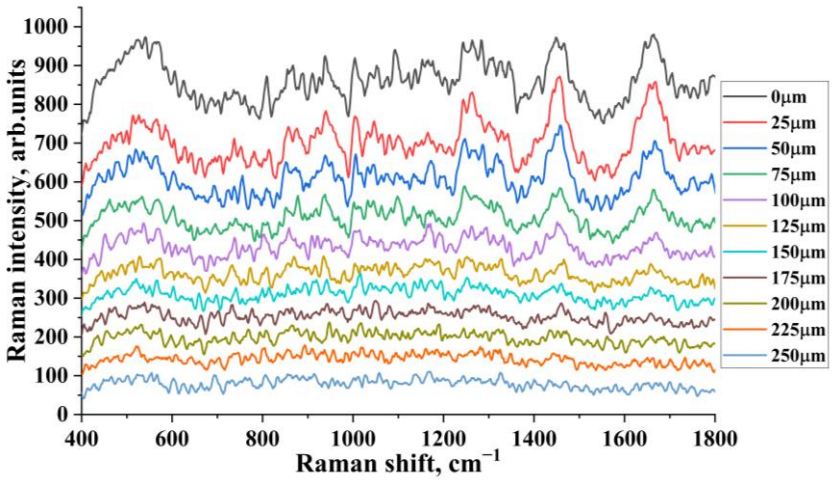

Figure 4.3: *Raman spectra of ex vivo porcine DM control sample from 0 to 250 µm in-depth. The spectra were offsetted along the ordinate for more clarity.*

The DM exhibits substantial optical scattering in the Vis-NIR wavelengths region, attributed to the variance in RI between the scatterers (collagen fibers) and the ISF. This significant scattering in biological objects leads to a notable reduction in the power of the focused excitation light and, consequently, beam divergence. This phenomenon contributes to the weakening of the Raman signal collected by CRM. As illustrated in Figure 4.3, the Raman peak intensities experience a rapid decline with increasing excitation depth caused by the limited penetration of photons into deeper layers of the DM. At depths ranging from 75 to 250 μm, the Raman peaks become indistinct, likely due to the scarcity of probing and detected photons traveling through the tissue as a consequence of its pronounced scattering and absorption properties.

To examine the impact of the OC process on DM after Gly treatment, Raman spectra of both control and treated-DM were recorded at various depths from the sample surface down to 250 μm. The depth-dependent Raman spectra of *ex vivo* porcine DM after Gly treatment times of 5, 10, 15, and 30 min are illustrated in Figure 4.4 A-D. In order to permit straight comparison of the Raman spectra, the Raman spectra related to the DM were first baseline-subtracted and normalized within the frequency intervals from 1590 to 1750 cm^{-1} (amide I band) [99,135,137].

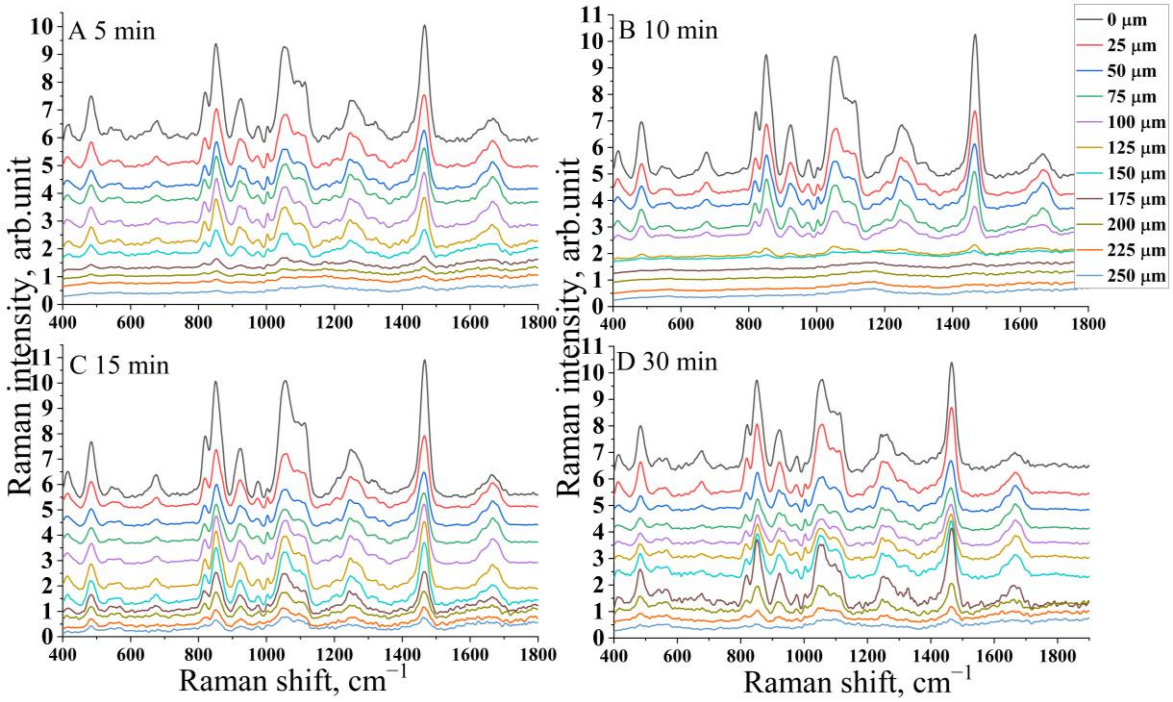

Figure 4.4: *The averaged Raman spectra of DM recorded from depths between 0 and 250 μm treated with glycerol for different times: (A) 5 min, (B) 10 min, (C) 15 min, and (D) 30 min.*

The application of Gly treatment to DM samples enhanced the quality of Raman spectra obtained from deeper regions, thereby enabling a more comprehensive analysis. As it can be seen from Figure 4.4 A-D collagen-related Raman peaks in the treated DM exhibit higher intensities, which is clearly seen in the Raman spectra recorded from deeper regions of the Gly-treated DM. Gly-related Raman peaks at 849 and 1056 cm^{-1} are initially visible only in the outermost superficial layers at the beginning of the treatment. However, these peaks became more visible in deeper layers of DM with prolonged treatment time, suggesting the penetration of Gly into the DM tissue (see Figure 4.5).

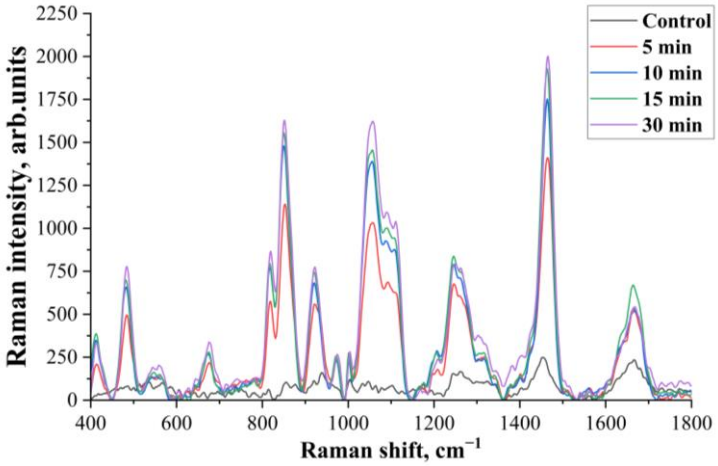

Figure 4.5: *Raman spectra of DM at different treatment time, control (black), 5 min (red), 10 min (blue), 15 min (green) and 30 min (Magenta) at 25 depth.*

To provide a quantitative analysis of the evolution of the impact of OC process at various depths over time, it is important to compare the Raman peak intensities recorded at particular depth before and after different treatment times. The results are summarized in Figure 4.6 demonstrating the impact of different treatment times on collagen-related Raman peak intensities located at 938, 1246, 1268, and 1666 cm^{-1}.

Figure 4.6 confirms that the intensities of Raman peak increase after treatment, attributed to the matching of the RI and the dehydration caused by Gly [177]. This reduction in light scattering and more compact arrangement of collagen fibers leads to improved light penetration and improved Raman spectra from deeper layers of the DM. Moreover, the application of OCA increases the photon penetration depth of the focused beam through the DM [233,261], resulting in the enhancement of Raman signals from deeper regions.

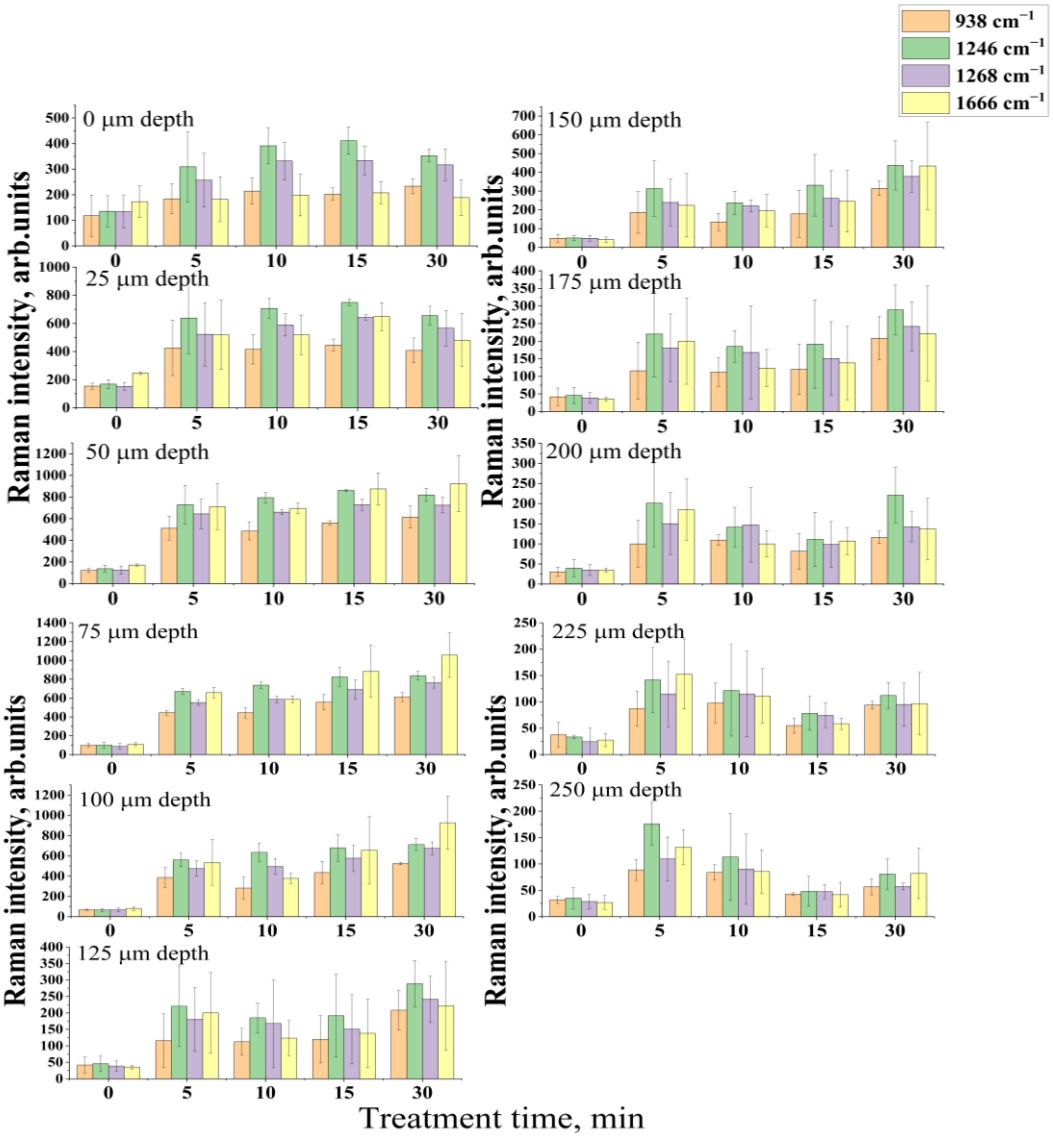

Figure 4.6: *The evolution of the intensities of DM-related Raman peaks located at 938, 1246, 1268, and 1666 cm^{-1} in the depth range from 0 to 250 µm after Gly-treatment for different exposure times.*

At depths from 0 to 50 µm, the collagen-related Raman peak intensities exhibit a monotonic increase after treatment, reaching saturation at 15 min. After this point, the Raman intensities begin to decline. For depths ranging from 75 to 125 µm, the Raman intensities show a gradual growth with respect to treatment time, reaching a highest at 30 min. This is probable attributed to the dehydration impact caused by the osmotic properties of Gly (see Figure 4.8) [38,135].

For depths between 150 and 200 µm, collagen-DM Raman intensities exhibit a reduction after OC treatment. Similar behavior of decreasing Raman intensities can be observed at depths of 225 and 250 µm after treatment of 5 to 15 min. This behavior is likely attributed to tissue rehydration due to water accumulation that comes from deeper layers (in

the absence of Gly) [262]. Additionally, for these treatment times, a lesser amount of Gly penetrates the probing depths. It is visible that at depths ranging from 150 to 250 µm, the Raman intensities begin to rise again after treatment for 30 min, suggesting that Gly molecules have reached the deeper layers of DM tissue.

Figure 4.7 illustrates the same above results in Figure 4.6, demonstrating the increase of collagen-related Raman peaks at 938, 1246, 1268, and 1666 cm^{-1} as a function of depth. It is clearly seen that all Raman peaks exhibit an increase after all treatment time with Gly. However, the enhancement of Raman peaks after OC treatment is more pronounced at first depth and gradually decrease with increasing probing depths.

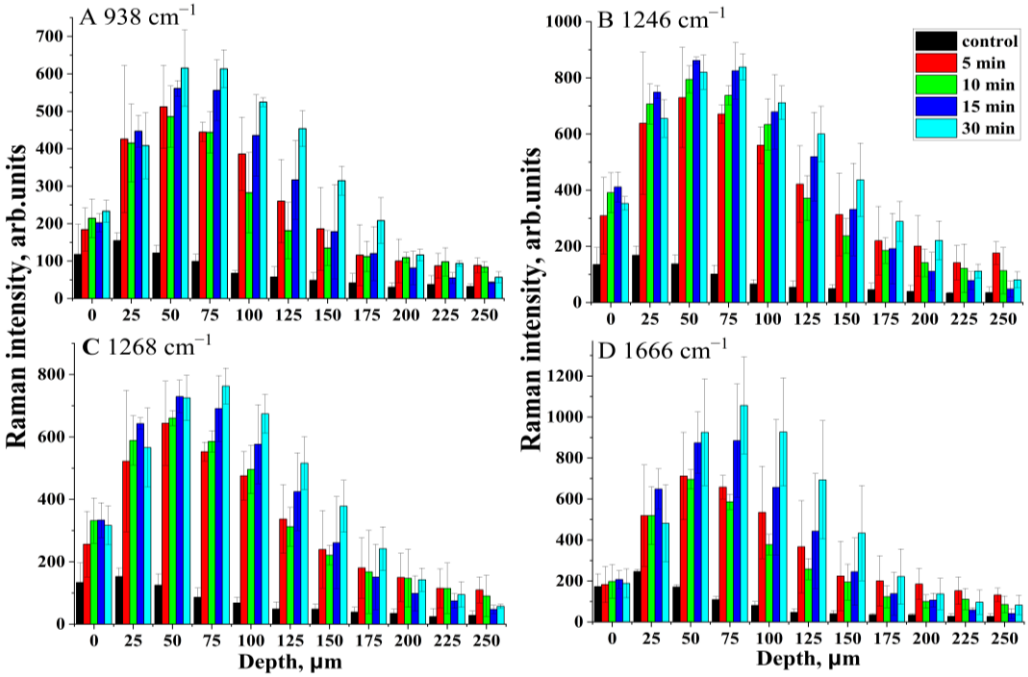

Figure 4.7: *The enhancement of collagen related Raman peaks at (A) 938, (B) 1246, (C) 1268, and (D) 1666 cm^{-1} as function of depths after different treatment time.*

Raman peak located at 938 cm^{-1} (stretching vibrations of skeletal C–C bond) and 922 cm^{-1} (stretching vibration of C–C bond) are observed in collagen chains. The ratio of intensities of the Raman peak at (I_{938}/I_{922}) shows a tendency to increase with increasing hydration of collagen. Therefore, it can be identified as a potential spectroscopic marker of collagen hydration [22,89]. Figure 4.8 illustrates the hydration rate of DM-collagen (modifications in collagen-bound water) evaluated at various depths ranging from 0 to 225 µm.

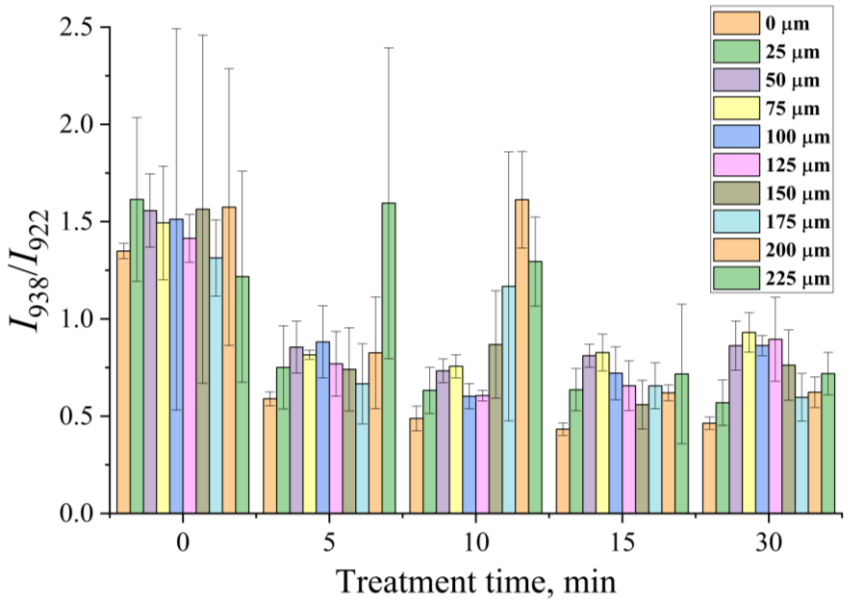

Figure 4.8: *The intensity ratio of the 938 and 922 cm^{-1} Raman peaks (I_{938}/I_{922}) as a function of exposure time for DM-collagen at different depths from 0 to 225 μm.*

As can be seen from Figure 4.8 the Raman intensity ratio (I_{938}/I_{922}) is dramatically reduced during the initial 10 min of Gly treatment for all depths. This observation can be attributed to the high dehydration effect caused by Gly, leading to reduced collagen hydration. Furthermore, the Raman intensity ratio displayed a slightly increase from 75 to 125 μm depths after 10 min treatment. This may be connected to collagen rehydration due to water replacement in the outmost layers with water accumulated from deeper layers of DM tissue at depth ranging from 150 to 200 μm [262]. Moreover, the Raman intensity ratio diminishes after treatment with 5 min, subsequently increases for 10 min, and declines again after treatment with 15 and 30 min. For a longer period of treatment, the Gly molecules diffuses into the DM layers, causing overall rehydration, which can be explained by the restoration of the DM thickness (see Table 4.1 and Figure 4.11). This indicates that there are two processes involved in the OC effect: first, fast shrinkage of collagen (tissue dehydration) and the second the swelling as Gly diffuses into the collagen interfibrillar space. It is worth to notice that each Gly molecule can accumulate approx. six water molecules in the tissue [263,264].

The observed variation in the Raman intensities ratio (I_{938}/I_{922}) across different treatment times reflects the dynamic processes occurring within the DM tissue in response to Gly treatment. The initial decline in the ratio points to a rapid dehydration effect, followed by a subsequent increase, hinting a partial rehydration process. The subsequent decrease in the ratio at longer treatment times could be associated with the ongoing penetration of Gly into deeper layers, affecting the overall hydration status of the DM. These results highlight the

complex interplay between glycerol diffusion, tissue hydration, and collagen dynamics during the OC process.

The detailed analysis of the Raman peaks in the wavenumber region from 1600 to 1750 cm^{-1} provides insights into specific molecular vibrations and structural alterations in the DM tissue. The identified four main Raman peaks located at 1616 cm^{-1} (corresponding to *v*(C═C) in phenylalanine and tyrosine), 1645 cm^{-1} (corresponding to amide I, α-helix and β-sheet), 1666 cm^{-1} (corresponding to amide I, α-helical conformation), and 1681cm^{-1} (corresponding to amide I, disordered structure, non-hydrogen bonds, and C═O stretching) are associated with distinct molecular components and structural features. The Raman peak located at 1666 cm^{-1} in particular, is regarded as a sensor mode of structural modifications of the amide group [265]. This suggestion is based on the fact that the stretching vibration in the amide I C═O is weakly bonded to the stretching vibration of the C–N bond and to the in-plane deformation mode of the N–H amide bond. Therefore, a shift toward lower wavenumbers of the Raman peaks at 1645 and 1666 cm^{-1} can be interpreted as a sign of the existence of heavier structures in collagen, specifically in α-helix and β-sheet [21]. Monitoring alterations in these peaks can provide valuable information about conformational changes and structural proteins within the DM tissue.

Deconvolution of Raman spectra using Gaussian-Lorentzian functions in the 1590–1720 cm^{-1} wavenumber region is a widely technique to analyze complex spectral features and identify individual peaks (see Figure 4.9). By adjusting the full widths at half maximum values of the four Gaussian-Lorentzian peaks within a specified range of 20 cm^{-1}, the deconvolution process aims to separate overlapping peaks and determine their positions more precisely. This approach facilitates the extraction of detailed information about the vibrational modes associated with specific molecular structures. In this context, the calculated spectral shift and changes in peak positions can provide valuable insights into the alterations in molecular conformations and compositions induced by the OC process. These analyses contribute to a better understanding of the structural modifications occurring in collagen fibers during OC treatments.

The combination of CRM and Raman spectra deconvolution offers a powerful tool for to investigating structural alterations in DM-collagen at different depths and treatment times (see Figure 4.10), revealing detailed information about the morphological modifications and the physical importance of the Raman peaks.

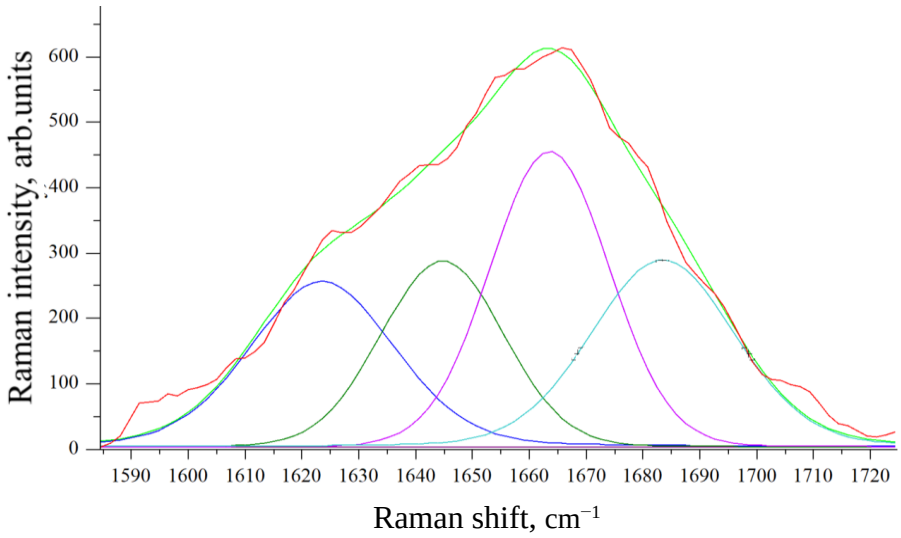

***Figure** 4.9: Gaussian–Lorentzian deconvolution of the four Raman peaks centred at 1616 ± 5 cm^{-1}, 1645 ± 5 cm^{-1}, 1666 ± 5 cm^{-1}, and 1681 ± 5 cm^{-1} for amide I of control DM at the depth of 25 μm.*

In Figure 4.10, the observed upshift in the wavenumber of the Raman peak located at 1666 cm^{-1} indicates modifications in the molecular geometry of amide I, which is attributed to collagen degradation. This suggesting the dissociation of triple helix chains into simpler structures such as single or double strings [21].

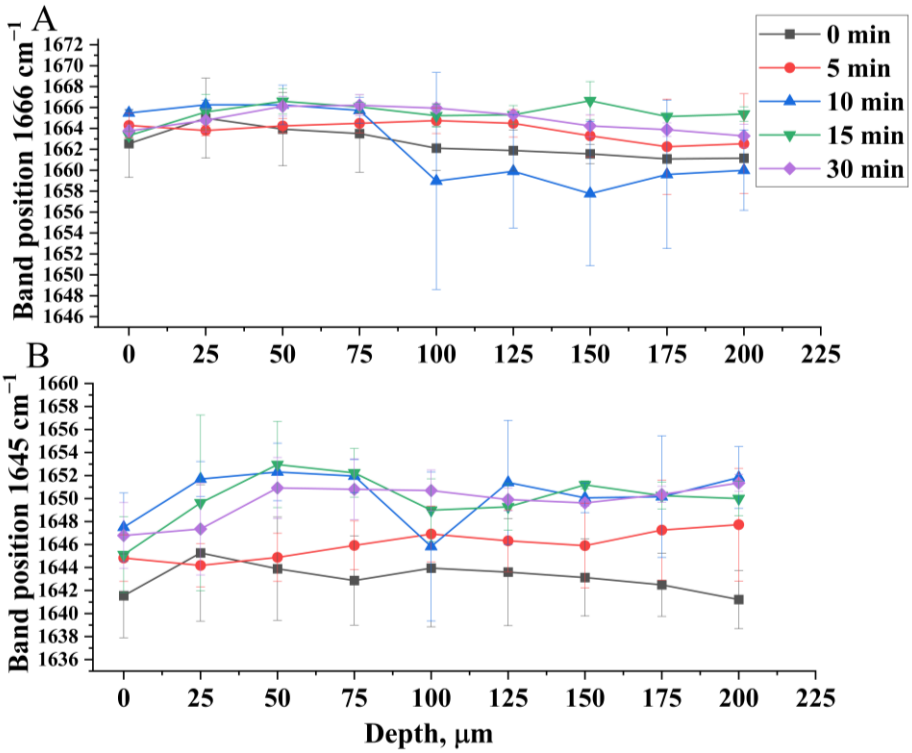

***Figure 4.10:** The position of the (A) 1666 cm^{-1} and (B) 1645 cm^{-1} Raman peaks as a function of depth for various exposure times.*

The dissociation of collagen is one of the OC mechanisms, along with RI matching and dehydration. These results contribute to a deeper understanding of the structural changes induced by Gly treatment in DM-collagen, shedding light on the impact of OC processes on the molecular organization of biological tissues. On the other hand, the observed wavenumber downshifts after 10 min of treatment at depths starting from 75 μm present an intriguing aspect of the OC process [22,89], suggesting that water accumulates from deeper layers, influences the molecular structure of collagen. This information contributes to our understanding of the interplay between dehydration, rehydration, and structural changes in collagen during the OC process. The Raman peak located at 1645 cm^{-1}, which corresponds to the amide I (α-helix and β-sheet) is very difficult to explain [266,267].

The precise measurement of the biological object's thickness during the OC method is one of the important factors in evaluating the OC effect. In this study, DM thickness was measured before and after treatment with Gly (see Table 4.1). The thickness measurements revealed possible limited modifications in the DM geometric parameters under Gly treatment. This result permits the use of non-invasive biophotonics methods like confocal microscopy or OCT to observe the thickness of DM. Nevertheless, it is important to consider the RI changes of the DM during OC treatment [32]. Table 4.1 summarizes the thickness values of DM sample treated with 99.0% Gly for different times. The results demonstrate minimal modifications in the DM thickness. The observed variations in DM thickness (shrinkage/swelling) may be attributed to individual variability among animals.

Table 4.1: *DM thickness (in mm) before and after Gly application for 5, 10, 15, 20, 25, and 30 min at different exposure times.*

Sample	**S1**	**S2**	**Ave**	**STD**
Before	0.54±0.08	0.49±0.08	0.51	0.03
5 min	0.46±0.08	0.33±0.09	0.39	0.09
Sample	**S1**	**S2**	**Ave**	**STD**
Before	0.37±0.09	0.54±0.09	0.46	0.12
10 min	0.37±0.07	0.38±0.04	0.38	0.05
Sample	**S1**	**S2**	**Ave**	**STD**
Before	0.66±0.05	0.61±0.05	0.63	0.04
15 min	0.50±0.06	0.35±0.03	0.42	0.10
Sample	**S1**	**S2**	**Ave**	**STD**
Before	0.54±0.08	0.55±0.04	0.54	0.01
20 min	0.38±0.06	0.33±0.03	0.35	0.03
Sample	**S1**	**S2**	**Ave**	**STD**
Before	0.360±0.12	0.48±0.06	0.42	0.08
25 min	0.42±0.09	0.44±0.08	0.43	0.01
Sample	**S1**	**S2**	**Ave**	**STD**
Before	0.44±0.03	0.52±0.05	0.48	0.05
30 min	0.51±0.10	0.43±0.05	0.47	0.05

Note: Two DM samples were used for each exposure time. The thickness of DM was measured in five different located points on each of them. DM samples were sandwiched between two microscope slides, and thickness measured using a digital micrometer before and after treatment.

Despite the variability in the results shown in Table 4.10, the averaged thickness values determined for all DM-treated for 5-20 min indicate shrinkage of DM due to the dehydration process. Subsequently, a rehydration process occurres, and the DM thickness returns to its original value after treatment with 30 min. DM tissue swelling is noted for the long treatment time, as illustrated in Figure 4.11.

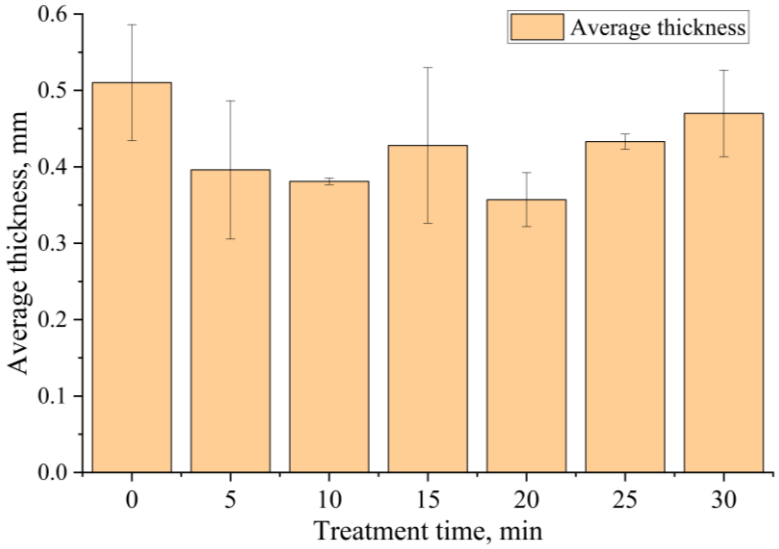

Figure 4.11: *Average thickness of DM as a function of OCA exposure time.*

The obtained results for DM thickness are in good agreement with the Raman spectra and corroborate the three-steps mechanism of the OC process. It is worth to note to avoid strong swelling of *ex vivo* collagenous tissue under OCAs application, the exposure time must be no more than one hour [268].

In conclusion of this part, it was found that the OC effect increases the scanning and the observation depth down to 250 μm of *ex vivo* DM treated with Gly. The Gly, as an OCA significantly increases the collagen-related Raman peak intensities for all investigated depths. In addition, CRM was effectively employed to determine the main processes of OC related to DM-collagen. The results indicate that the OC process can be divided into three stages:

1. Tissue dehydration (a rapid process, collagen shrinkage),
2. Tissue swelling (a relatively slow process) associated with the diffusion of Gly molecules into the collagen interfibrillar space,
3. Collagen dissociation due to high Gly concentration.

4.2 Characterizing glycerol diffusivity and its effect on hydrogen bands

This section focused on investigating the effect of 50% Gly treatment on the Raman spectra of DM-collagen, characterizing Gly diffusivity within the framework of a passive diffusion model in the FP region. In addition, to determine water migration in HWN region using real-time CRM measurement with a 633 nm laser excitation. Time-series Raman spectra were acquired during the OC process by focusing the laser beam at particular depths (50, 100, 150, and 200 μm) below the DM surface. After dropping of 40 μL of 50% Gly onto the investigated area using a micropipette, Raman spectra were recorded in every 30 s (see Figure 3.4).

4.2.1 Diffusion coefficient and concentration of optical clearing agent and its effect on Raman peak intensities

The significant impact of OC on the optical properties of biological tissue and the efficiency of Raman excitation has to be compensated in order to determine the concentration of Gly in biological tissue during the OC process. As a result, there is remarkable crosstalk in the Raman signal. The Raman signal is enhanced because of Gly molecules diffusion and the effect of OC of the upper DM layers. Therefore, we use the following correction method to compensate the influence of OC and determine the relative of Gly concentration (TRGC) from the kinetics of non-movable proteins peak in DM tissue, independent of the OC efficiency (OC_{eff}).

First, we calculated the OC_{eff} from the increase in collagen-related Raman peak intensity, expressed as the intensity of Raman peak after treatment (I_{OC}) to the intensity of Raman peak before treatment (I_0) ratio at a given depth and time [38,229,269].

$$OC_{eff} = \frac{I_{oc}}{I_0} \tag{16}$$

Then, we calculated the ratio of the intensity of Gly-related Raman peak (I_{gly}) located at 485 cm^{-1} already acquired during measurement to OC_{eff} of various collagen-related Raman peaks to get the change arising solely from TRGC:

$$\mathrm{TRGC} = \frac{I_{\mathrm{gly}}}{\mathrm{OC_{eff}}} \tag{17}$$

In the beginning, Raman spectra of the DM control sample at 50 μm depth, 50% Gly solution, and a series of different Gly concentrations 0–50% in DW were recorded in the FP region (see Figure 4.12A, B and C, respectively). Figure 4.12A illustrates the prominent

collagen-related Raman peaks located at 938 cm^{-1}, 1246 cm^{-1}, 1270 cm^{-1}, and 1666 cm^{-1} [19,21,38], the Raman peaks of 50% Gly are located at 485, 849, 1054, and 1466 cm^{-1} according to study results (see Figure 4.12B) [38], and Raman spectra of DM before and after treatment were measured at depths of 50 and 200 μm (see Figure 4.12D). However, Gly- and DM-related Raman peaks exhibit overlapping in the spectra (see Figure 4.12D). Thereby, the less overlapped Gly-related Raman peak at 485 cm^{-1} was selected to determine the Gly concentration in the treated DM.

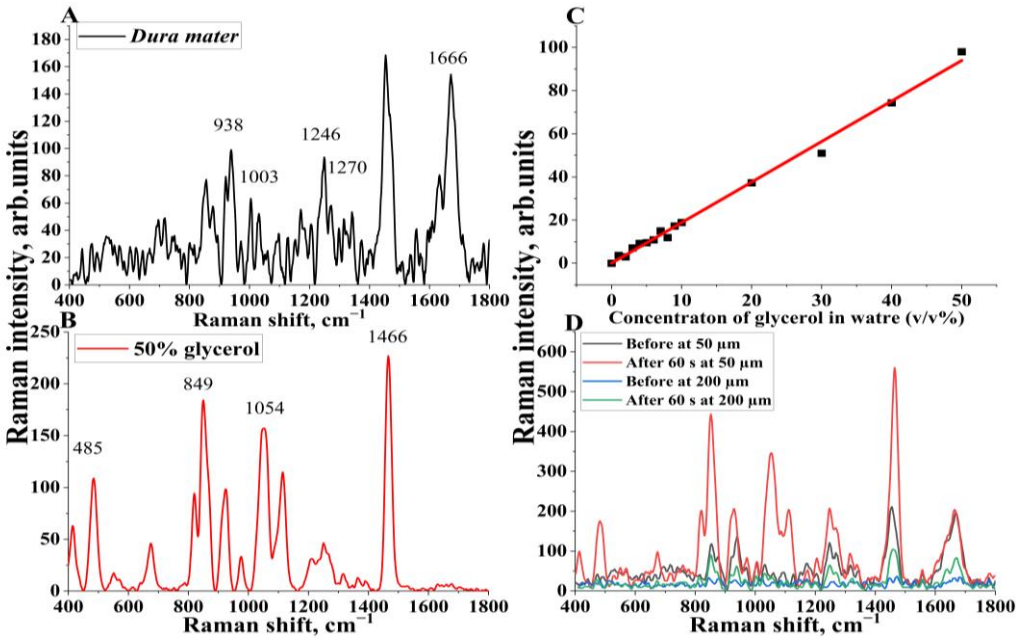

Figure 4.12: *Raman spectra of (A) untreated DM at depth 50 μm, (B) 50% Gly solution and (C) Calibration curve of the 485 cm^{-1} Raman peak intensity for glycerol solutions of different (0–50%) concentrations in water. The red line is a result of fitting with correlation coefficient (R^2) of 0.9941. (D) Raman spectrum before and after 60 sec treatments at depths of 50 and 200 μm.*

Figure 4.12C illustrates a linear relationship between the intensity of Gly-realted Raman peak at 485 cm^{-1} and the concentration of Gly in DW. This calibration curve can be employed to determine the TRGC in Gly-treated DM tissue.

Following the method described by Liu *et al*. [48], a custom nonlinear curve fitting algorithm and the calibration curve of Gly were used to obtain the fitting parameters from Figures 4.13–17, which reported in Table 4.2. The D and C_0 values were calculate using the change in TRGC corresponding to various depths and treatment times, employing the framework of the passive diffusion model (as described in Section 3.5) for collagen-related Raman peaks at 938, 1003, 1247, 1271, and 1665 cm^{-1} during the OC process. Due to the fibrous structures of tissues like the dermis, scaler, and muscle, it is entirely reasonable to

assume that fluid dynamics diffusion within these biological tissues is well explained by free diffusion. As shown in Section 3.5 the solution can be written in the next form (Equation 15):

$$C_{\mathrm{OCA}}(z,t) = C_0 \operatorname{erfc}\left(\frac{z}{2\sqrt{Dt}}\right)$$

where erfc is the complementary error function, C_0 is the maximum concentration of Gly at saturation conditions D is the diffusion coefficient corresponding to the Gly molecular mass transport into the DM tissue.

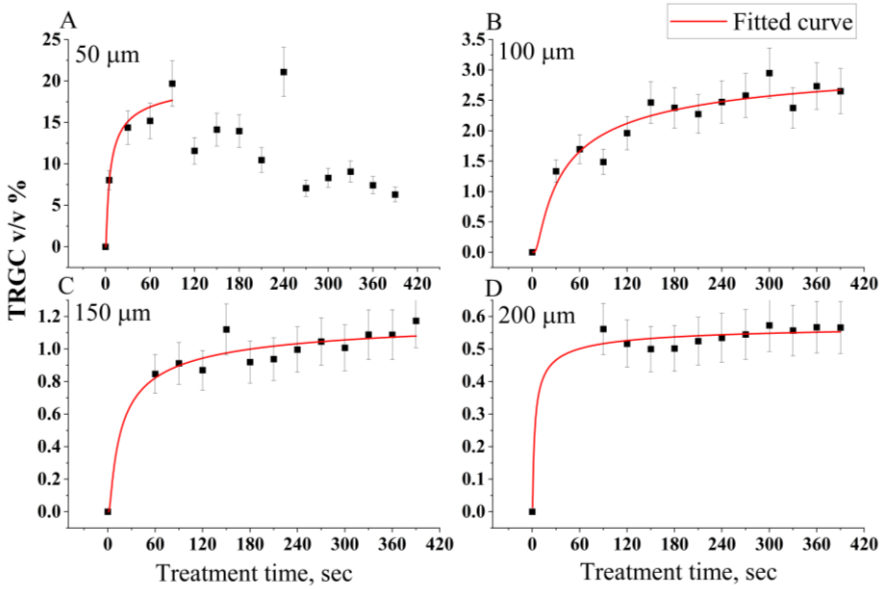

Figure 4.13: *The TRGC change at various depths of (A) 50 µm, (B) 100 µm, (C) 150 µm, and (D) 200 µm for ex vivo DM-related Raman peak at 938 cm^{-1} as a function of treatment time treated by 50% Gly.*

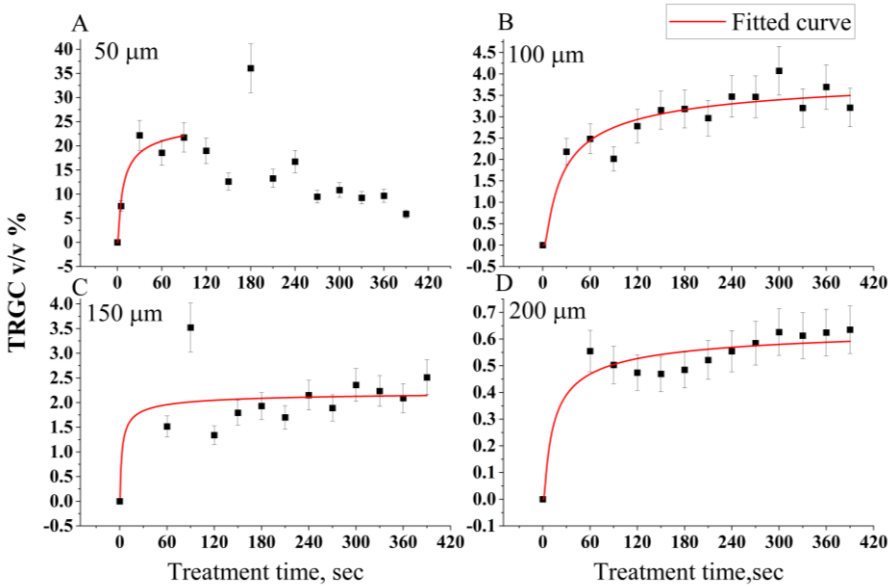

Figure 4.14: *The TRGC change at various depths of 50 µm (A), 100 µm (B), 150 µm (C), and 200 µm (D), for ex vivo DM-related Raman peak at 1003 cm^{-1} as a function of treatment time treated by 50% Gly.*

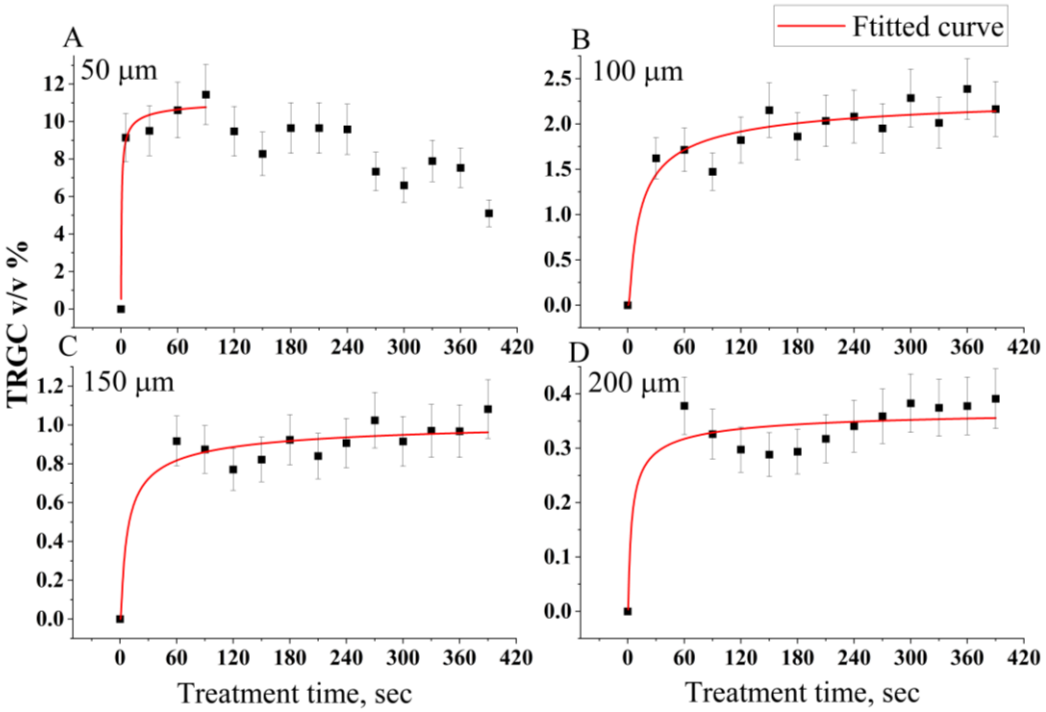

Figure 4.15: *The TRGC change at various depths of 50 µm (A), 100 µm (B), 150 µm (C), and 200 µm (D), for ex vivo DM-related Raman peak at 1247 cm^{-1} as a function of treatment time treated by 50% Gly.*

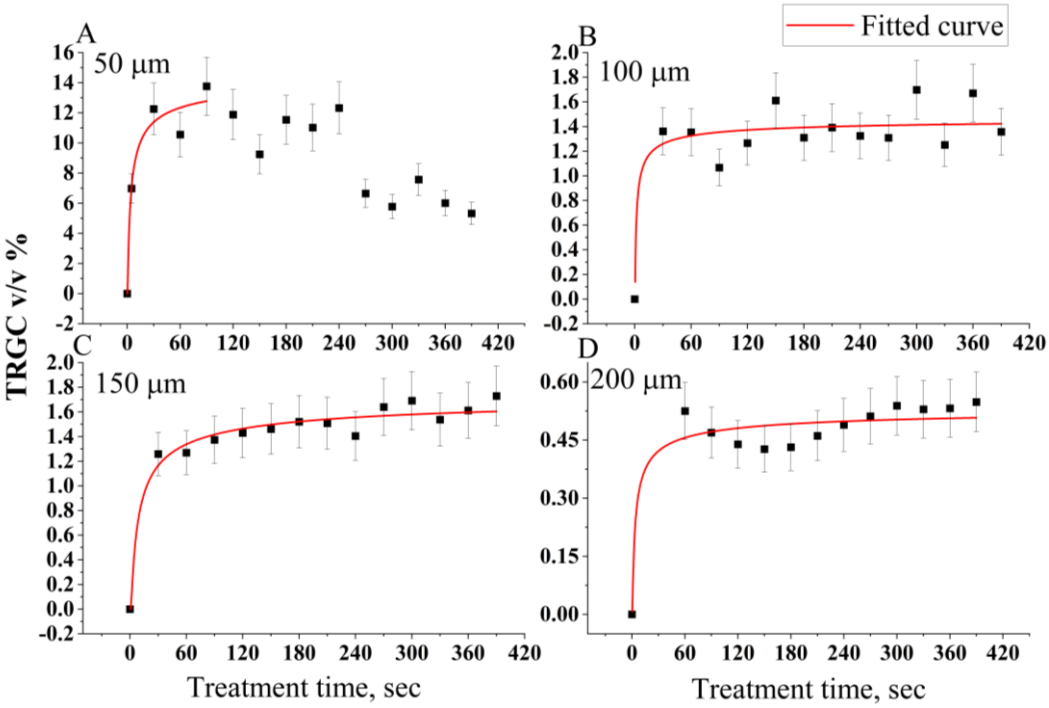

Figure 4.16: *The TRGC change at various depths of 50 µm (A), 100 µm (B), 150 µm (C), and 200 µm (D), for ex vivo DM-related Raman peak at 1271 cm^{-1} as a function of treatment time treated by 50% Gly.*

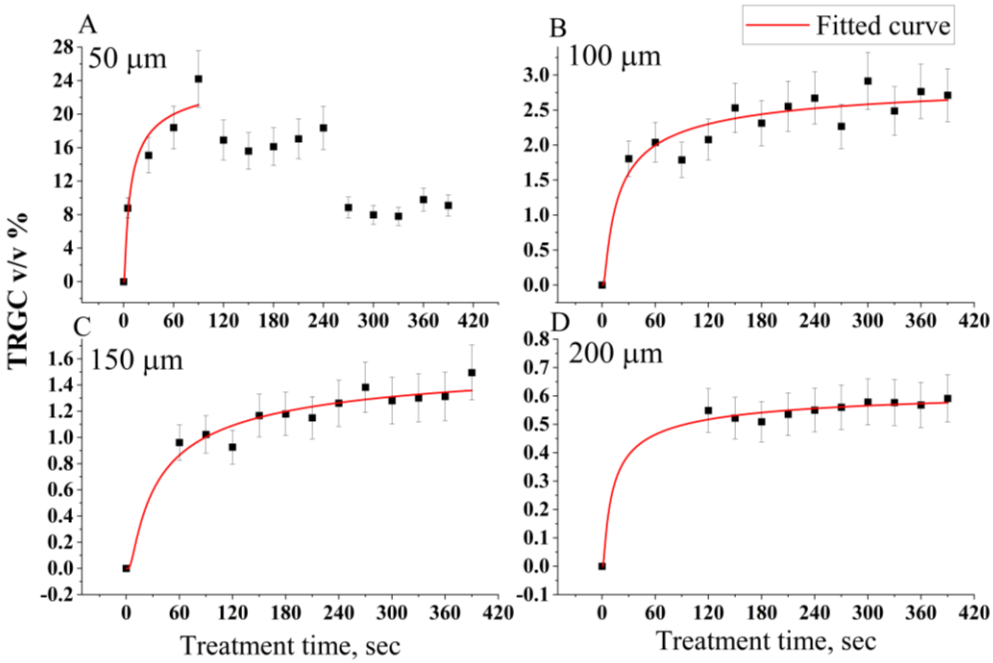

Figure 4.17: *The TRGC change at various depths of 50 µm (A), 100 µm (B), 150 µm (C), and 200 µm (D), for ex vivo DM-related Raman peak at 1666 cm^{-1} as a function of treatment time treated by 50% Gly.*

For instance, by use equation 15 for calculated the diffusion coefficient and concentration. If we stay at depth of 0 µm, i.e., x = 0 µm, then at t = 0, $C(t=0)$= 0 and $C(t=\infty)$ = $C0$. A complex dependence with saturation and decrease over a short distance may be associated with some artifacts or complex behavior at the liquid-tissue interface. Figure 4.18 illustrates an example to calculate the diffusion coefficient and concentration using custom nonlinear curve fitting at depth 150 µm.

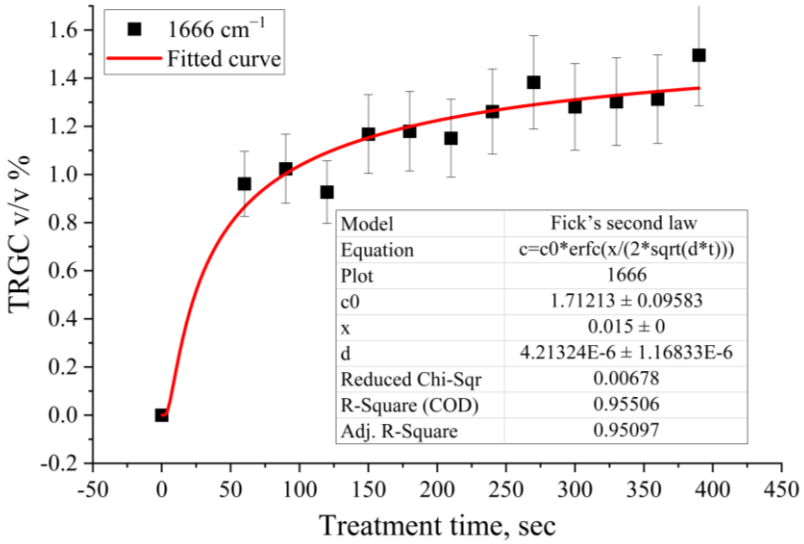

Figure 4.18: *The TRGC change at various depths of 150 µm for ex vivo DM-related Raman peak at 1666 cm^{-1} as a function of treatment time treated by 50% Gly.*

Table 4.2: *Results of the fitting data of the Figures 4.13-17 for DM-collagen at various depth and exposure times employing the passive diffusion model.*

Depth, μm (938 cm^{-1})	**Time, sec**	C_0 **v/v**	D**, cm^2/sec**	R^2
50	90	21	3.0×10^{-6}	0.96
100	390	3.4	1.7×10^{-6}	0.92
150	390 starts with 60	1.2	9.4×10^{-6}	0.94
200	390 starts with 90	0.5	9.8×10^{-5}	0.97
Depth, μm (1003 cm^{-1})	**Time, sec**	C_0 **v/v**	D**, cm^2/sec**	R^2
50	90	27	2.5×10^{-6}	0.94
100	390	4.2	2.7×10^{-6}	0.88
150	390 starts from 60	2.3	6.5×10^{-5}	0.53
200	390 starts from 90	0.8	6.2×10^{-6}	0.96
Depth, μm (1247 cm^{-1})	**Time, sec**	C_0 **v/v**	D**, cm^2/sec**	R^2
50	90	11	3.5×10^{-5}	0.98
100	390	2.4	5.9×10^{-6}	0.91
150	390 starts from 60	1.1	2.2×10^{-5}	0.92
200	390 starts from 90	0.5	8.1×10^{-6}	0.94
Depth, μm (1270 cm^{-1})	**Time, sec**	C_0 **v/v**	D**, cm^2/sec**	R^2
50	90	15	5.0×10^{-6}	0.95
100	390	1.5	4.6×10^{-5}	0.83
150	390 starts from 60	1.9	9.6×10^{-6}	0.97
200	390 starts from 90	0.6	1.1×10^{-5}	0.96
Depth, μm (1666 cm^{-1})	**Time, sec**	C_0 **v/v**	D**, cm^2/sec**	R^2
50	90	26	2.3×10^{-6}	0.94
100	390	3.1	4.3×10^{-6}	0.91
150	390 starts from 60	1.7	4.2×10^{-6}	0.95
200	390 starts from 120	0.6	2.5×10^{-5}	0.99

We calculated the change in the diffusion coefficient (D) of TRGC (I_{gly}/OC_{eff}) for collagen-related Raman peaks at 938, 1003, 1247, 1271, and 1666 cm^{-1} during the OC process at varying treatment times. These results are shown in Figures 4.13–17 at different depths of 50, 100, 150, and 200 μm under the DM sample's surface, respectively. As can clearly be seen from Figures 4.13–17, the diffusion curves exhibit a smoother profile with rising probing depth and have a tendency to a mono-exponential shape at 100 to 150 μm depths, which is consistent with published experimental and theoretical model [48,260].

On the other hand, at a depth of 200 μm, at least two exponents are observed, indicating two competing mechanisms. The main difference between these results and the theoretical model lies in the simultaneous occurrence of two fluxes in the DM tissue—water is going out (fast), and Gly going in (slow), leading to two processes for improved Gly-related Raman peak intensity: first, the increase in Gly molecule concentration at a specific depth over time (see Figure 4.19 C), and second, the reduction of light scattering from the upper DM layers due to OC's impact. However, the water migration involved in the fast OC process causes dehydration.

Table 4.3 reveals that the *D* values are different at various depths and displays ascending and descending patterns with treatment time. This variation can be attributed to the combined effects of DM component dehydration and/or the collagen structural modification [270]. The average variation of *D* ranges from 9.6×10^{-6} to 3.0×10^{-5} cm^2/s depending on the concentration of Gly and depth.

Table 4.3: *Glycerol diffusion coefficients and concentrations obtained from fitting of the TRGC data.*

	Depth 50 µm		**Depth 150 µm**	
Raman peak, cm^{-1}	***D*, cm^2/sec**	**C_0, v/v**	***D*, cm^2/sec**	**C_0, v/v**
938	2.3×10^{-6}	21	9.4×10^{-6}	1.2
1003	2.5×10^{-6}	27	6.5×10^{-5}	2.3
1247	3.5×10^{-5}	11	2.2×10^{-5}	1.1
1270	5.0×10^{-6}	15	9.6×10^{-6}	1.9
1665	2.3×10^{-6}	26	4.2×10^{-6}	1.7
Average	**9.6×10^{-6}**	**20**	**2.2×10^{-5}**	**1.6**
	Depth 100 µm		**Depth 200 µm**	
Raman peak, cm^{-1}	***D*, cm^2/sec**	**C_0, v/v**	***D*, cm^2/sec**	**C_0, v/v**
938	1.7×10^{-6}	3.4	9.8×10^{-5}	0.6
1003	2.7×10^{-6}	4.2	6.2×10^{-6}	0.8
1247	5.9×10^{-6}	2.4	8.1×10^{-6}	0.5
1270	4.6×10^{-5}	1.5	1.1×10^{-5}	0.6
1665	4.3×10^{-6}	3.1	2.5×10^{-5}	0.6
Average	**1.2×10^{-5}**	**2.9**	**3×10^{-5}**	**0.6**

The variation in *D* values across different DM depths is associated to the heterogeneous composition and structural organization of the tissue. DM collagen fibril layers tend to be more disorganized and chaotic from the surface to in-depth [64,67]. In general, the DM predominantly composed of approx. 70% water, 20% collagen, and 10% elastin [271], the diffusion coefficients of mixtures of Gly/water systems serve as acceptable models for study of any biological object, including DM. Studies have demonstrated that Gly diffusion coefficient values in Gly/water mixtures system increase with decreasing Gly concentration [272,273].

We can observe from Table 4.3, C_0 averages range from 0.6 to 20 v/v, which is significantly less than the original 50% Gly concentration. The C_0 average concentration value reduces progressively from high to low with depth and has a maximum value in the upper layer of DM. The reasons may be associated with the Gly dilution because of the dehydration process [178].

As illustrated in Figures 4.13A–17A, the TRGC at 50 µm depth in the uppermost DM drastically rises during the early period of diffusion [48,260], followed by a gradual decrease

with time. However, in deeper DM layers, the TRGC gradually rises with time, except at the 200 μm depth. Here, the TRGC concentration remains very low (see Table 4.3, 200 μm depth); and the efficiency of OC is greater than three times lower than for other depths. On the other hand, the Raman peak intensities increase fastly (within 1–2 min), which is related to the low viscosity and high diffusivity of the small concentrated of Gly in the tissue water [272–275].

Over time, the Raman peak intensities saturate and even steadily reduce due to the following two phenomena. First, interaction of Gly molecule with water molecules leading to the binding of one Gly molecule to approximately six water molecules. This interaction, which is a key contributor to Gly's hydrating effect in cosmetology, promotes tissue softening and hydration [276]. In this case, localized tissue rehydration (swelling) occurs, leading to a returns to a higher scattering state [93]. Second, corresponds to the interaction of Gly molecules with collagen fibrils. This occurs as the next phase after Gly fills up the interstitial space in the protein matrix, causing dehydration of the fibrils. During this process, the RI of the fibrils slightly increases, while that of the surrounding tissue slightly decreases, resulting in some RI mismatching and higher light scattering [277].

To examine the influence of OC, Gly was topically applied on the same DM samples used for Gly diffusion coefficient (*D*) calculations. The intensities of Raman peak were recorded in real-time from 0 to 390 seconds under the DM surface at depths of 50, 100, 150, and 200 μm. Figure 4.19 illustrates the kinetic curves of collagen-related Raman peak intensities after Gly application.

As can be clearly seen from Figure 4.19A, the intensities of Raman peak for the 50 μm depth exhibit sharply increases during the early stage of treatment, reaching a maximum at 5 seconds. Afterward, the intensities drop down due to the interaction of Gly molecules with water migration within the DM tissue for longer treatment times. This observation could be connected to the time-dependent Gly diffusion, influenced by its complex interactions with both bound and unbound water molecules in the tissue [181,278]. Another potential contributing factor is the shortage of Gly molecules at the DM surface, leads to an irregular flux and a decrease in concentration with time. Additionally, the observed decline in Raman peak intensities following the initial rise could be attributed to local tissue swelling, which occurs following the initial tissue shrinkage induced by the high Gly concentration (see Table 4.3 at 50 μm depth). This swelling results in increased scattering, i.e., a decline in the OC efficiency [93].

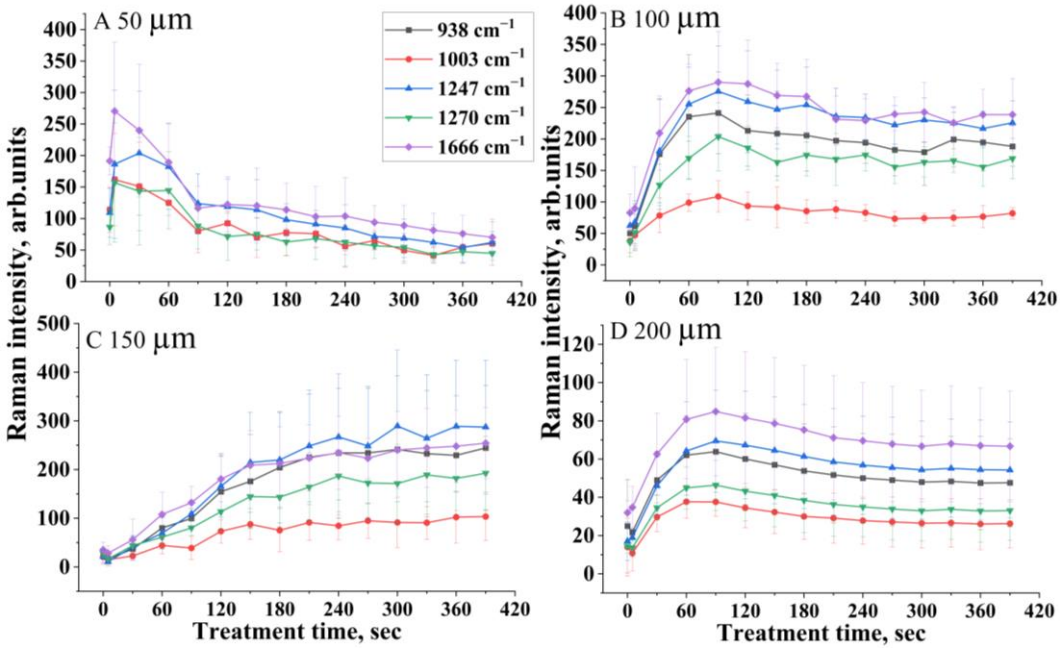

Figure 4.19: *Raman peaks of the main collagen-DM at 938 (black squares), 1003 (red circles), 1247 (blue upward triangles), 1270 (green downward triangles), and 1665 cm^{-1} (purple diamonds) as a function of time from 0 to 390 sec after topically applied of 50% Gly at different depths of (A) 50, (B)100, (C) 150 , and (D) 200 µm.*

At a depth of 100 µm, the intensity of Raman peak improves with time and achieves the highest value at 90 s. Subsequently, the intensity decreases, followed by a saturation between 210 and 390 s (Figure 4.19B). At a depth of 150 µm, the intensities of Raman peak exhibit a monotonic increase with time (see Figure 4.19C), which can be described as the balance between local tissue swelling/shrinkage abilities for a specific concentration of Gly (see Table 4.3, at depth 150 µm) due to the similar level of the opposite water fluxes. Therefore, the relatively slow diffusion of Gly molecules into the tissue results in the matching of RI process of the OC.

At a depth of 200 µm, the intensity of Raman peak increased in the first 1–2 min due to the high diffusivity and low viscosity of the low-concentration Gly in DM tissue. It can be clearly seen from Figure 4.19, the Raman peak intensities continue to increase throughout the OC process, primarily driven by the RI matching and dehydration effects induced by OC [177]. This dehydration leads to a more compact collagen structure and fewer light scattering and enhancing the Raman signal. Additionally, the moderate Gly concentration dose not induce any dissociation of the collagen fibers [141].

4.2.2 The effect of glycerol on various types of water hydrogen bonds

In this part, in-depth water migration is studied according to the hydrogen bonds strength during the topical application of Gly on *ex vivo* porcine DM samples. The deconvolution of Raman spectra, as proposed in [138,140], and further customized by Choe *et al.* [139] for skin analysis, is extended to examine the water migration within DM layers in-depth.

To quantify water content fluxes according to the strength of hydrogen bonds, Raman spectra of *ex vivo* porcine DM in the HWN region were recorded and then deconvoluted utilizing 10 Gaussian functions [139]. The area under the curve (AUC) related to each Gaussian function was determined. Four Gaussian functions centered at 2850, 2880, 2940, and 2980 cm^{-1} (±5 cm^{-1}) were assigned to vibrations of proteins and lipids. Two Gaussian functions positioned at 3060 and 3330 cm^{-1} (±5 cm^{-1}) were assigned to vibrations of the NH to unsaturated methylene.

Additionally, four Gaussian functions located at 3005, 3277, 3458, and 3604 cm^{-1} (±5 cm^{-1}) were related to the mobility states of water: tightly-bound (DAA–OH, single donor–double acceptor), strongly-bound (DDAA–OH, double donor–double acceptor), weakly-bound (DA–OH, single donor–single acceptor), and free water (sum of unbound water (free OH) and very weakly bound (DDA–OH, double donor–single acceptor)), as suggested in the literature [139]. The Gaussian function widths were allowed to vary within 20 cm^{-1} for better-fitting curve quality. The full water content was calculated as the ratio of the sum of the AUCs of the four water peaks to that of the protein Raman peak at 2940 cm^{-1}.

Figure 4.20 illustrates Raman spectra in the HWN region for control *ex vivo* DM control together with deconvolution (Figure 4.20A), 50% Gly (Figure 4.20B), and the impact of OC for 50 and 200 μm depths (Figure 4.20 C, D). It can be observed in Figure 4.20 A and B, the Raman spectra of 50% Gly overlap with the water and protein components in the DM Raman spectra, particularly within the 2910 to 2965 cm^{-1} (CH_2 vibrations of OCA) and from 3100 to 3700 cm^{-1} (CO–H and OH vibrations) regions [279]. In Figure 4.20 C and D, there is a clear enhancement of Raman spectra in the HWN at depth 50 and 200 μm after Gly treatment, primarily attributed to the OC-induced dehydration and reduced light scattering.

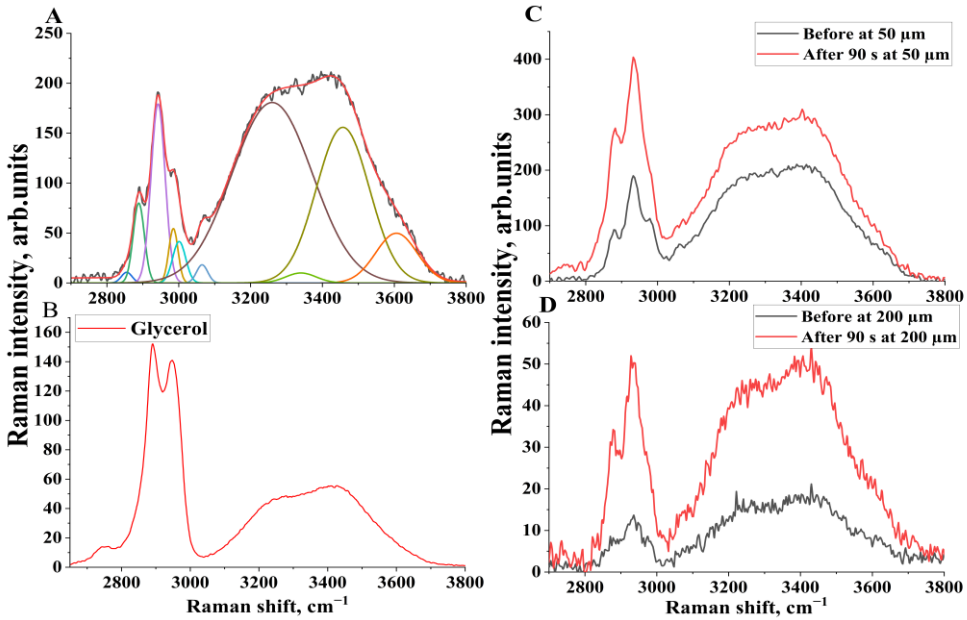

Figure 4.20: *Deconvolution of Raman spectra in the HWN region with Gaussian peaks for (A) control DM at 50 µm depth, (B) 50% glycerol solution and the Raman spectra before and after 90 sec treatment at (C) 50 and (D) 200 µm depths, respectively.*

To examine the impact of 50% Gly treatment, the AUC values were determined for the four water mobility states in the DM tissue after treatment at different depths and over time. Figure 4.21 illustrates the results for the time-dependent kinetics of the four mobility states of water.

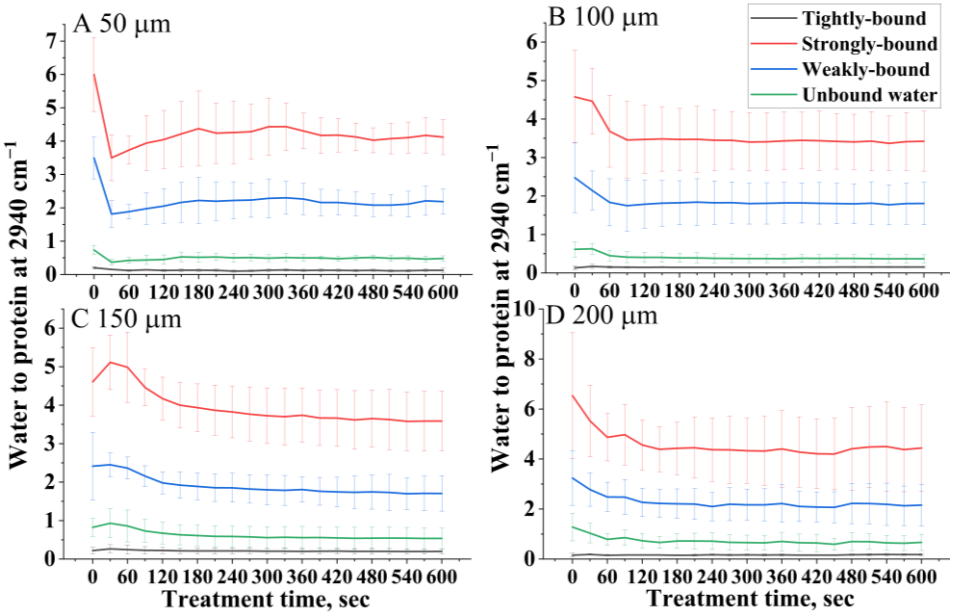

Figure 4.21: *Time-dependent kinetics of tightly-bound (3005 cm^{-1} Raman peak, black), strongly-bound (3270 cm^{-1}, red), weakly-bound (3458 cm^{-1}, blue,), and unbound (3605 cm^{-1}, green) water based on Gaussian deconvolution at depths of (A) 50 µm, (B) 100 µm, (C) 150 µm, and (D) 200 µm.*

As can be observed from Figure 4.21, all four mobility states of water consistently decrease over time after application of 50% Gly, with the exception of tightly-bound water, which exhibits the smallest change across all depths. At a depth of 50 μm, both strongly and weakly bound water molecules experience a significant reduction in the initial stage, followed by a slight increase after 60 seconds (Figure 4.21 A). This phenomenon can be attributed to collagen rehydration, resulting from the replacement of water molecules in the uppermost layers of DM with water accumulated from deeper DM layers [262]. At depths of 100 μm, 150 μm, and 200 μm, strongly and weakly-bound water exhibited a monotonic reduction with time. Additionally, unbound water showed a consistent decrease after treatment across all depths (Figure 4.21 B–D).

Table 4.4 presents water content values for the four water mobility states before and at the end of treatment of 50% Gly (see Figure 4.21). It can be seen that the most prominent water molecule states both before and after the OC treatment at all examined depths are strongly and weakly bound water molecules.

Table 4.4: *DM water content (in v/v) before and after the treatment with 50% glycerol solution.*

Water type	**Depths, μm**							
	50		**100**		**150**		**200**	
	Before	**After**	**Before**	**After**	**Before**	**After**	**Before**	**After**
Tightly-bound	0.20±0.03	0.12±0.06	0.13±0.05	0.15±0.02	0.22±0.08	0.19±0.06	0.18±0.08	0.17±0.04
Strongly-bound	6.00±1.10	4.12±0.52	4.57±1.20	3.42±0.77	4.60±0.88	3.58±0.77	6.53±2.51	4.44±1.72
Weakly-bound	3.49±0.62	2.18±0.37	2.47±0.90	1.80±0.55	2.41±0.87	1.70±0.45	3.24±1.09	2.15±0.83
Unbound water	0.73±0.13	0.48±0.07	0.61±0.19	0.36±0.10	0.82±0.23	0.53±0.27	1.27±0.55	0.66±0.32

However, the values corresponding to these two types substantially decreased after 50% Gly application at all four depths. The results suggest that in DM tissue, these two types of water—strongly and weakly-bound—are preferentially involved in water mobility caused by OCA, making them significant contributors to the OC process. A comparable effect has detected in the skin [135,139].

Figure 4.22 shows the time-dependent behavior of total water content in the DM tissue after 50% Gly treatment. The total water content exhibits a monotonic decrease after treatment at all depths except 50 μm. In this case, a sharply decreases in the initial stage of treatment followed by a subsequent rise over time. This pattern can be attributed to water replacement in the uppermost DM layers with water accumulated from deeper layers [262].

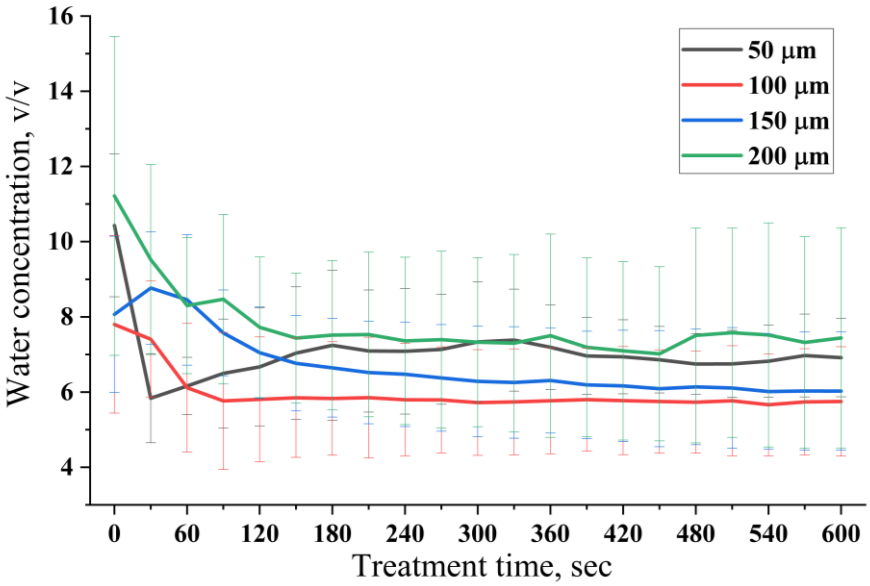

Figure 4.22: *The kinetics of full water content in DM after the application of 50% glycerol at different depths: 50 (black), 100 (red), 150 (blue), and 200 µm (green).*

As it has been shown earlier (see Fig. 4.20), the Raman peaks of 50% Gly overlap with protein-related in the DM, potential leading to underestimation of the AUC ratios [82]. Even though this underestimation is particularly manifest in superficial layers where the concentration of Gly is highest. However, in deeper DM layers, the influence of Gly on DM protein-related Raman spectra is expected to be substantially less. This substantial decrease in underestimation can be attributed to the lower concentrations of Gly in these deeper layers, minimizing its influence. It is important to mention that the osmotic pressure caused by Gly results in the conversion of bound water to free water (unbound) [278,280]. This response is similar to the effect detected during occlusion-induced swelling in the skin [281]. Consequently, Gly has potential to produce local, depth-dependent dehydration in the DM. Moreover, as Gly molecules penetrate the DM tissue, they bind with water molecules, giving rise to water fluxes between DM water and glycerol-bound water.

To conclusion this section, the impact of the OC process on *ex vivo* porcine DM were investigated after topical application of 50% Gly assisted by CRM. The Gly diffusion coefficients in *ex vivo* porcine DM were found to range from 9.6×10^{-6} to 3.0×10^{-5} cm^2/s at different depths. Notably, the highest concentration of Gly (C_0) observed in the DM tissue is about 20%, was significantly smaller than the original applied concentration of 50% Gly. The intensities of collagen-related Raman peak were significantly enhanced for all depths, ranging from 50 to 200 µm, after OCA application, as an outcome of the OC process. Furthermore, 50% Gly application caused significant changes in the total water content of the DM,

suggesting that 50% Gly application causes tissue dehydration occurs during the OC process. Weakly and strongly bound water types were identified as the most prevalent and concentrated water states in the DM. These water states play a crucial role in the OC process by influencing Gly-induced water migrations. The results demonstrate that the OC process is an effective technique for controlling the optical properties of DM.

4.3 The effect of OCA and laser wavelength on *ex vivo* skin collagen

This section aimed to investigate the impact of various OCAs on the Raman spectra of *ex vivo* porcine skin within the FP region (from 630 to 1750 cm^{-1}) using 633 and 785 nm laser excitation at depths ranging from 0 to 240 µm. Additionally, the study explored the influence of DMSO as a potential enhancer. The skin samples were placed on a motorized *xyz*-stage of the microscope to obtain in-depth z-scan profiles. Prior to each measurement, any remaining Gly was removed from the skin surface using a paper towel. Figure 4.23A-B illustrates a sequence of Raman spectra recorded from a control *ex vivo* porcine skin sample at incremental depths, with 40 µm interval (from 0 to 240 µm), using excitation wavelengths of 633 and 785 nm, respectively.

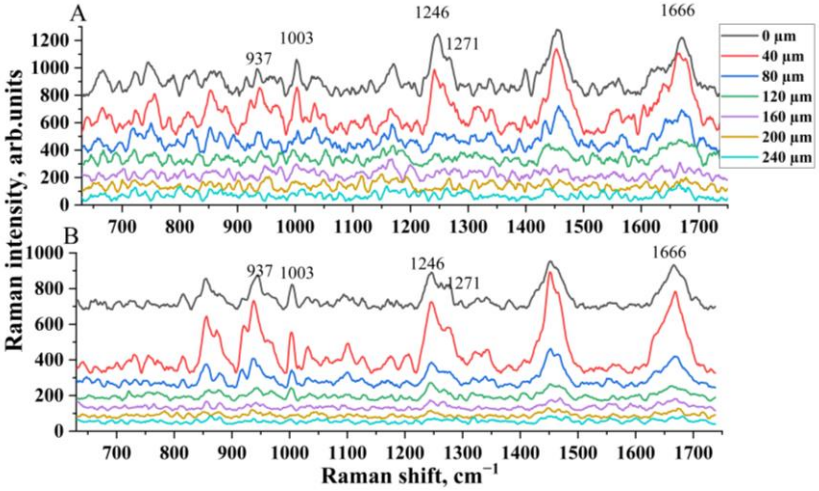

Figure 4.23: *In-depth evolution of the Raman spectra of control ex vivo porcine ear skin from 0 to 240 µm acquired using (A) 633 nm and (B) 785 nm excitation. The Raman spectra were shifted along the ordinate for clarity.*

The main Raman peaks observed at the skin surface (0 µm) correspond to 1666 cm^{-1} (amide I band), 1426 cm^{-1} (C–C stretching vibrations), 1271 cm^{-1} (amide III), 1246 cm^{-1} (amide III), 1003 cm^{-1} (phenylalanine/urea), and 937 cm^{-1}(C–C stretch backbone) [38]. As can be seen from Figure 4.23A-B, the Raman peaks related to the skin monotonically diminish with increasing probing depth for both excitation wavelengths. This attenuation is more prominent at 633 nm excitation, resulting in greater noise compared to 785 nm. Some

main Raman peaks in the 633 nm spectra become indistinct within the depth range from 80 to 120 µm, primarily due to the increased noise. In contrast, with 785 nm excitation, the same Raman peaks related to the skin can be resolved even at a depth of 160 µm. The decline in Raman intensities can be attributed to the limited penetration and detection of light, as a result of the pronounced scattering and absorption properties of the skin.

As discussed in Section 3.3, 633 nm offers two notable advantages: First, Raman spectra with larger amplitude and higher resolution, permitting a more accurate probing of skin conformation compared to laser excitation at 785 nm. Second, the use of laser excitation at 633 nm permits for the simultaneous coverage of both FP and HWN regions with the maximum sensitivity of the CCD detector, as demonstrated in Section 4.2 on the DM experiment. While 785 nm possesses a higher penetration depth ability into the skin layers, but the combination of the OC method with 633 nm laser excitation will provide both high scanning depth and better spectral resolution for skin investigations.

In this section, Gly and DMSO were used as OCAs due to their pharmacokinetics and biocompatibility, making them suitable for application in biological tissues. Also, they have different penetration mobility properties into the skin layers, with DMSO having a faster diffusion rate compared to the Gly [45]. Figure 4.24A-B illustrates the Raman spectra of different OCAs recorded under 633 and 785 nm excitation.

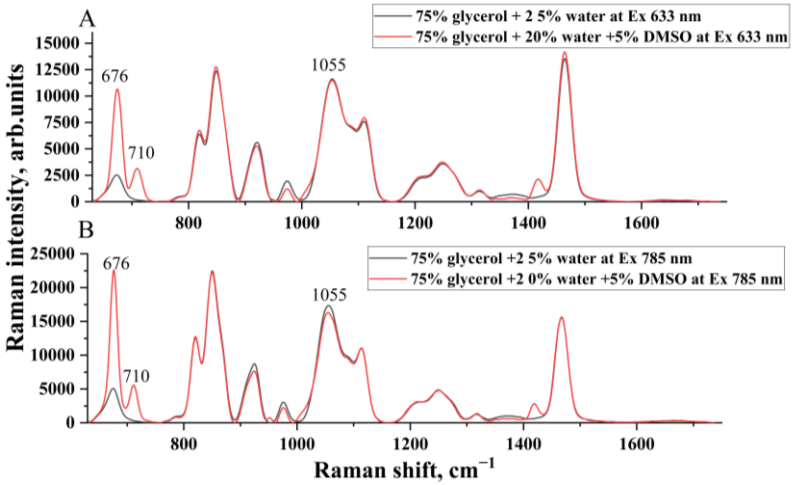

Figure 4.24: *Raman spectra were acquired using (A) 633 nm and (B) 785 nm excitation for both used OCAs: 75% glycerol + 20% distilled water + 5% DMSO and 75% glycerol + 25% distilled water.*

The Gly-related Raman peak appears at 850 and 1055 cm^{-1}, and for DMSO-related Raman peaks are found at 676 and 710 cm^{-1}, corresponding to symmetric and asymmetric vibration (CSC) modes, respectively. To investigate the impact of the OC method on the Raman spectra recorded from different *ex vivo* skin layers at various depths, a comparative

study was conducted between Raman spectra of control and treated *ex vivo* skin with different OCAs using both 633 nm and 785 nm excitation sources. Figures 4.25 and 4.25 illustrate a series of Raman spectra of control and treated skin for 30 and 60 min with all OCAs.

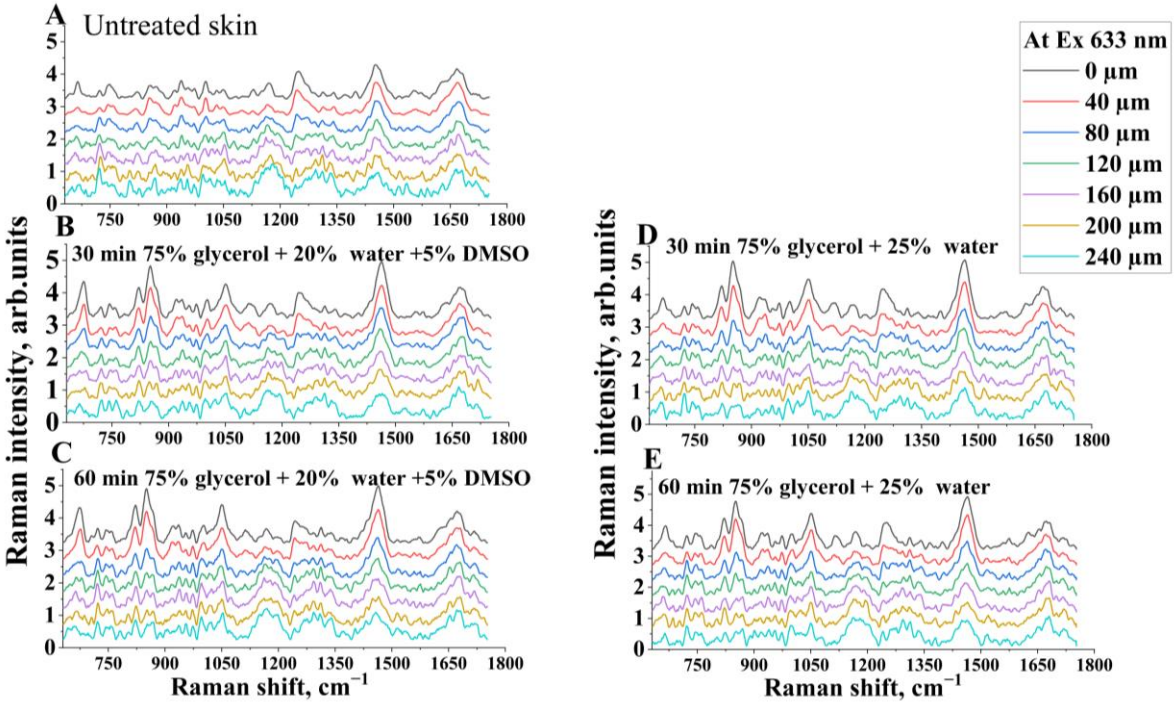

Figure 4.25: *Raman spectra from 0 to 240 µm depths of ex vivo porcine ear skin acquired with 633 nm excitation. (A) control skin sample, skin treated with 75% glycerol + 20% distilled water + 5% DMSO for (B) 30 and (C) 60 min, and skin treated with 75% glycerol + 25% distilled water for (D) 30, and (E) 60 min. The Raman spectra were normalized for the intensity in the 1590 to 1750 cm^{-1} region and shifted along the ordinate for more clarity.*

Figures 4.25 and 4.26 demonstrate that the main Raman peak intensities in deeper layers of the skin before and after OC treatment for both laser sources. The Raman intensities at 1003, 1246, and 1271 cm^{-1} are significantly enhanced and resolved after OC treatment for both exposure times when using 633 nm excitation, even at a depth of 240 µm. Moreover, for both excitation sources longer treatment time at 60 min leads to more pronounced OC effect. This suggests that the OC method, when combined with CRM utilizing a 633 nm laser source, allows for achieving similar or even better scanning depth and Raman spectra quality compared to CRM utilizing a 785 without the OC method. It is worth to notice that the Raman peaks are resolved for all depths after OCA application for both treatment times, indicating that all OCAs reached all probing depths in the *ex vivo* skin during the measurement.

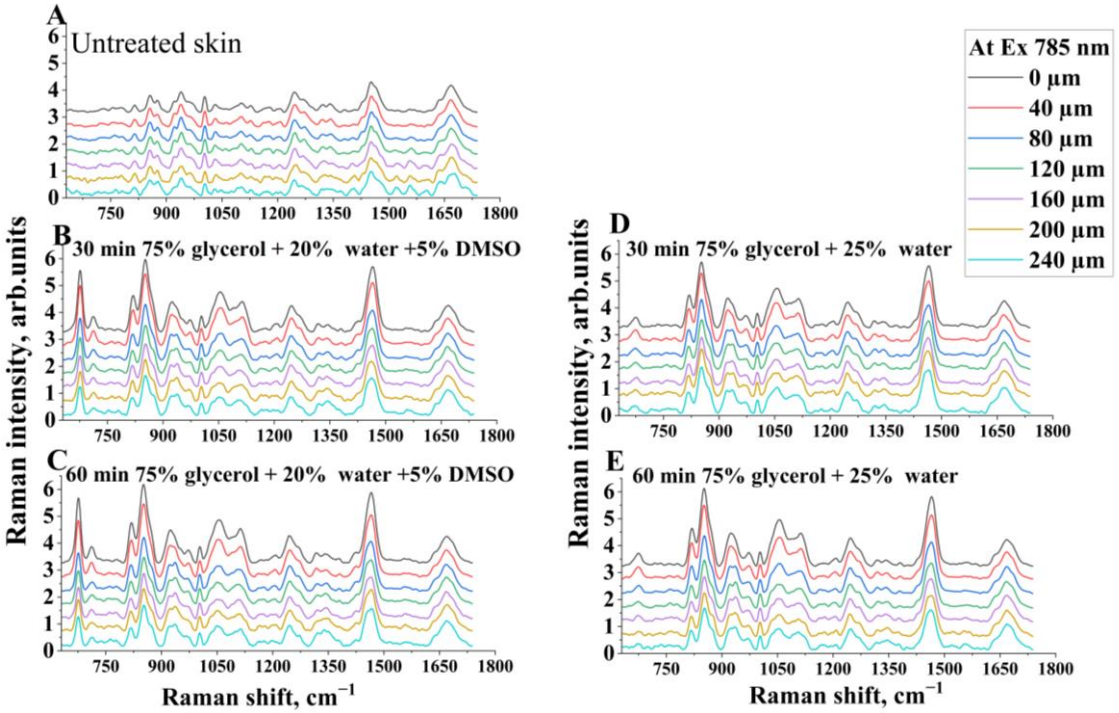

Figure 4.26: *Raman spectra from 0 to 240 µm depths of ex vivo porcine ear skin acquired with 785 nm excitation. (A) control skin sample, skin treated with 75% glycerol + 20% distilled water + 5% DMSO for (B) 30 and (C) 60 min, and skin treated with 75% glycerol + 25% distilled water for (D) 30 and (E) 60 min. The Raman spectra were normalized for the intensity in the 1590 to 1750 cm^{-1} region and shifted along the ordinate for more clarity.*

In order to have a straight comparison of OC_{eff} results at various depths, the Raman spectra were baseline-subtracted and normalized at intervals from 1590 to 1750 cm^{-1} (amide I band) [99,135,137]. It is crucial to bear in mind that normalization on this interval may not be fully accurate at a depth of 40 µm, as this depth relates to the stratum spinosum layer. This layer is relatively protein-deficient compared to the *stratum corneum*, which is rich in keratin, and the dermis, which is abundant in collagen types I, III, and elastin [282]. The amide III offers significant distinctions between the predominant skin proteins, collagen types I and IV, as well as the structural variations between the epidermis/dermis boundary, dermis, and epidermis [20]. The intensity ratio of the Raman peak at 1271 to 1246 cm^{-1} (I_{1271}/ I_{1246}) highlights the distinctions between collagen types I and IV in terms of the distribution of proline-poor and proline-rich, respectively [283].

To examine the influence of OCAs on collagen types I and IV in skin samples, the effectiveness of OC on the intensity of the Raman peaks at 1003, 1246, and 1271 cm^{-1} was investigated for various depths [284,285]. The OC_{eff} was determined as the ratio of Raman intensities after and before treatment (I_{OC}/I) [38]. Figure 4.27 A-C illustrates the OC_{eff} values of Raman peaks corresponding to proline-rich (1246 cm^{-1}, non-polar), proline-poor (1271

cm^{-1}, polar), and 1003 cm^{-1} (phenylalanine/urea) after OCAs treatment for 30 and 60 min. It is clearly seen that the OC_{eff} for both OCAs and excitation sources improves with increasing treatment time. Furthermore, the OC_{eff} for the 785 nm excitation is higher compared to 633 nm, which can be attributed to the better penetration ability of the longer wavelength laser into the tissue.

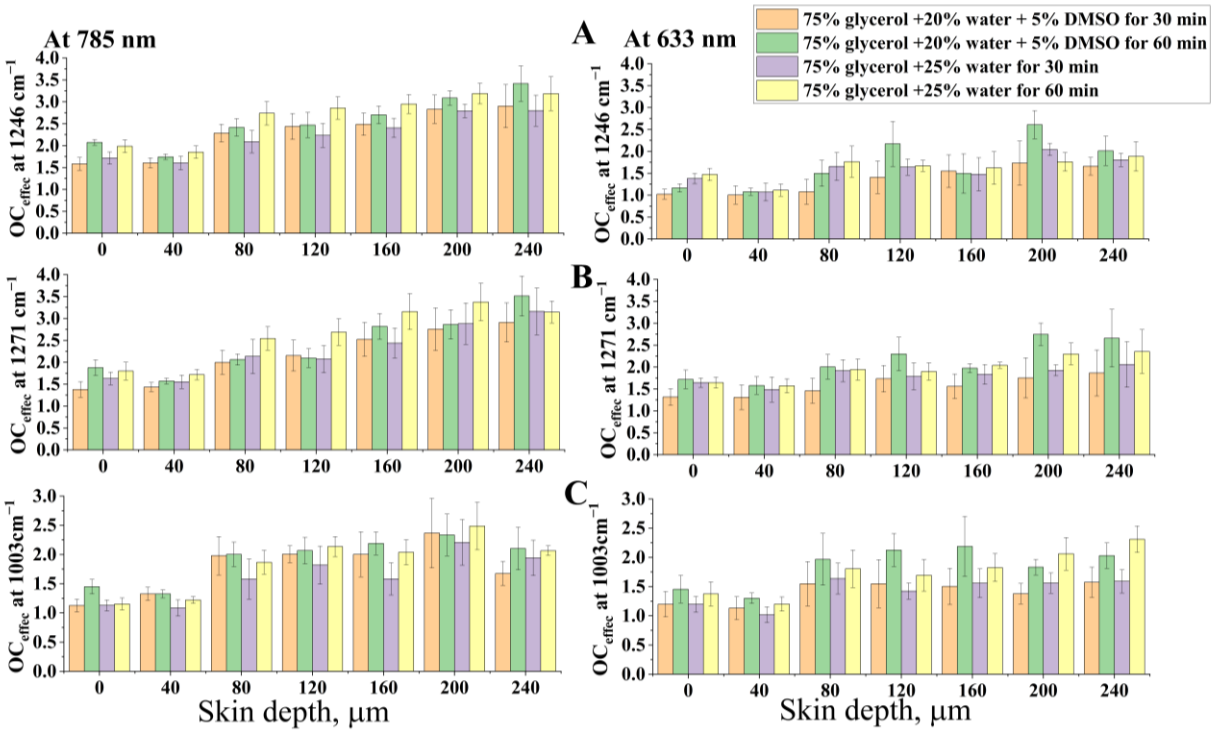

Figure 4.27: *The efficiency of optical clearing of ex vivo porcine skin treated with the two OCAs for 30 min and 60 min for the Raman peaks at (A) 1246 cm^{-1} (amide III) (B) 1271 cm^{-1} (amide III) and (C) 1003 cm^{-1} (phenylalanine/urea) using 633 nm (right) and 785 nm (left) excitations.*

For 785 nm excitation, the highest OC_{eff} values were achieved for Raman peaks at 1246 and 1271 cm^{-1} (3.4 and 3.5, respectively) at a depth of 240 μm after 60 min of Gly-water-DMSO solution treatment. Regarding to the Raman peak at 1003 cm^{-1}, the maximum OC_{eff} (2.4) was reached at a depth 200 μm after 60 min of Gly-water solution treatment. Overall, both OCAs were found to be efficient agents for OC at all depths after the treatments (30 to 60 min). The addition of 5% DMSO in the OCA significantly improved the OC_{eff} for most investigated depths. The highest increase in OC_{eff} was observed for Raman peaks at 1246 cm^{-1} (from 3.1 to 3.4) and at 1271 cm^{-1} (from 3.1 to 3.5) at a depth of 240 μm. For the 1003 cm^{-1} Raman peak, the highest increase in the OC_{eff} was from 1.9 to 2.1 at a depth of 160 μm. The better performance of the OCA containing DMSO can be attributed to the penetration enhancing properties of DMSO, which is considered to be an OCA itself.

For 633 nm excitation, the maximum OC_{eff} values were obtained for Raman peaks at 1246 and 1271 cm^{-1} (2.6 and 2.7, respectively) at a depth of 200 μm after one hour of Gly-water-DMSO solution treatment. For the Raman peak at 1003 cm^{-1}, the maximum OC_{eff} value (2.3) was obtained a depth of 240 after one hour of Gly-water solution treatment. The longer treatment time for 633 nm excitation also resulted in an increased OC_{eff}, similarly to the case of 785 nm laser. The most substantial improvement in OC_{eff} was observed for the 5% DMSO OCA, specifically at a depth of 200 μm. The OC_{eff} increased from 1.7 to 2.6 for the Raman peak at 1246 cm^{-1} and from 2.3 to 2.5 for the Raman peak at 1271 cm^{-1}. Similarly, for the Raman peak at 1003 cm^{-1}, the highest increase in OC_{eff} from 1.6 to 2.2, was obtained at a depth of 160 μm.

The intensities of collagen-related Raman peaks were found to increase after treatment with both OCAs, which indicates higher arrangement collagen fibers. This enhancement is attributed to the dehydration induced by the OCAs [38]. As mentioned earlier, the OC method combined with CRM plays an important role in medical research. This technique allows for the preservation of signal-to-noise ratio, scanning depth, and spatial resolution, which are vital factors for identifying the early stages of skin diseases and therapy control.

In conclusion, this section presented the results of the OC effect on *ex vivo* porcine skin after OCA applications for 30 and 60 min, assisted by CRM using 633 and 785 nm excitation wavelengths. The results revealed a significant enhancement in the main Raman peak intensities of *ex vivo* skin across all scanning depths following OCA application for both 30 and 60 min with both laser sources. Moreover, the OC method combined with CRM at 633 nm excitation permitted to obtain the better scanning depth, and spectral resolution. The study indicated that OCA comprising 5% DMSO as a penetration enhancer significantly increased OC_{eff} compared to the DMSO-free OCA. Both OCAs were found to clearly enhanced the Raman peak intensities for 1246, 1271, and 1003 cm^{-1}. The first two peaks are related to proteins that undergo significant changes during skin cancer or aging, and the latter plays an important role in skin cancer diagnoses. The combination of chemical enhancers with traditional OCAs offers more efficient OC process, potentially paving the way for safer treatment of biological objects.

Chapter 5: Summary and perspectives

Unlike the gold standards for the diagnosis and monitoring of biological tissue diseases, biopsy and histopathology, which give information on the presence of specific compounds only, confocal Raman microscopy offers a non-invasive and non-destructive tool provides a “fingerprint” characterizing the entire molecular composition of biological tissues and objects. This thesis successfully employed optical clearing to enhance deep tissue-related Raman peaks from *dura mater* and skin. By monitoring Raman spectrum changes over time at different depths during glycerol and glycerol + DMSO treatment as OCA, the impact of the OC process on the tissues was comprehensively investigated.

Firstly, the impact of pure glycerol as an OCA on enhancing Raman scattering at probing depths ranging from 0 to 250 μm in *ex vivo* porcine DM was investigated, focusing on collagen-related Raman peaks, dehydration, and dissociation of collagen. The results demonstrated that glycerol significantly increased the intensities of collagen-related Raman peaks across all depths from 0 to 250 μm. In addition, the contributions of three main collagen-related OC processes were explored. First, tissue dehydration (fast process leading to collagen shrinkage). Second tissue swelling (relatively slow process), both associated with diffusion of Gly molecules into the collagen interfibrillar space (RI matching). Third process related to collagen dissociation due to high glycerol concentration.

Secondly, the impact of topically applied moderate concentration of Gly (50%, considered to be safe for *in vivo* human applications) on collagen-related Raman peak intensities in *ex vivo* dura mater was monitored in real-time at depths ranging from 50 to 200. The diffusivity of glycerol was determined within the passive diffusion model and water migration in DM during the OC process was also investigated. The results indicated a significant enhancement in collagen-related Raman peak intensities across all investigated depths after the OCA treatment, confirming the effectiveness of the OC method.

Depending on the depth, the glycerol diffusion coefficient was found to range from 9.6×10^{-6} to 3.0×10^{-5} cm^2/s with its concentration varying from 0.6 to 20% v/v. Notably, these values were considerably less than the 50% concentration of the originally applied glycerol. The variations in glycerol diffusion coefficient and concentration at different depths, were attributed to the structure and composition of the DM tissue. Furthermore, the changes in water content during the OC process indicated that 50% glycerol leads to tissue dehydration even with very low concentrations inside the tissue. Among the four different types of water,

weakly and strongly bound water were found to have highest concentration in DM tissue, play a crucial role in the glycerol-induced water flux and the overall impact of the OC effect.

The final section of the thesis delves into a comparison of the effects of two different optical clearing agents on collagen-related Raman peaks in *ex vivo* porcine skin, examined by CRM with 633 and 785 nm excitation wavelengths. The results revealed substantial enhancements in the Raman peak intensities of *ex vivo* skin across all probed depths from 0 to 240 μm after OCA treatment for 30 and 60 min. Interestingly, the longer treatment time resulted in a noticeably improved optical clearing effect.

In the case of 633 nm excitation, the OC method allowed to accomplish similar or even better probing depth of the Raman spectra compared to 785 nm excitation without OC. In addition, the results demonstrate that the addition of DMSO to a glycerol-water OCA as penetration enhancer can significantly improve OC efficiency. Both OCAs (glycerol-water with and without DMSO) distinctly enhanced the intensity of the Raman peaks at 1246, 1271, and 1003 cm^{-1}. These peaks are associated to protein alterations in skin aging or cancer progression.

Scientific and significant practical aspects of the study:

Based on the result of this PhD thesis, future studies in this direction could involve optimizing the biocompatibility of OCA and integrating this method into clinical practices for the diagnosis and treatment of brain and skin diseases. This integration aims to enhance the diagnostic and therapeutic capabilities of optical analysis methods. These results could provide valuable insights into the structural alterations induced by glycerol treatment, shedding light on the impact of OC processes on the molecular organization of biological tissues. Furthermore, the presented thesis has a rather general nature and can be employed in a wide field of medicine, including subcutaneously implanted or injected Raman biosensors for *in vivo* glucose monitoring [286,287], nucleic acid nano sensors implanted in *in vivo* porcine skin [288], and *in vivo* diagnostic and cancer detection [289]. Such applications could benefit from the reduced light scattering, thereby improving the Raman signal quality from deeper tissue layers.

Moreover, these results of the impact of Gly on collagen in *dura mater* are particularly relevant to clinical practice due to the widespread use of Gly solutions in patients undergoing neurosurgery and strokes. Gly is employed to reduce edema through water migration (dehydration), thereby lowering intracranial pressure and increasing cerebral blood flow. Furthermore. the results presented in this thesis demonstrate the effectiveness of the OC

process in controlling the optical properties of *dura mater*, paving the way for improved in-depth monitoring of human and animal brains during laser therapy and diagnostics. Additionally, these results have potential applications in forensic purpose applications and Burr holes surgery, where tiny holes are drilled into the skull reduce brain pressure caused by fluid compression. It is worth to notice that DM is similar to many collagen-based tissues like the sclera and dermis. Therefore, these results may be translated to other fibrous biological tissues. This opens up exciting possibilities for the application of OC in a wider range of clinical practice.

Chapter 6: New scientific results

In this thesis, I investigated the impact of optical cleaning on collagen-related Raman peaks to control the optical properties of biological objects (*ex vivo* porcine *dura mater* and skin-dermis) in-depth using confocal Raman micro-spectroscopy. The scientific results achieved in this research work are summarized in the following points:

1- I determined the impact of pure glycerol as an optical clearing agent on *ex vivo dura mater* tissue with confocal Raman micro-spectroscopy at different depths from 0 to 250 μm and treatment times [T1].

   i. The intensities of collagen-related Raman peaks were significantly enhanced across all depths after glycerol application. This enhancement was attributed to collagen dehydration, as evidenced by the change in the I_{937}/I_{926} Raman peak intensity ratio induced by glycerol, which suggests collagen shrinkage.

   ii. Deconvolution of the Raman spectra using Gaussian-Lorentzian functions revealed evidence of collagen dissociation. The observed upshift of the 1666 cm^{-1} Raman peak indicated structural alterations in the molecular geometry of the amide I group of collagen, suggesting dissociation of triple helix chains into simpler structures such as single or double strings. This dissociation was attributed to the high concentration of glycerol.

2- I determined the impact of a moderate concertation of 50% glycerol, as an optical clearing agent on *ex vivo dura mater* at different depths, including measuring the diffusivity of glycerol and tracking the changes in the water content [T2].

   i. A new approach was developed to determine the diffusion coefficient and concentration by measuring the actual concentration of glycerol using the Raman peak intensity of the immobilized proteins as a reference. The diffusion coefficient of 50% glycerol ranged from 9.6×10^{-6} to 3.0×10^{-5} cm^2/s, and its concentration from 0.6 to 20% v/v at different depths confirming the effectiveness of the optical clearing method with a moderate concertation. This method can be applied for different optical cleaning agents and drugs.

   ii. The application of a 50% glycerol solution caused significant changes in the total water content of the *dura mater*, reflecting tissue dehydration during the

optical cleaning process. Even at low concentrations of glycerol inside the sample. The most prevalent water states in the *dura mater* with highest concentration were the weakly and strongly-bound water types. These water forms play a crucial role in the optical cleaning process, influencing the glycerol-induced water migrations.

3- I determined the impact of various optical cleaning agents containing glycerol and dimethyl sulfoxide on the Raman spectra of *ex vivo* porcine skin-dermis using 633 and 785 nm excitations at different depths from 0 to 240 μm during the optical clearing for both 30 and 60 min, together with the influence of dimethyl sulfoxide as an enhancer for the optical cleaning process [T3].

   i. Optical cleaning significantly enhanced the excitation depth and the quality of Raman spectra obtained using 633 nm excitation confocal Raman micro-spectroscopy, exceeding the capabilities of 785 nm excitation without optical clearing. In addition, the results show enhancement in Raman peak intensities of *ex vivo* skin for both excitation wavelengths across all scanning depths after optical clearing treatment.

   ii. The addition of 5% dimethyl sulfoxide, as a penetration enhancer into the optical cleaning agent further increases the efficiency of the optical cleaning compared to the DMSO-free optical cleaning agent. The most substantial improvement in optical cleaning efficiency values were obtained for Raman peaks at 1246 and 1271 cm^{-1} (2.6 and 2.7, respectively) at a depth of 200 μm after one hour using 633 nm excitation.

Publications related to the Ph.D. thesis

[T1] Ali Jaafar, Roman Holomb, Anton Y. Sdobnov, Zsombor Ocskay, Zoltán Jakus, Valery V. Tuchin and Miklós Veres; *Ex vivo* confocal Raman microspectroscopy of porcine *dura mater* supported by optical clearing; https://doi.org/10.1002/jbio.202100332; Q2; IF: 2.8, MTMT ID: 32587417.

[T2] Ali Jaafar, Maxim E. Darvin, Valery V. Tuchin and Miklós Veres; Confocal Raman Micro-Spectroscopy for Discrimination of Glycerol Diffusivity in *Ex vivo* porcine *dura mater*; Life 2022, 12(10), 1534; https://doi.org/10.3390/life12101534; Q2; IF: 3.2, MTMT ID: 33204848.

[T3] Ali Jaafar, Malik H. Mahmood, Roman Holom, László Himics, Tamás Váczi, Anton Y. Sdobnov, Valery V. Tuchin and Miklós Veres; *Ex-vivo* confocal Raman microspectroscopy of porcine skin with 633/785-nm laser excitation and optical clearing with glycerol/water/DMSO solution; Journal of Innovative Optical Health Sciences Vol. 14, No. 05, 2142003,2021, https://doi.org/10.1142/S1793545821420037; Q2; IF: 2.3, MTMT ID: 32078778.

International conferences

[IC1] Ali Jaafar, Malik H. Mahmood, R. Holomb, L. Himics, V. V. Tuchin, Miklós Veres; Confocal Raman microspectroscopy of porcine skin ex vivo using laser excitation at 633 nm and optical clearing with glycerol/water/DMSO solution; for Internet Poster presentation, Conference on Internet Biophotonics XIII, annual conference Saratov Fall Meeting SFM'20, September 29- October 1, at Saratov, Russia, 2020.

[IC2] Ali Jaafar, Ágnes N. Szokol, Malik H. Mahmood, István Rigó, Anton Y. Sdobnov, Valery V. Tuchin and Miklós Veres; *Ex vivo* confocal Raman microspectroscopy of porcine dura mater using 532 nm excitation and optical clearing; for Internet Poster presentation, Conference on Internet Biophotonics, annual conference Saratov Fall Meeting SFM21, September 29- October 1, at Saratov, Russia, 2021.

[IC3] Malik H. Mahmood, **Ali Jaafar,** László Himics, László Péter, Ágnes Nagyné Szokol, István Rigó, Shereen Zangana, Attila Bonyár, Miklós Veres; Surface-enhanced Raman scattering substrates for DNA detection based on nanogold-capped poly (DEGDMA) microparticles; proceedings of the 25th Saratov Fall Meeting Conference, Laser Physics and Biophotonics, at Saratov, Russia, September 27- October 1, 2021.

[IC4] Ali Jaafar, Abbas Albarazanchi, Maxim E. Darvin, Valery V. Tuchin, Miklós Veres; Impact of e-cigarette liquid on porcine lung tissue *ex vivo* confocal Raman micro-spectroscopy study; oral presentation, The 2nd Spring Biophotonics Conference 15-18, June, Espinho, Portugal, 2023.

Further scientific publications

[F1] Roman Holomb, Oleksandr Kondrat, Volodimir Mitsa, Alexander Mitsa, David Gevczy, Dmytro Olashyn, László Himics, István Rigó, **Ali Jaafar**, Malik H. Mahmood, Tamás Váczi, Aladár Czitrovszky, Attila Csík, Viktor Takáts, Miklós Veres; Gold nanoparticle assisted synthesis and characterization of As-S crystallites: scanning electron microscopy, X-ray diffraction, energy-dispersive X-ray and Raman spectroscopy combined with DFT calculations, doi.org/10.1016/j.jallcom.2021.162467; Q1; IF: 5.3, MTMT ID: 32550898.

[F2] Malik H Mahmood, **Ali Jaafar**, László Himics, László Péter, István Rigó, Shereen Zangana, Attila Bonyár and Miklós Veres; Nanogold-capped poly (DEGDMA) microparticles as surface-enhanced Raman scattering substrates for DNA detection; Journal of Physics D: Applied Physics, 2022, Volume 55, Number 40; DOI 10.1088/1361-6463/ac7bba; Q2; IF: 3.4, MTMT ID: 33041627.

[F3] Ali Jaafar, Abbas Albarazanchi, Mohammed Jawad Kadhim, Maxim E Darvin, Tamás Váczi, Valery V Tuchin and Miklós Veres; Impact of e-cigarette liquid on porcine lung tissue–ex vivo confocal Raman micro-spectroscopy study; J.Biophotonics, 2023, e202300336. https://doi.org/10.1002/jbio.202300336; Q2; IF: 2.8, MTMT ID: 34396683.

[F4] Marowa Yass, Ahmed Al-Haddad, Mohammed Jassim Mohammed Ali, **Ali Jaafar** and Miklós Veres; Effectiveness of Green Synthesized Zinc Oxide Nanoparticles against Extensively Drug-resistant Klebsiella pneumoniae; Biomedical and Biotechnology Research Journal 7(3): p 497-503, Jul–Sep 2023. DOI: 10.4103/bbrj.bbrj_167_23; Q3; IF: 1.4, MTMT ID: 34425261.

Acknowledgements

This thesis is the result of research work performed at the Institute of Solid State Physics and Optics, HUN-REN Wigner Research Centre for Physics, Budapest, Hungary in 2019–2024.

First and foremost, all praises and thanks to ALLAH, the Almighty, for His showers of blessings throughout my research work, and with his mercy I completed the research successfully.

I would like to express my sincere gratitude to Dr. Miklós Veres for the supervision of my studies, assistance and providing me with all the necessary conditions for research. For the hours spent correcting my articles, present thesis manuscript, discussing scientific work, results and directions for the development of our research. For great kindness to people, endless optimism and sense of humour even in difficult moments. For interesting conversations affecting all aspects, not only the scientific sphere. Finally, for a huge impact on my development as a researcher and scientist.

My sincere gratitude I would like to express to my mentor and teacher Prof. Valery Tuchin, Head of Chair of Optics and Biophotonics at Saratov National Research State University (Russia), who guided and inspired me from the very beginning of my research work and for all the help, advice and support provided to me in my journey towards the doctoral degree and for opening this boundless world of physics to me.

I also thank Dr. Maxim Darvin from Charité-Universitätsmedizin Berlin (Germany) for his support and useful advice. For the joint discussion of scientific results and the time spent on correcting my scientific publications. For giving me this invaluable opportunity to participate in the scientific interaction in Charité-Universitätsmedizin (Germany). For inexhaustible optimism and a fresh look at things that allowed me to become a researcher and scientist, seeing such an example next to me.

I also thank the members of my Follow-up group: Dr. László Himics, Dr. Tamás Váczi, Dr. István Rigó, Dr. Roman Holomb, Dr. Judit Kámán, Dr. Nagy Attila, Dávid Gál, Csáki Attila and Benedek Márk, for their support and useful discussions. In addition, I very much appreciate the help of Prof. Aladár Czitrovszky, former director of SZFI, for his help, advice and support. Special thanks to Ágnes Szokol for her help with many administrative issues. For kindness and hospitality, which allowed me to feel like a part of the team and for moral and comprehensive support in difficult times.

I also thank the members of Department of Physics, College of Science, Mustansiriyah University, Baghdad, Iraq. Especially, Dr. Hanan, Dr. Abbas, Dr. Rafid, Dr. Firas, and Dr. Ahmed for their guidance, responsiveness and attentiveness since I was a bachelor student in their laboratory. For countless rich conversations and valuable advice.

I would also like to separately express my gratitude to Alexey Bashkatov, who, unfortunately, passed away prematurely due to illness. His vast experience in the field of spectroscopy, biophotonics and physics in general has greatly influenced the development of my skills and my development as a scientist and researcher. I also thank Prof. Elina Genina and Prof. Vladimir Ryabukho for their guidance, responsiveness and attentiveness since I was a master student in their laboratory. For countless rich conversations and valuable advice.

My special thanks go to all members of Institute of Solid State Physics and Optics Wigner Research Centre for Physics for the friendly working environment that surrounded me during all these years. I am especially grateful to my present and former colleagues whose became my dearest friends, namely, Dr. Malik, Dr. Ameer, Loris Busch and Anton Y. Sdobnov for always being ready to help.

I also wish to thank my family for supporting me during all the years of my study. I am grateful to my mother for raising me and for supporting of my choices and my lovely sister and three brothers and their children.

Finally, I would like to acknowledge the financial support provided by the Ministry of Higher Education and Scientific Research, Baghdad (Iraq), and Hungarian Government, The Ministry of Human Capacities, Tempus Public Foundation (TPF) for granting my Ph.D. scholarship under the program of Stipendium Hungaricum (SH).

Finally, I apologize to everyone I forgot to mention.

References

1. Keiser, G. *Biophotonics*; Graduate Texts in Physics; Second.; Springer Nature Singapore: Singapore, **2022**; ISBN 978-981-19-3481-0.
2. Wilson, B.C.; Jermyn, M.; Leblond, F. Challenges and Opportunities in Clinical Translation of Biomedical Optical Spectroscopy and Imaging. *J. Biomed. Opt.* **2018**, *23*, 1, doi:10.1117/1.jbo.23.3.030901.
3. Stevens, A.R.; Stickland, C.A.; Harris, G.; Ahmed, Z.; Oppenheimer, P.G.; Belli, A.; Davies, D.J. Raman Spectroscopy as a Neuromonitoring Tool in Traumatic Brain Injury : A Systematic Review and Clinical Perspectives. **2022**.
4. Darvin, M.E.; Schleusener, J.; Lademann, J.; Choe, C.-S. Current Views on Non-Invasive in Vivo Determination of Physiological Parameters of the Stratum Corneum Using Confocal Raman Microspectroscopy. *Skin Pharmacol. Physiol.* **2022**, *35*, 125–136, doi:10.1159/000521416.
5. Lee, K.S.; Landry, Z.; Pereira, F.C.; Wagner, M.; Berry, D.; Huang, W.E.; Taylor, G.T.; Kneipp, J.; Popp, J.; Zhang, M.; et al. Raman Microspectroscopy for Microbiology. *Nat. Rev. Methods Prim.* **2021**, *1*.
6. Azemtsop Matanfack, G.; Pistiki, A.; Rösch, P.; Popp, J. Raman Stable Isotope Probing of Bacteria in Visible and Deep Uv-Ranges. *Life* **2021**, *11*, doi:10.3390/life11101003.
7. DePaoli, D.; Lemoine, É.; Ember, K.; Parent, M.; Prud'homme, M.; Cantin, L.; Petrecca, K.; Leblond, F.; Côté, D.C. Rise of Raman Spectroscopy in Neurosurgery: A Review. *J. Biomed. Opt.* **2020**, *25*, 1, doi:10.1117/1.jbo.25.5.050901.
8. Mandrell, C.T.; Holland, T.E.; Wheeler, J.F.; Esmaeili, S.M.A.; Amar, K.; Chowdhury, F.; Sivakumar, P. Machine Learning Approach to Raman Spectrum Analysis of Mia Paca-2 Pancreatic Cancer Tumor Repopulating Cells for Classification and Feature Analysis. *Life* **2020**, *10*, 1–14, doi:10.3390/life10090181.
9. Cordero, E. In-Vivo Raman Spectroscopy: From Basics to Applications. *J. Biomed. Opt.* **2018**, *23*, 071210–071223, doi:10.1117/1.jbo.23.7.071210.
10. Kong, K.; Kendall, C.; Stone, N.; Notingher, I. Raman Spectroscopy for Medical Diagnostics - From in-Vitro Biofluid Assays to in-Vivo Cancer Detection. *Adv. Drug Deliv. Rev.* **2015**, *89*, 121–134, doi:10.1016/j.addr.2015.03.009.
11. Latka, I.; Dochow, S.; Krafft, C.; Dietzek, B.; Popp, J. Fiber Optic Probes for Linear and Nonlinear Raman Applications - Current Trends and Future Development. *Laser Photonics Rev.* **2013**, *7*, 698–731, doi:10.1002/lpor.201200049.
12. Brauchle, E.; Schenke-Layland, K. Raman Spectroscopy in Biomedicine - Non-Invasive in Vitro Analysis of Cells and Extracellular Matrix Components in Tissues. *Biotechnol. J.* **2013**, *8*, 288–297, doi:10.1002/biot.201200163.
13. Lizio, M.G.; Boitor, R.; Notingher, I. Selective-Sampling Raman Imaging Techniques for: Ex Vivo Assessment of Surgical Margins in Cancer Surgery. *Analyst* **2021**, *146*, 3799–3809, doi:10.1039/d1an00296a.
14. Becker, L.; Lu, C.E.; Montes-Mojarro, I.A.; Layland, S.L.; Khalil, S.; Nsair, A.; Duffy, G.P.; Fend, F.; Marzi, J.; Schenke-Layland, K. Raman Microspectroscopy Identifies Fibrotic Tissues in Collagen-Related Disorders via Deconvoluted Collagen Type I Spectra. *Acta Biomater.* **2023**, *162*, 278–291, doi:10.1016/j.actbio.2023.03.016.

15. Santos, I.P.; Barroso, E.M.; Bakker Schut, T.C.; Caspers, P.J.; Van Lanschot, C.G.F.; Choi, D.H.; Van Der Kamp, M.F.; Smits, R.W.H.; Van Doorn, R.; Verdijk, R.M.; et al. Raman Spectroscopy for Cancer Detection and Cancer Surgery Guidance: Translation to the Clinics. *Analyst* **2017**, *142*, 3025–3047, doi:10.1039/c7an00957g.

16. Martinez, M.G.; Bullock, A.J.; MacNeil, S.; Rehman, I.U. Characterisation of Structural Changes in Collagen with Raman Spectroscopy. *Appl. Spectrosc. Rev.* **2019**, *54*, 509–542, doi:10.1080/05704928.2018.1506799.

17. Di, L.; Eichberg, D.G.; Park, Y.J.; Shah, A.H.; Jamshidi, A.M.; Luther, E.M.; Lu, V.M.; Komotar, R.J.; Ivan, M.E.; Gultekin, S.H. Rapid Intraoperative Diagnosis of Meningiomas Using Stimulated Raman Histology. *World Neurosurg.* **2021**, *150*, e108–e116, doi:10.1016/j.wneu.2021.02.097.

18. Jelke, F.; Mirizzi, G.; Borgmann, F.K.; Husch, A.; Slimani, R.; Klamminger, G.G.; Klein, K.; Mombaerts, L.; Gérardy, J.J.; Mittelbronn, M.; et al. Intraoperative Discrimination of Native Meningioma and Dura Mater by Raman Spectroscopy. *Sci. Rep.* **2021**, *11*, 1–10, doi:10.1038/s41598-021-02977-7.

19. Koljenović, S.; Schut, T.B.; Vincent, A.; Kros, J.M.; Puppels, G.J. Detection of Meningioma in Dura Mater by Raman Spectroscopy. *Anal. Chem.* **2005**, *77*, 7958–7965, doi:10.1021/ac0512599.

20. Nguyen, T.T.; Gobinet, C.; Feru, J.; -Pasco, S.B.; Manfait, M.; Piot, O. Characterization of Type i and IV Collagens by Raman Microspectroscopy: Identification of Spectral Markers of the Dermo-Epidermal Junction. *Spectrosc. (New York)* **2012**, *27*, 421–427, doi:10.1155/2012/686183.

21. Pezzotti, G.; Boffelli, M.; Miyamori, D.; Uemura, T.; Marunaka, Y.; Zhu, W.; Ikegaya, H. Raman Spectroscopy of Human Skin: Looking for a Quantitative Algorithm to Reliably Estimate Human Age. *J. Biomed. Opt.* **2015**, *20*, 065008, doi:10.1117/1.jbo.20.6.065008.

22. Nguyen, T.T.; Happillon, T.; Feru, J.; Brassart-Passco, S.; Angiboust, J.F.; Manfait, M.; Piot, O. Raman Comparison of Skin Dermis of Different Ages: Focus on Spectral Markers of Collagen Hydration. *J. Raman Spectrosc.* **2013**, *44*, 1230–1237, doi:10.1002/jrs.4355.

23. Votteler, M.; Carvajal Berrio, D.A.; Pudlas, M.; Walles, H.; Stock, U.A.; Schenke-Layland, K. Raman Spectroscopy for the Non-Contact and Non-Destructive Monitoring of Collagen Damage within Tissues. *J. Biophotonics* **2012**, *5*, 47–56, doi:10.1002/jbio.201100068.

24. Xiao, Y.; Guo, M.; Zhang, P.; Shanmugam, G.; Polavarapu, P.L.; Hutson, M.S. Wavelength-Dependent Conformational Changes in Collagen after Mid-Infrared Laser Ablation of Cornea. *Biophys. J.* **2008**, *94*, 1359–1366, doi:10.1529/biophysj.107.114389.

25. Dehring, K.A.; Smukler, A.R.; Roessler, B.J.; Morris, M.D. Correlating Changes in Collagen Secondary Structure with Aging and Defective Type II Collagen by Raman Spectroscopy. *Appl. Spectrosc.* **2006**, *60*, 366–372, doi:10.1366/000370206776593582.

26. Huang, Z.; McWilliams, A.; Lui, H.; McLean, D.I.; Lam, S.; Zeng, H. Near-Infrared Raman Spectroscopy for Optical Diagnosis of Lung Cancer. *Int. J. Cancer* **2003**, *107*, 1047–1052, doi:10.1002/ijc.11500.

27. Stone, N.; Kendall, C.; Smith, J.; Crow, P.; Barr, H. Raman Spectroscopy for Identification of Epithelial Cancers. *Faraday Discuss.* **2004**, *126*, 141–157, doi:10.1039/b304992b.

28. Lin, K.; Wang, J.; Zheng, W.; Ho, K.Y.; Teh, M.; Yeoh, K.G.; Huang, Z. Rapid Fiber-Optic Raman Spectroscopy for Real-Time in Vivo Detection of Gastric Intestinal Metaplasia during Clinical Gastroscopy. *Cancer Prev. Res.* **2016**, *9*, 476–483, doi:10.1158/1940-6207.CAPR-15-0213.

29. Taketani, A.; Hariyani, R.; Ishigaki, M.; Andriana, B.B.; Sato, H. Raman Endoscopy for the in Situ Investigation of Advancing Colorectal Tumors in Live Model Mice. *Analyst* **2013**, *138*,

4183–4190, doi:10.1039/c3an00169e.

30. Kong, K.; Zaabar, F.; Rakha, E.; Ellis, I.; Koloydenko, A.; Notingher, I. Towards Intra-Operative Diagnosis of Tumours during Breast Conserving Surgery by Selective-Sampling Raman Micro-Spectroscopy. *Phys. Med. Biol.* **2014**, *59*, 6141–6152, doi:10.1088/0031-9155/59/20/6141.

31. Sdobnov, A.Y.; Darvin, M.E.; Genina, E.A.; Bashkatov, A.N.; Lademann, J.; Tuchin, V. V. Recent Progress in Tissue Optical Clearing for Spectroscopic Application. *Spectrochim. Acta - Part A Mol. Biomol. Spectrosc.* **2018**, *197*, 216–229, doi:10.1016/j.saa.2018.01.085.

32. Valery Tuchin *Tissue Optics : Light Scattering Methods and Instruments for Medical Diagnosis*; Third Edit.; SPIE Press, Bellingham, WA, **2015**; ISBN 9781628415162.

33. Genina, E.A.; Bashkatov, A.N.; Tuchin, V. V. Tissue Optical Immersion Clearing. *Expert Rev. Med. Devices* **2010**, *7*, 825–842, doi:10.1586/erd.10.50.

34. Tuchin, V. V.; Maksimova, I.L.; Zimnyakov, D.A.; Kon, I.L.; Mavlutov, A.K.; Mishin, A.A. Light Propagation in Tissues with Controlled Optical Properties. *Proc. SPIE - Int. Soc. Opt. Eng.* **1996**, *2925*, 118–142, doi:10.1117/12.281502.

35. V.V.Tuchin, D.Zhu, E.A.Genina (Eds.) *Handbook of Tissue Optical Clearing: New Prospects in Optical Imaging*; 1st ed.; Taylor & Francis Group, LLC, CRC Press, **2022**; ISBN 2013206534.

36. Oliveira, L.M.C.; Tuchin, V.V. *The Optical Clearing Method - A New Tool for Clinical Practice and Biomedical Engineering*; Springer Nature Switzerland AG, Basel, **2019**; ISBN 978-3-030-33054-5.

37. Schulmerich, M. V.; Cole, J.H.; Dooley, K.A.; Morris, M.D.; Kreider, J.M.; Goldstein, S.A. Optical Clearing in Transcutaneous Raman Spectroscopy of Murine Cortical Bone Tissue. *J. Biomed. Opt.* **2008**, *13*, 021108, doi:10.1117/1.2892687.

38. Sdobnov, A.Y.; Tuchin, V. V.; Lademann, J.; Darvin, M.E. Confocal Raman Microscopy Supported by Optical Clearing Treatment of the Skin - Influence on Collagen Hydration. *J. Phys. D. Appl. Phys.* **2017**, *50*, 285401–285409, doi:10.1088/1361-6463/aa77c9.

39. Darvin, M.E.; Schleusener, J.; Parenz, F.; Seidel, O.; Krafft, C.; Popp, J.; Lademann, J. Confocal Raman Microscopy Combined with Optical Clearing for Identification of Inks in Multicolored Tattooed Skin: In Vivo. *Analyst* **2018**, *143*, 4990–4999, doi:10.1039/c8an01213j.

40. Fu, Y.Y.; Tang, S.C. Optical Clearing Facilitates Integrated 3D Visualization of Mouse Ileal Microstructure and Vascular Network with High Definition. *Microvasc. Res.* **2010**, *80*, 512–521, doi:10.1016/j.mvr.2010.06.003.

41. Nadiarnykh, O.; Campagnola, P.J. Retention of Polarization Signatures in SHG Microscopy of Scattering Tissues through Optical Clearing. *Opt. Express* **2009**, *17*, 5794, doi:10.1364/oe.17.005794.

42. Liang, Y.; Yuan, W.; Mavadia-Shukla, J.; Li, X. Optical Clearing for Luminal Organ Imaging with Ultrahigh-Resolution Optical Coherence Tomography. *J. Biomed. Opt.* **2016**, *21*, 081211, doi:10.1117/1.jbo.21.8.081211.

43. Zhernovaya, O.; Tuchin, V. V.; Leahy, M.J. Enhancement of OCT Imaging by Blood Optical Clearing in Vessels-A Feasibility Study. *Photonics Lasers Med.* **2016**, *5*, 151–159, doi:10.1515/plm-2016-0004.

44. Larin, K. V; Tuchin, V. V Functional Imaging and Assessment of the Glucose Diffusion Rate in Epithelial Tissues in Optical Coherence Tomography. *Quantum Electron.* **2008**, *38*, 551–556, doi:10.1070/qe2008v038n06abeh013850.

45. Jiang, J.; Boese, M.; Turner, P.; Wang, R.K. Penetration Kinetics of Dimethyl Sulphoxide and Glycerol in Dynamic Optical Clearing of Porcine Skin Tissue in Vitro Studied by Fourier

Transform Infrared Spectroscopic Imaging. *J. Biomed. Opt.* **2008**, *13*, 021105, doi:10.1117/1.2899153.

46. Zimmerley, M.; McClure, R.A.; Choi, B.; Potma, E.O. Following Dimethyl Sulfoxide Skin Optical Clearing Dynamics with Quantitative Nonlinear Multimodal Microscopy. *Appl. Opt.* **2009**, *48*, 79–87, doi:10.1364/AO.48.000D79.

47. Xu, X.; Wang, R.K. Synergistic Effect of Hyperosmostic Agents of Dimethyl Sulfoxide and Glycerol on Optical Clearing of Gastric Tissue Studied with near Infrared Spectroscopy. *Phys. Med. Biol.* **2004**, *49*, 457–468, doi:10.1088/0031-9155/49/3/008.

48. Liu, P.; Huang, Y.; Guo, Z.; Wang, J.; Zhuang, Z.; Liu, S. Discrimination of Dimethyl Sulphoxide Diffusion Coefficient in the Process of Optical Clearing by Confocal Micro-Raman Spectroscopy. *J. Biomed. Opt.* **2013**, *18*, 020507, doi:10.1117/1.jbo.18.2.020507.

49. Zhu, X.; Huang, L.; Zheng, Y.; Song, Y.; Xu, Q.; Wang, J.; Si, K.; Duan, S.; Gong, W. Ultrafast Optical Clearing Method for Three-Dimensional Imaging with Cellular Resolution. *Proc. Natl. Acad. Sci. U. S. A.* **2019**, *166*, 11480–11489, doi:10.1073/pnas.1819583116.

50. Pan, C.; Cai, R.; Quacquarelli, F.P.; Ghasemigharagoz, A.; Lourbopoulos, A.; Matryba, P.; Plesnila, N.; Dichgans, M.; Hellal, F.; Ertürk, A. Shrinkage-Mediated Imaging of Entire Organs and Organisms Using UDISCO. *Nat. Methods* **2016**, *13*, 859–867, doi:10.1038/nmeth.3964.

51. Hama, H.; Hioki, H.; Namiki, K.; Hoshida, T.; Kurokawa, H.; Ishidate, F.; Kaneko, T.; Akagi, T.; Saito, T.; Saido, T.; et al. ScaleS: An Optical Clearing Palette for Biological Imaging. *Nat. Neurosci.* **2015**, *18*, 1518–1529, doi:10.1038/nn.4107.

52. Hama, H.; Kurokawa, H.; Kawano, H.; Ando, R.; Shimogori, T.; Noda, H.; Fukami, K.; Sakaue-Sawano, A.; Miyawaki, A. Scale: A Chemical Approach for Fluorescence Imaging and Reconstruction of Transparent Mouse Brain. *Nat. Neurosci.* **2011**, *14*, 1481–1488.

53. Ramshaw, J.; Veronica, G. *Biophysical and Chemical Properties of Collagen: Biomedical Applications*; Iop Publishing Ltd: Bristol, UK, **2020**;

54. Ricard-Blum, S. The Collagen Family. *Cold Spring Harb. Perspect. Biol.* **2011**, *3*, 1–19, doi:10.1101/cshperspect.a004978.

55. V. R. Sherman, W. Yang, M.A.M. The Materials Science of Collagen. *J. Mech. Behav. Biomed. Mater.* **2015**, *52*, 22–50.

56. Sibilla, S.; Godfrey, M.; Brewer, S.; Budh-Raja, A.; Genovese, L. An Overview of the Beneficial Effects of Hydrolysed Collagen as a Nutraceutical on Skin Properties: Scientific Background and Clinical Studies. *Open Nutraceuticals J.* **2015**, *8*, 29–42, doi:10.2174/1876396001508010029.

57. Canelón, S.P.; Wallace, J.M. β-Aminopropionitrile-Induced Reduction in Enzymatic Crosslinking Causes in Vitro Changes in Collagen Morphology and Molecular Composition. *PLoS One* **2016**, *11*, 1–13, doi:10.1371/journal.pone.0166392.

58. Shipp, D.W.; Sinjab, F.; Notingher, I. Raman Spectroscopy: Techniques and Applications in the Life Sciences. *Adv. Opt. Photonics* **2017**, *9*, 315, doi:10.1364/aop.9.000315.

59. Bella, J.; Brodsky, B.; Berman, H.M. Hydration Structure of a Collagen Peptide. *Structure* **1995**, *3*, 893–906, doi:10.1016/S0969-2126(01)00224-6.

60. Kramer, R.Z.; Venugopal, M.G.; Bella, J.; Mayville, P.; Brodsky, B.; Berman, H.M. Staggered Molecular Packing in Crystals of a Collagen-like Peptide with a Single Charged Pair. *J. Mol. Biol.* **2000**, *301*, 1191–1205, doi:10.1006/jmbi.2000.4017.

61. Stanley Jacobson, Elliott M.Marcus, P.S. *Neuroanatomy for the Neuroscientist*; Third Edit.; Springer Cham, **2018**; ISBN 9783319601854.

62. Walsh, D.R.; Ross, A.M.; Newport, D.T.; Zhou, Z.; Kearns, J.; Fearon, C.; Lorigan, J.; Mulvihill, J.J.E. Mechanical Characterisation of the Human Dura Mater, Falx Cerebri and

Superior Sagittal Sinus. *Acta Biomater.* **2021**, *134*, 388–400, doi:10.1016/j.actbio.2021.07.043.

63. Walsh, D.R.; Zhou, Z.; Li, X.; Kearns, J.; Newport, D.T.; Mulvihill, J.J.E. Mechanical Properties of the Cranial Meninges: A Systematic Review. *J. Neurotrauma* **2021**, *38*, 1748–1761, doi:10.1089/neu.2020.7288.

64. Protasoni, M.; Sangiorgi, S.; Cividini, A.; Culuvaris, G.T.; Tomei, G.; Dell'Orbo, C.; Raspanti, M.; Balbi, S.; Reguzzoni, M. The Collagenic Architecture of Human Dura Mater: Laboratory Investigation. *J. Neurosurg.* **2011**, *114*, 1723–1730, doi:10.3171/2010.12.JNS101732.

65. Bashkatov, A.N.; Genina, E.A.; Sinichkin, Y.P.; Kochubey, V.I.; Lakodina, N.A.; Tuchin, V. V. Glucose and Mannitol Diffusion in Human Dura Mater. *Biophys. J.* **2003**, *85*, 3310–3318, doi:10.1016/S0006-3495(03)74750-X.

66. Tuchin, V. V *Optical Clearing of Tissues and Blood*; SPIE Press, Bellingham, WA, **2005**; ISBN 0819460060.

67. Kinaci, A.; Bergmann, W.; Bleys, R.L.A.W.; van der Zwan, A.; van Doormaal, T.P.C. Histologic Comparison of the Dura Mater among Species. *Comp. Med.* **2020**, *70*, 170–175, doi:10.30802/AALAS-CM-19-000022.

68. Rua, R.; McGavern, D.B. Advances in Meningeal Immunity. *Trends Mol. Med.* **2018**, *24*, 542–559, doi:10.1016/j.molmed.2018.04.003.

69. Cheshire, E.C.; Malcomson, R.D.G.; Joseph, S.; Biggs, M.J.B.; Adlam, D.; Rutty, G.N. Optical Clearing of the Dura Mater Using Glycerol: A Reversible Process to Aid the Post-Mortem Investigation of Infant Head Injury. *Forensic Sci. Med. Pathol.* **2015**, *11*, 395–404, doi:10.1007/s12024-015-9691-7.

70. Calikoglu, C.; Cakir, M.; Tuzun, Y. Histopathological Investigation of the Effectiveness of Collagen Matrix in the Repair of Experimental Spinal Dura Mater Defects. *Eurasian J. Med.* **2019**, *51*, 133–137, doi:10.5152/eurasianjmed.2018.17422.

71. Liu, W.; Wang, X.; Su, J.; Jiang, Q.; Wang, J.; Xu, Y.; Zheng, Y.; Zhong, Z.; Lin, H. In Vivo Evaluation of Fibrous Collagen Dura Substitutes. *Front. Bioeng. Biotechnol.* **2021**, *9*, 1–12, doi:10.3389/fbioe.2021.628129.

72. Seung Lee, J.; Kim, J.; Ye, Y. sinn; Kim, T. il Materials and Device Design for Advanced Phototherapy Systems. *Adv. Drug Deliv. Rev.* **2022**, *186*, 114339.

73. Ng, K.W.; Lau, W.M. Skin Deep: The Basics of Human Skin Structure and Drug Penetration. *Percutaneous Penetration Enhanc. Chem. Methods Penetration Enhanc. Springer Berlin/Heidelberg, Ger.* **2015**, 3–11, doi:10.1007/978-3-662-45013.

74. Simpson, C.L.; Patel, D.M.; Green, K.J. Deconstructing the Skin: Cytoarchitectural Determinants of Epidermal Morphogenesis. *Nat. Rev. Mol. Cell Biol.* **2011**, *12*, 565–580, doi:10.1038/nrm3175.

75. Farage, M.A.; Miller, K.W.; Elsner, P.; Maibach, H.I. Structural Characteristics of the Aging Skin: A Review. *Cutan. Ocul. Toxicol.* **2007**, *26*, 343–357, doi:10.1080/15569520701622951.

76. Quondamatteo, F. Skin and Diabetes Mellitus: What Do We Know? *Cell Tissue Res.* **2014**, *355*, 1–21, doi:10.1007/s00441-013-1751-2.

77. Igarashi, T.; Nishino, K.; Nayar, S.K. The Appearance of Human Skin: A Survey. *Found. Trends® Comput. Graph. Vis.* **2007**, *3*, 1–95, doi:10.1561/0600000013.

78. van Smeden, J.; Janssens, M.; Gooris, G.S.; Bouwstra, J.A. The Important Role of Stratum Corneum Lipids for the Cutaneous Barrier Function. *Biochim. Biophys. Acta - Mol. Cell Biol. Lipids* **2014**, *1841*, 295–313, doi:10.1016/j.bbalip.2013.11.006.

79. Alhibah, M.; Kröger, M.; Schanzer, S.; Busch, L.; Lademann, J.; Beckers, I.; Meinke, M.C.; Darvin, M.E. Penetration Depth of Propylene Glycol, Sodium Fluorescein and Nile Red into the Skin Using Non-Invasive Two-Photon Excited FLIM. *Pharmaceutics* **2022**, *14*,

doi:10.3390/pharmaceutics14091790.

80. Darvin, M.E. Optical Methods for Non-Invasive Determination of Skin Penetration: Current Trends, Advances, Possibilities, Prospects, and Translation into In Vivo Human Studies. *Pharmaceutics* **2023**, *15*, 2272, doi:10.3390/pharmaceutics15092272.

81. Schleusener, J.; Salazar, A.; Hagen, J. von; Lademann, J.; Darvin, M.E. Retaining Skin Barrier Function Properties of the Stratum Corneum with Components of the Natural Moisturizing Factor—a Randomized, Placebo-Controlled Double-Blind in Vivo Study. *Molecules* **2021**, *26*, doi:10.3390/molecules26061649.

82. Choe, C.; Choe, S.; Schleusener, J.; Lademann, J.; Darvin, M.E. Modified Normalization Method in in Vivo Stratum Corneum Analysis Using Confocal Raman Microscopy to Compensate Nonhomogeneous Distribution of Keratin. *J. Raman Spectrosc.* **2019**, *50*, 945–957.

83. Sütterlin, T.; Tsingos, E.; Bensaci, J.; Stamatas, G.N.; Grabe, N. A 3D Self-Organizing Multicellular Epidermis Model of Barrier Formation and Hydration with Realistic Cell Morphology Based on EPISIM. *Sci. Rep.* **2017**, *7*, 1–11, doi:10.1038/srep43472.

84. Sahle, F.F.; Gebre-Mariam, T.; Dobner, B.; Wohlrab, J.; Neubert, R.H.H. Skin Diseases Associated with the Depletion of Stratum Corneum Lipids and Stratum Corneum Lipid Substitution Therapy. *Skin Pharmacol. Physiol.* **2015**, *28*, 42–55, doi:10.1159/000360009.

85. Tuchin, V. V. Tissue Optics and Photonics: Biological Tissue Structures. *J. Biomed. Photonics Eng.* **2015**, *1*, 3–21, doi:10.18287/jbpe-2015-1-1-3.

86. Choe, C.; Schleusener, J.; Lademann, J.; Darvin, M.E. Keratin-Water-NMF Interaction as a Three Layer Model in the Human Stratum Corneum Using in Vivo Confocal Raman Microscopy. *Sci. Rep.* **2017**, *7*, doi:10.1038/s41598-017-16202-x.

87. Tuchina, D.K.; Shi, R.; Bashkatov, A.N.; Genina, E.A.; Zhu, D.; Luo, Q.; Tuchin, V. V. Ex Vivo Optical Measurements of Glucose Diffusion Kinetics in Native and Diabetic Mouse Skin. *J. Biophotonics* **2015**, *8*, 332–346, doi:10.1002/jbio.201400138.

88. Bashkatov, A.N.; Genina, E.A.; Tuchin, V. V. Optical Properties of Skin, Subcutaneous, and Muscle Tissues: A Review. *J. Innov. Opt. Health Sci.* **2011**, *4*, 9–38, doi:10.1142/S1793545811001319.

89. Zhang, Q.; Andrew Chan, K.L.; Zhang, G.; Gillece, T.; Senak, L.; Moore, D.J.; Mendelsohn, R.; Flach, C.R. Raman Microspectroscopic and Dynamic Vapor Sorption Characterization of Hydration in Collagen and Dermal Tissue. *Biopolymers* **2011**, *95*, 607–615, doi:10.1002/bip.21618.

90. Bashkatov, A.N.; Genina, É.A.; Kochubey, V.I.; Tuchin, V. V. Optical Properties of the Subcutaneous Adipose Tissue in the Spectral Range 400-2500 Nm. *Opt. Spectrosc. (English Transl. Opt. i Spektrosk.* **2005**, *99*, 836–842, doi:10.1134/1.2135863.

91. Bashkatov, A.N.; Genina, E.A.; Kochubey, V.I.; Tuchin, V. V. Optical Properties of Human Skin, Subcutaneous and Mucous Tissues in the Wavelength Range from 400 to 2000 Nm. *J. Phys. D. Appl. Phys.* **2005**, *38*, 2543–2555, doi:10.1088/0022-3727/38/15/004.

92. McGrath, J.A.; Eady, R.A.J.; Pope, F.M. Anatomy and Organization of Human Skin. *Rook's Textb. Dermatology* **2008**, 45–128, doi:10.1002/9780470750520.CH3.

93. Genina, E.; Bashkatov, A.; Tuchin, V. Optical Clearing of Human Dura Mater by Glucose Solutions. *J. Biomed. Photonics Eng.* **2017**, *3*, 010309, doi:10.18287/jbpe17.03.010309.

94. C. V. Raman; K.s.Krishnan A New Type of Secondary Radiation. *NASSP Bull.* **1928**, *22*, 501–501.

95. Dieing, T., Hollricher, O., & Toporski, J. *Confocal Raman Microscopy Second Edition*; **2018**; Vol. 66; ISBN 9783319753782.

96. Ewen Smith, G.D. *Modern Raman Spectroscopy – a Practical Approach*; SECOND.; John Wiley & Sons Ltd, **2019**; ISBN 9781119130536.

97. Auner, G.W.; Koya, S.K.; Huang, C.; Broadbent, B.; Trexler, M.; Auner, Z.; Elias, A.; Mehne, K.C.; Brusatori, M.A. Applications of Raman Spectroscopy in Cancer Diagnosis. *Cancer Metastasis Rev.* **2018**, *37*, 691–717, doi:10.1007/s10555-018-9770-9.

98. Kollias, N.; Stamatas, G.N. Optical Non-Invasive Approaches to Diagnosis of Skin Diseases. *J. Investig. Dermatology Symp. Proc.* **2002**, *7*, 64–75, doi:10.1046/j.1523-1747.2002.19635.x.

99. Caspers, P.J.; Lucassen, G.W.; Carter, E.A.; Bruining, H.A.; Puppels, G.J. In Vivo Confocal Raman Microspectroscopy of the Skin: Noninvasive Determination of Molecular Concentration Profiles. *J. Invest. Dermatol.* **2001**, *116*, 434–442, doi:10.1046/j.1523-1747.2001.01258.x.

100. Abramczyk, H. Introduction to Laser Spectroscopy. *Elsevier* **2005**, 332.

101. Mizuno, A.; Hayashi, T.; Tashibu, K.; Maraishi, S.; Kawauchi, K.; Ozaki, Y. Near-Infrared FT-Raman Spectra of the Rat Brain Tissues. *Neurosci. Lett.* **1992**, *141*, 47–52, doi:10.1016/0304-3940(92)90331-Z.

102. Mizuno, A.; Kitajima, H.; Kawauchi, K.; Muraishi, S.; Ozaki, Y. Near-infrared Fourier Transform Raman Spectroscopic Study of Human Brain Tissues and Tumours. *J. Raman Spectrosc.* **1994**, *25*, 25–29, doi:10.1002/jrs.1250250105.

103. Jermyn, M.; Desroches, J.; Aubertin, K.; St-Arnaud, K.; Madore, W.J.; De Montigny, E.; Guiot, M.C.; Trudel, D.; Wilson, B.C.; Petrecca, K.; et al. A Review of Raman Spectroscopy Advances with an Emphasis on Clinical Translation Challenges in Oncology. *Phys. Med. Biol.* **2016**, *61*, R370–R400, doi:10.1088/0031-9155/61/23/R370.

104. Krafft, C.; Schmitt, M.; Schie, I.W.; Cialla-May, D.; Matthäus, C.; Bocklitz, T.; Popp, J. Label-Free Molecular Imaging of Biological Cells and Tissues by Linear and Nonlinear Raman Spectroscopic Approaches. *Angew. Chemie - Int. Ed.* **2017**, *56*, 4392–4430, doi:10.1002/anie.201607604.

105. Movasaghi, Z.; Rehman, S.; Rehman, I.U. Raman Spectroscopy of Biological Tissues. *Appl. Spectrosc. Rev.* **2007**, *42*, 493–541, doi:10.1080/05704920701551530.

106. Guilbert, M.; Said, G.; Happillon, T.; Untereiner, V.; Garnotel, R.; Jeannesson, P.; Sockalingum, G.D. Probing Non-Enzymatic Glycation of Type i Collagen: A Novel Approach Using Raman and Infrared Biophotonic Methods. *Biochim. Biophys. Acta - Gen. Subj.* **2013**, *1830*, 3525–3531, doi:10.1016/j.bbagen.2013.01.016.

107. Jastrzebska, M.; Wrzalik, R.; Kocot, A.; Zalewska-Rejdak, J.; Cwalina, B. Raman Spectroscopic Study of Glutaraldehyde-Stabilized Collagen and Pericardium Tissue. *J. Biomater. Sci. Polym. Ed.* **2003**, *14*, 185–197, doi:10.1163/156856203321142605.

108. Talari, A.C.S.; Movasaghi, Z.; Rehman, S.; Rehman, I.U. Raman Spectroscopy of Biological Tissues. *Appl. Spectrosc. Rev.* **2015**, *50*, 46–111, doi:10.1080/05704928.2014.923902.

109. Lo, W.L.; Lai, J.Y.; Feinberg, S.E.; Izumi, K.; Kao, S.Y.; Chang, C.S.; Lin, A.; Chiang, H.K. Raman Spectroscopy Monitoring of the Cellular Activities of a Tissue-Engineered Ex Vivo Produced Oral Mucosal Equivalent. *J. Raman Spectrosc.* **2011**, *42*, 174–178, doi:10.1002/jrs.2688.

110. Naomi, R.; Ridzuan, P.M.; Bahari, H. Current Insights into Collagen Type I. *Polymers (Basel).* **2021**, *13*, 1–19, doi:10.3390/polym13162642.

111. Jariashvili, K.; Madhan, B.; Brodsky, B.; Kuchava, A.; Namicheishvili, L.; Metreveli, N. Uv Damage of Collagen: Insights from Model Collagen Peptides. *Biopolymers* **2012**, *97*, 189–198, doi:10.1002/bip.21725.

112. Aarnoutse, P.J.; Westerhuis, J.A. Quantitative Raman Reaction Monitoring Using the Solvent

as Internal Standard. *Anal. Chem.* **2005**, *77*, 1228–1236, doi:10.1021/ac0401523.

113. Binder, L.; Kulovits, E.M.; Petz, R.; Ruthofer, J.; Baurecht, D.; Klang, V.; Valenta, C. Penetration Monitoring of Drugs and Additives by ATR-FTIR Spectroscopy/Tape Stripping and Confocal Raman Spectroscopy – A Comparative Study. *Eur. J. Pharm. Biopharm.* **2018**, *130*, 214–223, doi:10.1016/j.ejpb.2018.07.007.

114. Mujica Ascencio, S.; Choe, C.S.; Meinke, M.C.; Müller, R.H.; Maksimov, G. V.; Wigger-Alberti, W.; Lademann, J.; Darvin, M.E. Confocal Raman Microscopy and Multivariate Statistical Analysis for Determination of Different Penetration Abilities of Caffeine and Propylene Glycol Applied Simultaneously in a Mixture on Porcine Skin Ex Vivo. *Eur. J. Pharm. Biopharm.* **2016**, *104*, 51–58, doi:10.1016/j.ejpb.2016.04.018.

115. Tippavajhala, V.K.; de Oliveira Mendes, T.; Martin, A.A. In Vivo Human Skin Penetration Study of Sunscreens by Confocal Raman Spectroscopy. *AAPS PharmSciTech* **2018**, *19*, 753–760, doi:10.1208/s12249-017-0852-8.

116. Choe, C.; Lademann, J.; Darvin, M.E. Analysis of Human and Porcine Skin in Vivo/Ex Vivo for Penetration of Selected Oils by Confocal Raman Microscopy. *Skin Pharmacol. Physiol.* **2015**, *28*, 318–330, doi:10.1159/000439407.

117. Tfaili, S.; Josse, G.; Angiboust, J.F.; Manfait, M.; Piot, O. Monitoring Caffeine and Resveratrol Cutaneous Permeation by Confocal Raman Microspectroscopy. *J. Biophotonics* **2014**, *7*, 676–681, doi:10.1002/jbio.201300011.

118. Tfayli, A.; Piot, O.; Pitre, F.; Manfait, M. Follow-up of Drug Permeation through Excised Human Skin with Confocal Raman Microspectroscopy. *Eur. Biophys. J.* **2007**, *36*, 1049–1058, doi:10.1007/s00249-007-0191-x.

119. Krombholz, R.; Lunter, D. A New Method for In-Situ Skin Penetration AAnalysis by Confocal Raman Microscopy. *Molecules* **2020**, *25*, doi:10.3390/molecules25184222.

120. Krombholz, R.; Fressle, S.; Lunter, D. Ex Vivo—In Vivo Correlation of Retinol Stratum Corneum Penetration Studies by Confocal Raman Microspectroscopy and Tape Stripping. *Int. J. Cosmet. Sci.* **2022**, *44*, 299–308, doi:10.1111/ics.12775.

121. Caspers, P.J.; Nico, C.; Bakker Schut, T.C.; Sterke, J.; Pudney, P.D.A.; Curto, P.R.; Illand, A.; Puppels, G.J. Method to Quantify the in Vivo Skin Penetration of Topically Applied Materials Based on Confocal Raman Spectroscopy . *Transl. Biophotonics* **2019**, *1*, 1–10, doi:10.1002/tbio.201900004.

122. Choe, C.S.; Ri, J.S.; Choe, S.H.; Kim, P.S.; Lademann, J.; Schleusener, J.; Darvin, M.E. TMCR-ALS Method for the Determination of Water Concentration Profiles in the Stratum Corneum of Untreated and Treated Skin in Vivo. *J. Raman Spectrosc.* **2022**, 0–3, doi:10.1002/jrs.6349.

123. Choe, C.S.; Schleusener, J.; Ri, J.S.; Choe, S.H.; Kim, P.S.; Lademann, J.; Darvin, M.E. Quantitative Determination of Concentration Profiles of Skin Components and Topically Applied Oils by Tailored Multivariate Curve Resolution-Alternating Least Squares Using in Vivo Confocal Raman Micro-Spectroscopy. *J. Biophotonics* **2023**, *16*, 1–11, doi:10.1002/jbio.202200219.

124. Choe, C.S.; Pak, G.J.; Ascencio, S.M.; Darvin, M.E. Quantification of Skin Penetration of Caffeine and Propylene Glycol Applied Topically in a Mixture by Tailored Multivariate Curve Resolution-Alternating Least Squares of Depth-Resolved Raman Spectra. *J. Biophotonics* **2023**, 1–13, doi:10.1002/jbio.202300146.

125. Yakimov, B.P.; Venets, A. V.; Schleusener, J.; Fadeev, V. V.; Lademann, J.; Shirshin, E.A.; Darvin, M.E. Blind Source Separation of Molecular Components of the Human Skin: In Vivo: Non-Negative Matrix Factorization of Raman Microspectroscopy Data. *Analyst* **2021**, *146*, 3185–3196, doi:10.1039/d0an02480e.

126. Miloudi, L.; Bonnier, F.; Tfayli, A.; Yvergnaux, F.; Byrne, H.J.; Chourpa, I.; Munnier, E. Confocal Raman Spectroscopic Imaging for in Vitro Monitoring of Active Ingredient Penetration and Distribution in Reconstructed Human Epidermis Model. *J. Biophotonics* **2018**, *11*, 1–12, doi:10.1002/jbio.201700221.

127. Mélot, M.; Pudney, P.D.A.; Williamson, A.M.; Caspers, P.J.; Van Der Pol, A.; Puppels, G.J. Studying the Effectiveness of Penetration Enhancers to Deliver Retinol through the Stratum Cornum by in Vivo Confocal Raman Spectroscopy. *J. Control. Release* **2009**, *138*, 32–39, doi:10.1016/j.jconrel.2009.04.023.

128. Förster, M.; Bolzinger, M.A.; Ach, D.; Montagnac, G.; Briançon, S. Ingredients Tracking of Cosmetic Formulations in the Skin: A Confocal Raman Microscopy Investigation. *Pharm. Res.* **2011**, *28*, 858–872, doi:10.1007/s11095-010-0342-0.

129. Franzen, L.; Anderski, J.; Windbergs, M. Quantitative Detection of Caffeine in Human Skin by Confocal Raman Spectroscopy - A Systematic in Vitro Validation Study. *Eur. J. Pharm. Biopharm.* **2015**, *95*, 110–116, doi:10.1016/j.ejpb.2015.03.026.

130. Alonso, C.; Carrer, V.; Barba, C.; Coderch, L. Caffeine Delivery in Porcine Skin: A Confocal Raman Study. *Arch. Dermatol. Res.* **2018**, *310*, 657–664, doi:10.1007/s00403-018-1854-4.

131. Choe, C.S.; Ri, J.R.; Schleusener, J.; Lademann, J.; Darvin, M.E. The Non-Homogenous Distribution and Aggregation of Carotenoids in the Stratum Corneum Correlates with the Organization of Intercellular Lipids in Vivo. *Exp. Dermatol.* **2019**, *28*, 1237–1243, doi:10.1111/exd.14018.

132. Zhang, D.; Bian, Q.; Zhou, Y.; Huang, Q.; Gao, J. The Application of Label-Free Imaging Technologies in Transdermal Research for Deeper Mechanism Revealing. *Asian J. Pharm. Sci.* **2021**, *16*, 265–279, doi:10.1016/j.ajps.2020.07.004.

133. Watanabe, N.; Suga, K.; Umakoshi, H. Functional Hydration Behavior: Interrelation between Hydration and Molecular Properties at Lipid Membrane Interfaces. *J. Chem.* **2019**, *2019*, doi:10.1155/2019/4867327.

134. Choe, C.; Schleusener, J.; Choe, S.; Lademann, J.; Darvin, M.E. A Modification for the Calculation of Water Depth Profiles in Oil-Treated Skin by in Vivo Confocal Raman Microscopy. *J. Biophotonics* **2020**, *13*, 1–9, doi:10.1002/jbio.201960106.

135. Sdobnov, A.Y.; Darvin, M.E.; Schleusener, J.; Lademann, J.; Tuchin, V. V. Hydrogen Bound Water Profiles in the Skin Influenced by Optical Clearing Molecular Agents—Quantitative Analysis Using Confocal Raman Microscopy. *J. Biophotonics* **2019**, *12*, 1–11, doi:10.1002/jbio.201800283.

136. Huizinga, A.; Bot, A.C.C.; de Mul, F.F.M.; Vrensen, G.F.J.M.; Greve, J. Local Variation in Absolute Water Content of Human and Rabbit Eye Lenses Measured by Raman Microspectroscopy. *Exp. Eye Res.* **1989**, *48*, 487–496, doi:10.1016/0014-4835(89)90032-8.

137. Nakagawa, N.; Matsumoto, M.; Sakai, S. In Vivo Measurement of the Water Content in the Dermis by Confocal Raman Spectroscopy. *Ski. Res. Technol.* **2010**, *16*, 137–141, doi:10.1111/j.1600-0846.2009.00410.x.

138. Vyumvuhore, R.; Tfayli, A.; Duplan, H.; Delalleau, A.; Manfait, M.; Baiilet-Guffroy, A. Effects of Atmospheric Relative Humidity on Stratum Corneum Structure at the Molecular Level: Ex Vivo Raman Spectroscopy Analysis. *Analyst* **2013**, *138*, 4103–4111, doi:10.1039/c3an00716b.

139. Choe, C.; Lademann, J.; Darvin, M.E. Depth Profiles of Hydrogen Bound Water Molecule Types and Their Relation to Lipid and Protein Interaction in the Human Stratum Corneum: In Vivo. *Analyst* **2016**, *141*, 6329–6337.

140. Sun, Q. The Raman OH Stretching Bands of Liquid Water. *Vib. Spectrosc.* **2009**, *51*, 213–217, doi:10.1016/j.vibspec.2009.05.002.

141. Weny, X.; Maoy, Z.; Han, Z.; Tuchin, V. V.; Zhu, D. In Vivo Skin Optical Clearing by Glycerol Solutions: Mechanism. *J. Biophotonics* **2010**, *3*, 44–52, doi:10.1002/jbio.200910080.

142. Zhou, Y.; Yao, J.; Wang, L. V. Tutorial on Photoacoustic Tomography. *J. Biomed. Opt.* **2016**, *21*, 061007, doi:10.1117/1.jbo.21.6.061007.

143. Doi, M.; Tominaga, S. Spectral Estimation of Human Skin Color Using The Kubelka-Munk Theory. *Proc. SPIE - Int. Soc. Opt. Eng. 5008221-228* **2003**.

144. Darvin, M.E.; Lademann, J.; von Hagen, J.; Lohan, S.B.; Kolmar, H.; Meinke, M.C.; Jung, S. Carotenoids in Human Skin In Vivo: Antioxidant and Photo-Protectant Role against External and Internal Stressors. *Antioxidants* **2022**, *11*, 1–31, doi:10.3390/antiox11081451.

145. Dawson, J.B.; Barker, D.J.; Ellis, D.J.; Cotterill, J.A.; Grassam, E.; Fisher, G.W.; Feather, J.W. A Theoretical and Experimental Study of Light Absorption and Scattering by in Vivo Skin. *Phys. Med. Biol.* **1980**, *25*, 695–709, doi:10.1088/0031-9155/25/4/008.

146. Bigio, I.J.; Fantini, S. Quantitative Biomedical Optics: Theory, Methods, and Applications. *Cambridge Univ. Press* **2016**, 698.

147. Mourant, J.R.; Freyer, J.P.; Hielscher, A.H.; Eick, A.A.; Shen, D.; Johnson, T.M. Mechanisms of Light Scattering from Biological Cells Relevant to Noninvasive Optical-Tissue Diagnostics. *Appl. Opt.* **1998**, *37*, 3586, doi:10.1364/ao.37.003586.

148. Bashkatov, A.N.; Genina, E.A.; Kochubey, V.I.; Stolnitz, M.M.; Bashkatova, T.A.; Novikova, O. V.; Peshkova, A.Y.; Tuchin, V. V. Optical Properties of Melanin in the Skin and Skinlike Phantoms. *Control. Tissue Opt. Prop. Appl. Clin. Study* **2000**, *4162*, 219–226, doi:10.1117/12.405946.

149. Salomatina, E.; Jiang, B.; Novak, J.; Yaroslavsky, A.N. Optical Properties of Normal and Cancerous Human Skin in the Visible and Near-Infrared Spectral Range. *J. Biomed. Opt.* **2006**, *11*, 064026, doi:10.1117/1.2398928.

150. Vo-Dinh, T. *Biomedical Photonics Handbook*; second.; **2015**; ISBN 9781420085136.

151. Leonard, D.W.; Meek, K.M. Refractive Indices of the Collagen Fibrils and Extrafibrillar Material of the Corneal Stroma. *Biophys. J.* **1997**, *72*, 1382–1387, doi:10.1016/S0006-3495(97)78784-8.

152. Tsang, S.H.; Sharma, T. *Optical Coherence Tomography*; **2018**; Vol. 1085; ISBN 9783319064185.

153. Lazareva, E.N.; Tuchin, V. V. Measurement of Refractive Index of Hemoglobin in the Visible/NIR Spectral Range. *J. Biomed. Opt.* **2018**, *23*, 1, doi:10.1117/1.jbo.23.3.035004.

154. Friebel, M.; Meinke, M. Model Function to Calculate the Refractive Index of Native Hemoglobin in the Wavelength Range of 250-1100 Nm Dependent on Concentration. *Appl. Opt.* **2006**, *45*, 2838–2842, doi:10.1364/AO.45.002838.

155. Tuchin V. V, Wang L., Z.D.A. *Optical Polarization in Biomedical Applications*; Springer Science & Business Media, 2006; ISBN 9783540258766.

156. Qi, Y.; Yu, T.; Xu, J.; Wan, P.; Ma, Y.; Zhu, J.; Li, Y.; Gong, H.; Luo, Q.; Zhu, D. FDISCO: Advanced Solvent-Based Clearing Method for Imaging Whole Organs. *Arch. di Stud. Urbani e Reg.* **2019**, *48*, 1–13, doi:10.1126/sciadv.aau8355.

157. Mai, H.; Luo, J.; Hoeher, L.; Al-Maskari, R.; Horvath, I.; Chen, Y.; Kofler, F.; Piraud, M.; Paetzold, J.C.; Modamio, J.; et al. Whole-Body Cellular Mapping in Mouse Using Standard IgG Antibodies. *Nat. Biotechnol.* **2023**, doi:10.1038/s41587-023-01846-0.

158. Zhu, J.; Li, D.; Yu, T.; Zhu, D. Optical Angiography for Diabetes-Induced Pathological Changes in Microvascular Structure and Function: An Overview. *J. Innov. Opt. Health Sci.* **2022**, *15*, 1–20, doi:10.1142/S1793545822300026.

159. Zhu, J.; Liu, X.; Xu, J.; Deng, Y.; Wang, P.; Liu, Z.; Yang, Q.; Li, D.; Yu, T.; Zhu, D. A Versatile Vessel Casting Method for Fine Mapping of Vascular Networks Using a Hydrogel-Based Lipophilic Dye Solution. *Cell Reports Methods* **2023**, *3*, 100407, doi:10.1016/j.crmeth.2023.100407.

160. Martinelli, L.P.; Iermak, I.; Moriyama, L.T.; Requena, M.B.; Pires, L.; Kurachi, C. Optical Clearing Agent Increases Effectiveness of Photodynamic Therapy in a Mouse Model of Cutaneous Melanoma: An Analysis by Raman Microspectroscopy. *Biomed. Opt. Express* **2020**, *11*, 6516, doi:10.1364/boe.405039.

161. Cui, Y.; Wang, X.; Ren, W.; Liu, J.; Irudayaraj, J. Optical Clearing Delivers Ultrasensitive Hyperspectral Dark-Field Imaging for Single-Cell Evaluation. *ACS Nano* **2016**, *10*, 3132–3143, doi:10.1021/acsnano.6b00142.

162. Bashkatov, A.N.; Genina, E.A.; Kochubey, V.I.; Tuchin, V. V. Estimation of Wavelength Dependence of Refractive Index of Collagen Fibers of Scleral Tissue. *Control. Tissue Opt. Prop. Appl. Clin. Study* **2000**, *4162*, 265–268, doi:10.1117/12.405952.

163. Oliveira, L.M.C.; Tuchin, V.V. The Optical Clearing Method - A New Tool for Clinical Practice and Biomedical Engineering. *Springer Nat. Switz. AG, Basel* **2019**, 1–177.

164. Tainaka, K.; Kuno, A.; Kubota, S.I.; Murakami, T.; Ueda, H.R. *Chemical Principles in Tissue Clearing and Staining Protocols for Whole-Body Cell Profiling*; 2016; Vol. 32; ISBN 1113151250.

165. Tainaka, K.; Kubota, S.I.; Suyama, T.Q.; Susaki, E.A.; Perrin, D.; Ukai-Tadenuma, M.; Ukai, H.; Ueda, H.R. Whole-Body Imaging with Single-Cell Resolution by Tissue Decolorization. *Cell* **2014**, *159*, 911–924, doi:10.1016/j.cell.2014.10.034.

166. Richardson, D.S.; Lichtman, J.W. Clarifying Tissue Clearing. *Cell* **2015**, *162*, 246–257, doi:10.1016/j.cell.2015.06.067.

167. Tuchin, V. V.; Xu, X.; Wang, R.K. Dynamic Optical Coherence Tomography in Studies of Optical Clearing, Sedimentation, and Aggregation of Immersed Blood. *Appl. Opt.* **2002**, *41*, 258–271, doi:10.1364/ao.41.000258.

168. Tuchin, V. V. A Clear Vision for Laser Diagnostics (Review). *IEEE J. Sel. Top. Quantum Electron.* **2007**, *13*, 1621–1628, doi:10.1109/JSTQE.2007.911313.

169. Larin, K. V.; Ghosn, M.G.; Bashkatov, A.N.; Genina, E.A.; Trunina, N.A.; Tuchin, V. V. Optical Clearing for OCT Image Enhancement and In-Depth Monitoring of Molecular Diffusion. *IEEE J. Sel. Top. Quantum Electron.* **2012**, *18*, 1244–1259, doi:10.1109/JSTQE.2011.2181991.

170. Genin, V.; Tuchina, D.; Sadeq, A.J.; Genina, E.; Tuchin, V.; Bashkatov, A. Ex Vivo Investigation of Glycerol Diffusion in Skin Tissue. *J. Biomed. Photonics Eng.* **2016**, *2*, 010303-1-010303–010305, doi:10.18287/jbpe16.02.010303.

171. Bui, A.K.; McClure, R.A.; Chang, J.; Stoianovici, C.; Hirshburg, J.; Yeh, A.T.; Choi, B. Revisiting Optical Clearing with Dimethyl Sulfoxide DMSO. *Lasers Surg. Med.* **2009**, *41*, 142–148, doi:10.1002/lsm.20742.

172. Zhu, D.; Larin, K. V.; Luo, Q.; Tuchin, V. V. Recent Progress in Tissue Optical Clearing. *Laser Photonics Rev.* **2013**, *7*, 732–757, doi:10.1002/lpor.201200056.

173. V V Tuchin, I L Maksimova, D A Zimnyakov, I L Kon, A H Mavlyutov, A.A.M. LIGHT PROPAGATION IN TISSUES WITH CONTROLLED OPTICAL PROPERTIES. *J. Biomed. Opt.* **1997**, *2*, 401–417.

174. Yeh, A.T.; Choi, B.; Nelson, J.S.; Tromberg, B.J. Reversible Dissociation of Collagen in Tissues. *J. Invest. Dermatol.* **2003**, *121*, 1332–1335, doi:10.1046/j.1523-1747.2003.12634.x.

175. Hirshburg, J.; Choi, B.; Nelson, J.S.; Yeh, A.T. Collagen Solubility Correlates with Skin

Optical Clearing. *J. Biomed. Opt.* **2006**, *11*, 040501, doi:10.1117/1.2220527.

176. Hirshburg, J.; Choi, B.; Nelson, J.S.; Yeh, A.T. Correlation between Collagen Solubility and Skin Optical Clearing Using Sugars. *Lasers Surg. Med.* **2007**, *39*, 140–144, doi:10.1002/lsm.20417.

177. Hirshburg, J.M.; Ravikumar, K.M.; Hwang, W.; Yeh, A.T. Molecular Basis for Optical Clearing of Collagenous Tissues. *J. Biomed. Opt.* **2010**, *15*, 055002, doi:10.1117/1.3484748.

178. Rylander, C.G.; Stumpp, O.F.; Milner, T.E.; Kemp, N.J.; Mendenhall, J.M.; Diller, K.R.; Welch, A.J. Dehydration Mechanism of Optical Clearing in Tissue. *J. Biomed. Opt.* **2006**, *11*, 041117, doi:10.1117/1.2343208.

179. Yu, T.; Wen, X.; Tuchin, V. V.; Luo, Q.; Zhu, D. Quantitative Analysis of Dehydration in Porcine Skin for Assessing Mechanism of Optical Clearing. *J. Biomed. Opt.* **2011**, *16*, 095002, doi:10.1117/1.3621515.

180. Oliveira, L.; Carvalho, M.I.; Nogueira, E.; Tuchin, V. V. Optical Clearing Mechanisms Characterization in Muscle. *J. Innov. Opt. Health Sci.* **2016**, *9*, 1–19, doi:10.1142/S1793545816500358.

181. Oliveira, L.M.; Carvalho, M.I.; Nogueira, E.M.; Tuchin, V. V. Errata: Diffusion Characteristics of Ethylene Glycol in Skeletal Muscle. *J. Biomed. Opt.* **2015**, *20*, 059801, doi:10.1117/1.jbo.20.5.059801.

182. Irma L. Kon, Valery V.Bakutkin, Nina V. Bogomolova, Svyatoslav V.Tuchin, D.A.Z. Trazograph Influence on Osmotic Pressure and Tissues' Structures of Human Sciera. *Ophthalmic Technol. VII* **1997**, *2971*, 198–206.

183. Genina, E.A.; Bashkatov, A.N.; Korobko, A.A.; Zubkova, E.A.; Tuchin, V. V.; Yaroslavsky, I.; Altshuler, G.B. Optical Clearing of Human Skin: Comparative Study of Permeability and Dehydration of Intact and Photothermally Perforated Skin. *J. Biomed. Opt.* **2008**, *13*, 021102, doi:10.1117/1.2899149.

184. Tuchin, V.V. (Valeriĭ V. *Handbook of Optical Sensing of Glucose in Biological Fluids and Tissues*; CRC Press, **2009**; ISBN 9781584889748.

185. Yu, T.; Zhu, J.; Li, D.; Zhu, D. Physical and Chemical Mechanisms of Tissue Optical Clearing. *iScience* **2021**, *24*, 102178, doi:10.1016/j.isci.2021.102178.

186. Berezin, K. V.; Dvoretski, K.N.; Chernavina, M.L.; Likhter, A.M.; Smirnov, V. V.; Shagautdinova, I.T.; Antonova, E.M.; Stepanovich, E.Y.; Dzhalmuhambetova, E.A.; Tuchin, V. V. Molecular Modeling of Immersion Optical Clearing of Biological Tissues. *J. Mol. Model.* **2018**, *24*, 9–11, doi:10.1007/s00894-018-3584-0.

187. Yeh, A.T.; Hirshburg, J. Molecular Interactions of Exogenous Chemical Agents with Collagen—Implications for Tissue Optical Clearing. *J. Biomed. Opt.* **2006**, *11*, 014003, doi:10.1117/1.2166381.

188. Vargas, G.; Chan, E.K.; Barton, J.K.; Rylander, H.G.; Welch, A.J. Use of an Agent to Reduce Scattering in Skin. *Lasers Surg. Med.* **1999**, *24*, 133–141, doi:10.1002/(SICI)1096-9101(1999)24:2<133::AID-LSM9>3.0.CO;2-X.

189. Bashkatov, A.N.; Korolevich, A.N.; Tuchin, V. V; Sinichkin, Y.P.; Genina, E.A.; Stolnitz, M.M.; Dubina, N.S.; Vecherinski, S.I.; Belsley, M.S. In Vivo Investigation of Human Skin Optical Clearing and Blood Microcirculation under the Action of Glucose Solution. *Asian J. Phys.* **2006**, *15*, 1–14.

190. Vargas, G.; Barton, J.K.; Welch, A.J. Use of Hyperosmotic Chemical Agent to Improve the Laser Treatment of Cutaneous Vascular Lesions. *J. Biomed. Opt.* **2008**, *13*, 021114, doi:10.1117/1.2907327.

191. Sun, R.W.; Tuchin, V. V.; Zharov, V.P.; Galanzha, E.I.; Richter, G.T. Current Status, Pitfalls

and Future Directions in the Diagnosis and Therapy of Lymphatic Malformation. *J. Biophotonics* **2018**, *11*, 1–12, doi:10.1002/jbio.201700124.

192. Mao, Z.; Zhu, D.; Hu, Y.; Wen, X.; Han, Z. Influence of Alcohols on the Optical Clearing Effect of Skin in Vitro. *J. Biomed. Opt.* **2008**, *13*, 021104, doi:10.1117/1.2892684.

193. Zhu, D.; Zhang, J.; Cui, H.; Mao, Z.; Li, P.; Luo, Q. Short-Term and Long-Term Effects of Optical Clearing Agents on Blood Vessels in Chick Chorioallantoic Membrane. *J. Biomed. Opt.* **2008**, *13*, 021106, doi:10.1117/1.2907169.

194. Genina, E.A.; Bashkatov, A.N.; Tuchin, V. V. Optical Clearing of Cranial Bone. *Adv. Opt. Technol.* **2008**, *2008*, doi:10.1155/2008/267867.

195. Zhu, Z.; Wu, G.; Wei, H.; Yang, H.; He, Y.; Xie, S.; Zhao, Q.; Guo, X. Investigation of the Permeability and Optical Clearing Ability of Different Analytes in Human Normal and Cancerous Breast Tissues by Spectral Domain OCT. *J. Biophotonics* **2012**, *5*, 536–543, doi:10.1002/jbio.201100106.

196. Bykov, A.; Hautala, T.; Kinnunen, M.; Popov, A.; Karhula, S.; Saarakkala, S.; Nieminen, M.T.; Tuchin, V.; Meglinski, I. Imaging of Subchondral Bone by Optical Coherence Tomography upon Optical Clearing of Articular Cartilage. *J. Biophotonics* **2016**, *9*, 270–275, doi:10.1002/jbio.201500130.

197. Galanzha, E.I.; Tuchin, V. V.; Solovieva, A. V.; Stepanova, T. V.; Luo, Q.; Cheng, H. Skin Backreflectance and Microvascular System Functioning at the Action of Osmotic Agents. *J. Phys. D. Appl. Phys.* **2003**, *36*, 1739–1746, doi:10.1088/0022-3727/36/14/313.

198. Khan, M.H.; Choi, B.; Chess, S.; Kelly, K.M.; McCullough, J.; Nelson, J.S. Optical Clearing of in Vivo Human Skin: Implications for Light-Based Diagnostic Imaging and Therapeutics. *Lasers Surg. Med.* **2004**, *34*, 83–85, doi:10.1002/lsm.20014.

199. Choi, B.; Tsu, L.; Chen, E.; Ishak, T.S.; Iskandar, S.M.; Chess, S.; Nelson, J.S. Determination of Chemical Agent Optical Clearing Potential Using in Vitro Human Skin. *Lasers Surg. Med.* **2005**, *36*, 72–75, doi:10.1002/lsm.20116.

200. Genina, E.A.; Bashkatov, A.N.; Kochubey, V.I.; Tuchin, V. V. Optical Clearing of Human Dura Mater. *Opt. Spectrosc. (English Transl. Opt. i Spektrosk.* **2005**, *98*, 470–476, doi:10.1134/1.1890530.

201. Proskurin, S.G.; Meglinski, I. V. Optical Coherence Tomography Imaging Depth Enhancement by Superficial Skin Optical Clearing. *Laser Phys. Lett.* **2007**, *4*, 824–826, doi:10.1002/lapl.200710056.

202. Ghosn, M.G.; Tuchin, V. V.; Larin, K. V. Depth-Resolved Monitoring of Glucose Diffusion in Tissues by Using Optical Coherence Tomography. *Opt. Lett.* **2006**, *31*, 2314, doi:10.1364/ol.31.002314.

203. Kinnunen, M.; Myllylä, R.; Vainio, S. Detecting Glucose-Induced Changes in in Vitro and in Vivo Experiments with Optical Coherence Tomography. *J. Biomed. Opt.* **2008**, *13*, 021111, doi:10.1117/1.2904957.

204. Wang, Y.; Ji, W.; Yu, Z.; Li, R.; Wang, X.; Song, W.; Ruan, W.; Zhao, B.; Ozaki, Y. Contribution of Hydrogen Bonding to Charge-Transfer Induced Surface-Enhanced Raman Scattering of an Intermolecular System Comprising p-Aminothiophenol and Benzoic Acid. *Phys. Chem. Chem. Phys.* **2014**, *16*, 3153–3161, doi:10.1039/c3cp54856b.

205. Ghosn, M.G.; Tuchin, V. V.; Larin, K. V. Nondestructive Quantification of Analyte Diffusion in Cornea and Sclera Using Optical Coherence Tomography. *Investig. Ophthalmol. Vis. Sci.* **2007**, *48*, 2726–2733, doi:10.1167/iovs.06-1331.

206. Guo, X.; Wu, G.; Wei, H.; Deng, X.; Yang, H.; Ji, Y.; He, Y.; Guo, Z.; Xie, S.; Zhong, H.; et al. Quantification of Glucose Diffusion in Human Lung Tissues by Using Fourier Domain Optical Coherence Tomography. *Photochem. Photobiol.* **2012**, *88*, 311–316,

doi:10.1111/j.1751-1097.2011.01065.x.

207. Wang, J.; Ma, N.; Shi, R.; Zhang, Y.; Yu, T.; Zhu, D. Sugar-Induced Skin Optical Clearing: From Molecular Dynamics Simulation to Experimental Demonstration. *IEEE J. Sel. Top. Quantum Electron.* **2014**, *20*, doi:10.1109/JSTQE.2013.2289966.

208. M. G. Ghosn, N. Sudheendran, M. Wendt, A. Glasser, V. V. Tuchin, and K.V.L. Monitoring of Glucose Permeability in Monkey Skin in Vivo Using Optical Coherence Tomography. *J .Biophotonics* **2010**, *23*, 25–33, doi:10.1002/jbio.200910075.Monitoring.

209. Silva, H.F.; Martins, I.S.; Bogdanov, A.A.; Tuchin, V. V.; Oliveira, L.M. Characterization of Optical Clearing Mechanisms in Muscle during Treatment with Glycerol and Gadobutrol Solutions. *J. Biophotonics* **2022**, 1–12, doi:10.1002/jbio.202200205.

210. Tuchina, D.K.; Meerovich, I.G.; Sindeeva, O.A.; Zherdeva, V. V.; Savitsky, A.P.; Bogdanov, A.A.; Tuchin, V. V. Magnetic Resonance Contrast Agents in Optical Clearing: Prospects for Multimodal Tissue Imaging. *J. Biophotonics* **2020**, *13*, 1–19, doi:10.1002/jbio.201960249.

211. Sdobnov, A.; Darvin, M.E.; Lademann, J.; Tuchin, V. A Comparative Study of Ex Vivo Skin Optical Clearing Using Two-Photon Microscopy. *J. Biophotonics* **2017**, *10*, 1115–1123, doi:10.1002/jbio.201600066.

212. Liu, Y.; Yang, X.; Zhu, D.; Shi, R.; Luo, Q. Optical Clearing Agents Improve Photoacoustic Imaging in the Optical Diffusive Regime. *Opt. Lett.* **2013**, *38*, 4236, doi:10.1364/ol.38.004236.

213. Jiang, J.; Wang, R.K. Comparing the Synergistic Effects of Oleic Acid and Dimethyl Sulfoxide as Vehicles for Optical Clearing of Skin Tissue in Vitro. *Phys. Med. Biol.* **2004**, *49*, 5283–5294, doi:10.1088/0031-9155/49/23/006.

214. Guo, L.; Shi, R.; Zhang, C.; Zhu, D.; Ding, Z.; Li, P. Optical Coherence Tomography Angiography Offers Comprehensive Evaluation of Skin Optical Clearing in Vivo by Quantifying Optical Properties and Blood Flow Imaging Simultaneously . *J. Biomed. Opt.* **2016**, *21*, 081202, doi:10.1117/1.jbo.21.8.081202.

215. Jin, X.; Deng, Z.; Wang, J.; Ye, Q.; Mei, J.; Zhou, W.; Zhang, C.; Tian, J. Study of the Inhibition Effect of Thiazone on Muscle Optical Clearing. *J. Biomed. Opt.* **2016**, *21*, 105004, doi:10.1117/1.jbo.21.10.105004.

216. Zhong, H.; Guo, Z.; Wei, H.; Guo, L.; Wang, C.; He, Y.; Xiong, H.; Liu, S. Synergistic Effect of Ultrasound and Thiazone-PEG 400 on Human Skin Optical Clearing in Vivo. *Photochem. Photobiol.* **2010**, *86*, 732–737, doi:10.1111/j.1751-1097.2010.00710.x.

217. Wang, J.; Shi, R.; Zhu, D. Switchable Skin Window Induced by Optical Clearing Method for Dermal Blood Flow Imaging. *J. Biomed. Opt.* **2012**, *18*, 061209, doi:10.1117/1.jbo.18.6.061209.

218. Ding, Y.; Wang, J.; Fan, Z.; Wei, D.; Shi, R.; Luo, Q.; Zhu, D.; Wei, X. Signal and Depth Enhancement for in Vivo Flow Cytometer Measurement of Ear Skin by Optical Clearing Agents. *Biomed. Opt. Express* **2013**, *4*, 2518, doi:10.1364/boe.4.002518.

219. Deng, Z.; Jing, L.; Wu, N.; lv, P.; Jiang, X.; Ren, Q.; Li, C. Viscous Optical Clearing Agent for in Vivo Optical Imaging . *J. Biomed. Opt.* **2014**, *19*, 076019, doi:10.1117/1.jbo.19.7.076019.

220. Vargas, G.; Readinger, A.; Dozier, S.S.; Welch, A.J. Morphological Changes in Blood Vessels Produced by Hyperosmotic Agents and Measured by Optical Coherence Tomography¶. *Photochem. Photobiol.* **2003**, *77*, 541, doi:10.1562/0031-8655(2003)077<0541:mcibvp>2.0.co;2.

221. Shi, R.; Chen, M.; Tuchin, V. V.; Zhu, D. Accessing to Arteriovenous Blood Flow Dynamics Response Using Combined Laser Speckle Contrast Imaging and Skin Optical Clearing. *Biomed. Opt. Express* **2015**, *6*, 1977, doi:10.1364/boe.6.001977.

222. Plotnikov, S.; Juneja, V.; Isaacson, A.B.; Mohler, W.A.; Campagnola, P.J. Optical Clearing for Improved Contrast in Second Harmonic Generation Imaging of Skeletal Muscle. *Biophys. J.* **2006**, *90*, 328–339, doi:10.1529/biophysj.105.066944.

223. Cicchi, R.; Pavone, F.S.; Massi, D.; Sampson, D.D. Contrast and Depth Enhancement in Two-Photon Microscopy of Human Skin Ex Vivo by Use of Optical Clearing Agents. *Opt. Express* **2005**, *13*, 2337, doi:10.1364/opex.13.002337.

224. Notman, R.; Den Otter, W.K.; Noro, M.G.; Briels, W.J.; Anwar, J. The Permeability Enhancing Mechanism of DMSO in Ceramide Bilayers Simulated by Molecular Dynamics. *Biophys. J.* **2007**, *93*, 2056–2068, doi:10.1529/biophysj.107.104703.

225. Caspers, P.J.; Williams, A.C.; Carter, E.A.; Edwards, H.G.M.; Barry, B.W.; Bruining, H.A.; Puppels, G.J. Monitoring the Penetration Enhancer Dimethyl Sulfoxide in Human Stratum Corneum in Vivo by Confocal Raman Spectroscopy. *Pharm. Res.* **2002**, *19*, 1577–1580, doi:10.1023/A:1020481305420.

226. Chen, Y.; Liu, S.; Liu, H.; Tong, S.; Tang, H.; Zhang, C.; Yan, S.; Li, H.; Yang, G.; Zhu, D.; et al. Coherent Raman Scattering Unravelling Mechanisms Underlying Skull Optical Clearing for Through-Skull Brain Imaging. *Anal. Chem.* **2019**, *91*, 9371–9375, doi:10.1021/acs.analchem.9b02624.

227. Wei, M.; Shi, L.; Shen, Y.; Zhao, Z.; Guzman, A.; Kaufman, L.J.; Wei, L.; Min, W. Volumetric Chemical Imaging by Clearing-Enhanced Stimulated Raman Scattering Microscopy. *Proc. Natl. Acad. Sci. U. S. A.* **2019**, *116*, 6608–6617, doi:10.1073/pnas.1813044116.

228. Huang, D.; Zhang, W.; Zhong, H.; Xiong, H.; Guo, X.; Guo, Z. Optical Clearing of Porcine Skin Tissue in Vitro Studied by Raman Microspectroscopy. *J. Biomed. Opt.* **2012**, *17*, 015004, doi:10.1117/1.jbo.17.1.015004.

229. Yanina, I.Y.; Schleusener, J.; Lademann, J.; Tuchin, V. V.; Darvin, M.E. The Effectiveness of Glycerol Solutions for Optical Clearing of the Intact Skin as Measured by Confocal Raman Microspectroscopy. *Opt. Spectrosc.* **2020**, *128*, 759–765, doi:10.1134/S0030400X20060259.

230. McNichols, R.J.; Coté, G.L. Optical Glucose Sensing in Biological Fluids: An Overview. *J. Biomed. Opt.* **2000**, *5*, 5, doi:10.1117/1.429962.

231. Lin, Q.; Lazareva, E.N.; Kochubey, V.I.; Duan, Y.; Tuchin, V. V. Kinetics of Optical Clearing of Human Skin Studied in Vivo Using Portable Raman Spectroscopy. *Laser Phys. Lett.* **2020**, *17*, doi:10.1088/1612-202X/abae6d.

232. Hokr, B.H.; Yakovlev, V. V. Raman Signal Enhancement via Elastic Light Scattering. *Opt. Express* **2013**, *21*, 11757, doi:10.1364/oe.21.011757.

233. Matousek, P. Raman Signal Enhancement in Deep Spectroscopy of Turbid Media. *Appl. Spectrosc.* **2007**, *61*, 845–854, doi:10.1366/000370207781540178.

234. Oelkrug, D.; Boldrini, B.; Rebner, K. Comparative Raman Study of Transparent and Turbid Materials: Models and Experiments in the Remote Sensing Mode. *Anal. Bioanal. Chem.* **2017**, *409*, 673–681, doi:10.1007/s00216-016-9582-0.

235. Liopo, A.; Su, R.; Tsyboulski, D.A.; Oraevsky, A.A. Optical Clearing of Skin Enhanced with Hyaluronic Acid for Increased Contrast of Optoacoustic Imaging. *J. Biomed. Opt.* **2016**, *21*, 081208, doi:10.1117/1.jbo.21.8.081208.

236. Zhang, Y.; Li, D.; Zhou, X.; Gao, X.; Zhao, S.; Li, C. Enhancing Sensitivity of SERRS Nanoprobes by Modifying Heptamethine Cyanine-Based Reporter Molecules. *J. Innov. Opt. Health Sci.* **2016**, *9*, 1–9, doi:10.1142/S1793545816420050.

237. Zhu, Y.; Choe, C.-S.; Ahlberg, S.; Meinke, M.C.; Alexiev, U.; Lademann, J.; Darvin, M.E. Penetration of Silver Nanoparticles into Porcine Skin Ex Vivo Using Fluorescence Lifetime Imaging Microscopy, Raman Microscopy, and Surface-Enhanced Raman Scattering

Microscopy . *J. Biomed. Opt.* **2014**, *20*, 051006, doi:10.1117/1.jbo.20.5.051006.

238. Ozaki Y., Kneipp K., A.R. *Frontiers of Surface-Enhanced Raman Scattering Single Nanoparticles and Single Cells*; John Wiley & Sons, **2014**; ISBN 9781118359020.

239. Yamamoto, Y.S.; Ishikawa, M.; Ozaki, Y.; Itoh, T. Fundamental Studies on Enhancement and Blinking Mechanism of Surface-Enhanced Raman Scattering (SERS) and Basic Applications of SERS Biological Sensing. *Front. Phys.* **2014**, *9*, 31–46, doi:10.1007/s11467-013-0347-3.

240. Zhang, Y.; Liu, H.; Tang, J.; Li, Z.; Zhou, X.; Zhang, R.; Chen, L.; Mao, Y.; Li, C. Noninvasively Imaging Subcutaneous Tumor Xenograft by a Handheld Raman Detector, with the Assistance of an Optical Clearing Agent. *ACS Appl. Mater. Interfaces* **2017**, *9*, 17769–17776, doi:10.1021/acsami.7b04205.

241. Khlebtsov, B.; Burov, A.; Pylaev, T.; Savkina, A.; Prikhozhdenko, E.; Bratashov, D.; Khlebtsov, N. Improving SERS Bioimaging of Subcutaneous Phantom in Vivo with Optical Clearing. *J. Biophotonics* **2022**, *15*, 1–9, doi:10.1002/jbio.202100281.

242. Lai, J.H.; Liao, E.Y.; Liao, Y.H.; Sun, C.K. Investigating the Optical Clearing Effects of 50% Glycerol in Ex Vivo Human Skin by Harmonic Generation Microscopy. *Sci. Rep.* **2021**, *11*, 1–14, doi:10.1038/s41598-020-77889-z.

243. Berger, C.; Sakowitz, O.W.; Kiening, K.L.; Schwab, S. Neurochemical Monitoring of Glycerol Therapy in Patients with Ischemic Brain Edema. *Stroke.* **2005**, *36*, 4–6, doi:10.1161/01.str.0000151328.70519.e9.

244. Chang, C.Y.; Pan, P.H.; Li, J.R.; Ou, Y.C.; Liao, S.L.; Chen, W.Y.; Kuan, Y.H.; Chen, C.J. Glycerol Improves Intracerebral Hemorrhagic Brain Injury and Associated Kidney Dysfunction in Rats. *Antioxidants* **2021**, *10*, 1–13, doi:10.3390/antiox10040623.

245. Sakamaki, M.; Igarashi, H.; Nishiyama, Y.; Hagiwara, H.; Ando, J.; Chishiki, T.; Curran, B.C.; Katayama, Y. Effect of Glycerol on Ischemic Cerebral Edema Assessed by Magnetic Resonance Imaging. *J. Neurol. Sci.* **2003**, *209*, 69–74, doi:10.1016/S0022-510X(02)00465-3.

246. Son, T.; Jung, B. Cross-Evaluation of Optimal Glycerol Concentration to Enhance Optical Tissue Clearing Efficacy. *Ski. Res. Technol.* **2015**, *21*, 327–332, doi:10.1111/srt.12196.

247. Emilia Mazgajczyk , Krzysztof Ścigała , Marcin Czyż , Włodzimierz Jarmundowicz, R.B. Mechanical Properties of Cervical Dura Mater. *Acta Bioeng. Biomech.* **2012**, *14*, 51–58.

248. Michael Frink, Hagen Andruszkow, Christian Zeckey, Christian Krettek, F.H. Experimental Trauma Models: An Update. *J. Biomed. Biotechnol.* **2011**, doi:10.1155/2011/797383.

249. Debeer, S.; Le Luduec, J.B.; Kaiserlian, D.; Laurent, P.; Nicolas, J.F.; Dubois, B.; Kanitakis, J. Comparative Histology and Immunohistochemistry of Porcine versus Human Skin. *Eur. J. Dermatology* **2013**, *23*, 456–466, doi:10.1684/ejd.2013.2060.

250. Mangelsdorf, S.; Vergou, T.; Sterry, W.; Lademann, J.; Patzelt, A. Comparative Study of Hair Follicle Morphology in Eight Mammalian Species and Humans. *Ski. Res. Technol.* **2014**, *20*, 147–154, doi:10.1111/srt.12098.

251. Darvin, M.E.; Richter, H.; Zhu, Y.J.; Meinke, M.C.; Knorr, F.; Gonchukov, S.A.; Koenig, K.; Lademann, J. Comparison of in Vivo and Ex Vivo Laser Scanning Microscopy and Multiphoton Tomography Application for Human and Porcine Skin Imaging. *Quantum Electron.* **2014**, *44*, 646–651, doi:10.1070/qe2014v044n07abeh015488.

252. Sullivan, T.; Eaglstein, W.H.; Davis, S.C.; Mertz, P. The Pig as a Model for Human Wound Healing. *Wound Repair Regen.* **2001**, *9*, 66–76.

253. Tuchin, V. V.; Altshuler, G.B.; Gavrilova, A.A.; Pravdin, A.B.; Tabatadze, D.; Childs, J.; Yaroslavsky, I. V. Optical Clearing of Skin Using Flashlamp-Induced Enhancement of Epidermal Permeability. *Lasers Surg. Med.* **2006**, *38*, 824–836, doi:10.1002/lsm.20392.

254. Akhalaya, M.Y.; Maksimov, G. V.; Rubin, A.B.; Lademann, J.; Darvin, M.E. Molecular

Action Mechanisms of Solar Infrared Radiation and Heat on Human Skin. *Ageing Res. Rev.* **2014**, *16*, 1–11, doi:10.1016/j.arr.2014.03.006.

255. Dai, T.; Pikkula, B.M.; Wang, L. V.; Anvari, B. Comparison of Human Skin Opto-Thermal Response to near-Infrared and Visible Laser Irradiations: A Theoretical Investigation. *Phys. Med. Biol.* **2004**, *49*, 4861–4877, doi:10.1088/0031-9155/49/21/002.

256. Na, R.; Stender, I.M.; Henriksen, M.; Wulf, H.C. Autofluorescence of Human Skin Is Age-Related after Correction for Skin Pigmentation and Redness. *J. Invest. Dermatol.* **2001**, *116*, 536–540, doi:10.1046/j.1523-1747.2001.01285.x.

257. Guillard, E.; Tfayli, A.; Manfait, M.; Baillet-Guffroy, A. Thermal Dependence of Raman Descriptors of Ceramides. Part II: Effect of Chains Lengths and Head Group Structures. *Anal. Bioanal. Chem.* **2011**, *399*, 1201–1213, doi:10.1007/s00216-010-4389-x.

258. Spectragryph - Optical Spectroscopy Software: Description Available online: https://www.effemm2.de/spectragryph/about_descr.html (accessed on 17 October **2020**).

259. Choe, C.; Lademann, J.; Darvin, M.E. A Depth-Dependent Profile of the Lipid Conformation and Lateral Packing Order of the Stratum Corneum in Vivo Measured Using Raman Microscopy. *Analyst* **2016**, *141*, 1981–1987, doi:10.1039/c5an02373d.

260. Zhou, F.; Wang, R.K. Theoretical Model on Optical Clearing of Biological Tissue with Semipermeable Chemical Agents. *Complex Dyn. Fluctuations, Chaos, Fractals Biomed. Photonics* **2004**, *5330*, 215, doi:10.1117/12.531499.

261. Menyaev, Y.A.; Nedosekin, D.A.; Sarimollaoglu, M.; Juratli, M.A.; Galanzha, E.I.; Tuchin, V. V.; Zharov, V.P. Optical Clearing in Photoacoustic Flow Cytometry. *Biomed. Opt. Express* **2013**, *4*, 3030, doi:10.1364/boe.4.003030.

262. Utz, S.R.; Tuchin, V.V.; Galkina, E.M. The Dynamics of Some Human Skin Biophysical Parameters in the Process of Optical Clearing after Hyperosmotic Solutions Topical Application. *Vestn. Dermatol. Venerol.* **2015**, 60–68.

263. Towey, J.J.; Soper, A.K.; Dougan, L. Molecular Insight into the Hydrogen Bonding and Micro-Segregation of a Cryoprotectant Molecule. *J. Phys. Chem. B* **2012**, *116*, 13898–13904, doi:10.1021/jp3093034.

264. Hovhannisyan, V.; Hu, P.-S.; Chen, S.-J.; Kim, C.-S.; Dong, C.-Y. Elucidation of the Mechanisms of Optical Clearing in Collagen Tissue with Multiphoton Imaging. *J. Biomed. Opt.* **2013**, *18*, 046004, doi:10.1117/1.jbo.18.4.046004.

265. Tosato, M.G.; Alves, R.S.; Dos Santos, E.A.P.; Raniero, L.; Menezes, P.F.C.; Belletti, K.M.S.; Praes, C.E.O.; Martin, A.A. Raman Spectroscopic Investigation of the Effects of Cosmetic Formulations on the Constituents and Properties of Human Skin. *Photomed. Laser Surg.* **2012**, *30*, 85–91, doi:10.1089/pho.2011.3059.

266. Calheiros, R.; Machado, N.F.L.; Fiuza, S.M.; Gaspar, A.; Garrido, J.; Milhazes, N.; Borges, F.; Marques, M.P.M. Antioxidant Phenolic Esters with Potential Anticancer Activity: A Raman Spectroscopy Study. *J. Raman Spectrosc.* **2008**, *39*, 95–107, doi:10.1002/jrs.1822.

267. Lakshmi, R.J.; Kartha, V.B.; Krishna, C.M.; Solomon, J.G.R.; Ullas, G.; Devi, P.U. Tissue Raman Spectroscopy for the Study of Radiation Damage: Brain Irradiation of Mice. *Radiat. Res.* **2002**, *157*, 175–182, doi:10.1667/0033-7587(2002)157[0175:TRSFTS]2.0.CO;2.

268. LaComb, R.; Nadiarnykh, O.; Carey, S.; Campagnola, P.J. Quantitative Second Harmonic Generation Imaging and Modeling of the Optical Clearing Mechanism in Striated Muscle and Tendon. *J. Biomed. Opt.* **2008**, *13*, 021109, doi:10.1117/1.2907207.

269. Jaafar, A.; Mahmood, M.H.; Holomb, R.; Himics, L.; Váczi, T.; Sdobnov, A.Y.; Tuchin, V. V.; Veres, M. Ex-Vivo Confocal Raman Microspectroscopy of Porcine Skin with 633/785-NM Laser Excitation and Optical Clearing with Glycerol/Water/DMSO Solution. *J. Innov. Opt. Health Sci.* **2021**, *14*, 1–13, doi:10.1142/S1793545821420037.

270. Zhuo, S.; Chen, J.; Wu, G.; Xie, S.; Zheng, L.; Jiang, X.; Zhu, X. Quantitatively Linking Collagen Alteration and Epithelial Tumor Progression by Second Harmonic Generation Microscopy. *Appl. Phys. Lett.* **2010**, *96*, 94–97, doi:10.1063/1.3441337.

271. Takeuchi, M.; Hayakawa, S.; Ichikawa, A.; Hasegawa, A.; Hasegawa, Y.; Fukuda, T. Multilayered Artificial Dura-Mater Models for a Minimally Invasive Brain Surgery Simulator. *Appl. Sci.* **2020**, *10*, 1–14, doi:10.3390/app10249000.

272. Rausch, M.H.; Heller, A.; Fröba, A.P. Binary Diffusion Coefficients of Glycerol-Water Mixtures for Temperatures from 323 to 448 K by Dynamic Light Scattering. *J. Chem. Eng. Data* **2017**, *62*, 4364–4370, doi:10.1021/acs.jced.7b00717.

273. Akinkunmi, F.O.; Jahn, D.A.; Giovambattista, N. Effects of Temperature on the Thermodynamic and Dynamical Properties of Glycerol-Water Mixtures: A Computer Simulation Study of Three Different Force Fields. *J. Phys. Chem. B* **2015**, *119*, 6250–6261, doi:10.1021/acs.jpcb.5b00439.

274. Egorov, A. V.; Lyubartsev, A.P.; Laaksonen, A. Molecular Dynamics Simulation Study of Glycerol-Water Liquid Mixtures. *J. Phys. Chem. B* **2011**, *115*, 14572–14581, doi:10.1021/jp208758r.

275. D'Errico, G.; Ortona, O.; Capuano, F.; Vitagliano, V. Diffusion Coefficients for the Binary System Glycerol + Water at 25 °C. a Velocity Correlation Study. *J. Chem. Eng. Data* **2004**, *49*, 1665–1670, doi:10.1021/je049917u.

276. Fluhr, J.W.; Darlenski, R.; Surber, C. Glycerol and the Skin: Holistic Approach to Its Origin and Functions. *Br. J. Dermatol.* **2008**, *159*, 23–34, doi:10.1111/j.1365-2133.2008.08643.x.

277. Tuchin, V. V. Coherent Optical Techniques for the Analysis of Tissue Structure and Dynamics. *J. Biomed. Opt.* **1999**, 106–124.

278. Carvalho, S.; Gueiral, N.; Nogueira, E.; Henrique, R.; Oliveira, L.; Tuchin, V. V. Glucose Diffusion in Colorectal Mucosa—a Comparative Study between Normal and Cancer Tissues. *J. Biomed. Opt.* **2017**, *22*, 091506, doi:10.1117/1.jbo.22.9.091506.

279. Mudalige, A.; Pemberton, J.E. Raman Spectroscopy of Glycerol/D2O Solutions. *Vib. Spectrosc.* **2007**, *45*, 27–35, doi:10.1016/j.vibspec.2007.04.002.

280. Schulz, B.; Chan, D.; Bäckström, J.; Rübhausen, M. Spectroscopic Ellipsometry on Biological Materials - Investigation of Hydration Dynamics and Structural Properties. *Thin Solid Films* **2004**, *455–456*, 731–734, doi:10.1016/j.tsf.2004.01.060.

281. Choe, C.; Schleusener, J.; Choe, S.; Ri, J.; Lademann, J.; Darvin, M.E. Stratum Corneum Occlusion Induces Water Transformation towards Lower Bonding State: A Molecular Level in Vivo Study by Confocal Raman Microspectroscopy. *Int. J. Cosmet. Sci.* **2020**, *42*, 482–493, doi:10.1111/ics.12653.

282. Shirshin, E.A.; Gurfinkel, Y.I.; Priezzhev, A. V.; Fadeev, V. V.; Lademann, J.; Darvin, M.E. Two-Photon Autofluorescence Lifetime Imaging of Human Skin Papillary Dermis in Vivo: Assessment of Blood Capillaries and Structural Proteins Localization. *Sci. Rep.* **2017**, *7*, 1171–10, doi:10.1038/s41598-017-01238-w.

283. Frushour, B.G.; Koenig, J.L. Raman Scattering of Collagen, Gelatin, and Elastin. *Biopolymers* **1975**, *14*, 379–391, doi:10.1002/bip.1975.360140211.

284. Gniadecka, M.; Wulf, H.C.; Nielsen, O.F.; Christensen, D.H.; Hercogova, J. Distinctive Molecular Abnormalities in Benign and Malignant Skin Lesions: Studies by Raman Spectroscopy. *Photochem. Photobiol.* **1997**, *66*, 418–423, doi:10.1111/j.1751-1097.1997.tb03167.x.

285. Nijssen, A.; Bakker Schut, T.C.; Heule, F.; Caspers, P.J.; Hayes, D.P.; Neumann, M.H.A.; Puppels, G.J. Discriminating Basal Cell Carcinoma from Its Surrounding Tissue by Raman Spectroscopy. *J. Invest. Dermatol.* **2002**, *119*, 64–69, doi:10.1046/j.1523-1747.2002.01807.x.

286. Huang, Y.; Luo, Y.; Liu, H.; Lu, X.; Zhao, J.; Lei, Y. A Subcutaneously Injected Sers Nanosensor Enabled Long-Term in Vivo Glucose Tracking. *Eng. Sci.* **2021**, *14*, 59–68, doi:10.30919/es8d1161.

287. Ma, K.; Yuen, J.M.; Shah, N.C.; Walsh, J.T.; Glucksberg, M.R.; Duyne, R.P. Van N Vivo, Transcutaneous Glucose Sensing Using Surface-Enhanced Spatially Offset Raman Spectroscopy: Multiple Rats, Improved Hypoglycemic Accuracy, Low Incident Power, and Continuous Monitoring for Greater than 17 Days. *Anal. Chem.* **2011**, *83*, 9146–9152.

288. Wang, H.N.; Register, J.K.; Fales, A.M.; Gandra, N.; Cho, E.H.; Boico, A.; Palmer, G.M.; Klitzman, B.; Vo-Dinh, T. Surface-Enhanced Raman Scattering Nanosensors for in Vivo Detection of Nucleic Acid Targets in a Large Animal Model. *Nano Res.* **2018**, *11*, 4005–4016, doi:10.1007/s12274-018-1982-3.

289. Henry, A.I.; Sharma, B.; Cardinal, M.F.; Kurouski, D.; Van Duyne, R.P. Surface-Enhanced Raman Spectroscopy Biosensing: In Vivo Diagnostics and Multimodal Imaging. *Anal. Chem.* **2016**, *88*, 6638–6647, doi:10.1021/acs.analchem.6b01597.